ABSTRACT

BLAST SHOCK-WAVE CHARACTERIZATION IN EXPERIMENTAL SHOCK TUBES

by
Sudeepto Kahali

Blast-induced traumatic brain injuries have affected U.S. soldiers deployed for extended periods in the gulf and Afghanistan wars. To identify the biomechanical and biochemical mechanisms of injury, critical in the identification of diagnostic and therapeutic tools, compressed gas-driven shock tubes are used by investigators to study shockwave-animal specimen interactions and its biological consequences. However, shock tubes are designed and operated in a variety of geometry with a range of process parameters, and the quality of shock wave characteristics relevant to field conditions and therefore the study of blast-induced traumatic brain injuries suffered by soldiers is affected by those conditions. Lab-to-lab comparison is restricted by these variations, inhibiting data pooling and impeding progress. Shock waves accurately characterized by a validated numerical model can be effective in identifying the relationship between shock characteristics vis-à-vis specific shock tube.

In this work, a finite element model was developed and validated with data from carefully designed experiments. It was hypothesized that the shock wave characteristics are governed by the energy source, geometry of the tube and specimen location, both along the length and within the section. Using three specific aims, it was identified that a truncated finite element model is appropriate. It was also shown, while the shock wave replicated the field parameters inside the shock tube, the characteristics outside the tube was complex and as affected by vortex tube and jet winds. Therefore, it was determined

that this location may not be suitable for replication relevant to the mild TBI problem. It was also determined that shape, size, and location of occlusion increases with the ratio of obstruction to shock tube cross-section.

BLAST SHOCK-WAVE CHARACTERIZATION IN EXPERIMENTAL SHOCK TUBES

by
Sudeepto Kahali

A Dissertation
Submitted to the Faculty of
New Jersey Institute of Technology
in Partial Fulfillment of the Requirements for the Degree of
Doctor of Philosophy in Mechanical Engineering

Department of Mechanical and Industrial Engineering

December 2020

APPROVAL PAGE

BLAST SHOCK-WAVE CHARACTERIZATION IN EXPERIMENTAL SHOCKTUBES

Sudeepto Kahali

Dr. Namas Chandra, Dissertation Advisor Distinguished Professor of Biomedical Engineering, NJIT	Date
Dr. Zhiming Ji, Co-Advisor Professor of Mechanical and Industrial Engineering, NJIT	Date
Dr. Dibakar Dutta, Committee Member Assistant Professor of Mechanical and Industrial Engineering, NJIT	Date
Dr. Eon Soo Lee, Committee Member Associate Professor of Mechanical and Industrial Engineering, NJIT	Date
Dr. Max Roman, Committee Member Director, MS Program, Biomedical Engineering, NJIT	Date

BIOGRAPHICAL SKETCH

Author: Sudeepto Kahali

Degree: Doctor of Philosophy

Date: December 2020

Date of Birth:

Place of Birth:

Undergraduate and Graduate Education:

- Doctor of Philosophy in Mechanical Engineering,
  New Jersey Institute of Technology, Newark, NJ, 2020

- Master of Science in Mechanical Engineering,
  New Jersey Institute of Technology, Newark, NJ, 2015

- Bachelor of Science in Mechanical Engineering,
  Georgia Institute of Technology, Atlanta, GA, 2012

Major: Mechanical Engineering

Presentations and Publications:

Kahali S, Townsend M, Mendez Nguyen M, Kim J, Alay E, Skotak M, et al. (2020) The evolution of secondary flow phenomena and their effect on primary shock conditions in shock tubes: Experimentation and numerical model. PLoS ONE 15(1): e0227125. https://doi.org/10.1371/journal.pone.0227125

Kuriakose M, Skotak M, Misistia A, Kahali S, Sundaramurthy A, Chandra N (2016) Tailoring the Blast Exposure Conditions in the Shock Tube for Generating Pure, Primary Shock Waves: The End Plate Facilitates Elimination of Secondary Loading of the Specimen. PLoS ONE 11(9): e0161597. https://doi.org/10.1371/journal.pone.0161597

< Dedicated to my little brother >

ACKNOWLEDGMENT

I would like to express my gratitude to my advisor, Professor Namas Chandra for the opportunity to work in such a fantastic lab. I am indebted to Dr. Chandra for his supervision and patience during my time in the lab.

I would like to thank Dr. Zhiming Ji, Dr. Dibakar Dutta, Dr. Eon Soo Lee and Dr. Max Roman for being a part of my committee.

I would also like to thank Dr. Molly Townsend for her assistance, guidance, encouragement, and support throughout my graduate studies.

I would also like to thank Dr. Maciej Skotak, Jose Rodriguez, Eren Alay, Jeff Kim and Melissa Mendez-Nguyen from the Center for Injury Biomechanics ($CIBM^3$), for performing all the experiments that were required for second and third specific aims of this work.

I would also like to thank the lab members: Matt Kuriakose, Daniel Younger from $CIBM^3$ for their support and insight during various stages of my work.

Finally, I would like to express my gratitude to my family and friends, without whom it would not have been possible for me to complete my work.

TABLE OF CONTENTS

TABLE OF CONTENTS

(CONTINUED)

TABLE OF CONTENTS

(CONTINUED)

Chapter **Page**

LIST OF FIGURES

LIST OF FIGURES
(CONTINUED)

LIST OF FIGURES
(CONTINUED)

LIST OF FIGURES
(CONTINUED)

LIST OF FIGURES
(CONTINUED)

LIST OF TABLES

CHAPTER 1

INTRODUCTION

1.1 Background

From the days of Trojan war, explosive blasts were always a threat to soldiers and civilians in armed conflicts. Only in the early days of the 20th century, technological advances in the weaponry and massive deployment of artillery in the trench warfare during World War I resulted in the identification of the neurological and psychological effects of blast waves, described as shell shock (Southard, 1919). The mechanisms responsible for shell shock were poorly understood; the term was subsequently banned and replaced with post-concussive syndrome during World War II (Jones, Fear, & Wessely, 2007). It was in the decades after WWII, when systematic research to identify mechanisms responsible for blast injuries was initiated. Blast lung injury was the subject of intense experimental study at the Lovelace Foundation in Albuquerque, New Mexico from the 1950s to 1980 (Stuhmiller, 2008). Additionally, blast-induced traumatic brain injuries (TBI) have been one of the most common injuries in the recent wars in Iraq and Afghanistan. Ironically, better thoracic protective systems against blasts were designed, developed, and deployed that transferred the injuries from lungs to brain, that allowed soldiers to survive but with totally different set of neurological problems. Thus, blast induced brain injuries has been the subject of intense research in the last two decades. Chemical explosives (improvised explosive devices, landmines, grenades) account for the bulk of these brain injuries. Between 2000 and 2017, of the 380,000 head injuries reported, 82.3% were diagnosed as mild TBI ("Defense and Veterans Brain Injury Center, DoD Numbers for Traumatic Brain

Injury," 2013). Mild TBIs are diagnosed using phenomenological clinical criteria as the absence of intracranial abnormalities on computed tomography and magnetic resonance imaging scans making mild TBI hard to detect. These injuries have large repercussions, with developed behavioral abnormalities that include problems in memory and concentration, emotional liability and depression, fatigue, light and noise intolerance, irritability and with correlations with post-traumatic stress disorder (Tanielian, 2008; Tsaousides & Gordon, 2009). Medical symptoms include migraine, insomnia, blurred vision, vertigo, tinnitus, nausea and vomiting (Ruff, 2008). The relationships between injury mechanisms and outcomes for mild TBI remain poorly understood (Hoge et al., 2008), due to the scarcity of information available on the pathophysiology of blast-induced neurotrauma (Tsaousides & Gordon, 2009) in humans. Several prevailing theories have been proposed concerning the mechanism of injury, including blast wave transmission through cranium, thoracic pressure surge, skull deflection and cavitation (Bass et al., 2012; Courtney & Courtney, 2009; Moore et al., 2009; Moss, King, & Blackman, 2009), but presently the causative mechanisms have not been conclusively identified (Fievisohn, Bailey, Guettler, & VandeVord, 2018).

Blast injury research primarily uses two tools to experimentally simulate the mechanics of the injuring events: field testing and shock tubes. Though field testing best matches real world conditions, they are expensive, unsafe, time consuming and have poor repeatability due to lack of control over ambient conditions (Bass et al., 2012). Shock tubes are preferred as they can be operated in controlled environments. The research group led by Clemedson was among the first to use blast tubes to study the effect of shock waves on biological tissues (Clemedson & Criborn, 1955). Shock tubes had previously been used

since the early 19th century in other research fields to study detonation, combustion, ionization, supersonic, and transonic flow fields. (Frohn & De Boer, 1969; Griffith, 1952; Henshall & Aeronautical Research, 1957; Hertzberg, 1951). In the last two decades, shock tubes have become a standard laboratory tool to study the effect of shock waves on animal models, including rodents, pigs, and ferrets (Masel et al., 2012). In a broad survey of recent literature (time span: 2010-2019, Appendix), trends can be observed in 71 experimental studies using shock tubes.

The survey summarized in Figure 1.1 shows that the source of energy in shock tubes is compressed gas, explosive materials, or combustion. Most of the shock tubes (82%) use compressed Helium, Nitrogen, or air, and some use explosives (14%), oxy-acetylene, and other methods, including unloaded firing pins. Shock tube length varied from 1.2 to 21.3 meters, with most shock tubes falling between 4-6.5 m. A majority of the shock tube designs had circular cross-sections. These tubes could produce a blast overpressure in the range 10 kPa to 5.3 MPa and thirteen reported values above 500 kPa. In most of the work surveyed, the purpose of the work was to study injury pathologies in animal models (76%). Other topics of interest included studies involved in understanding and visualizing shock wave physics, shock-structure interactions in materials and shapes, and the investigation of the flow fields near the shock tube exit. In more than half of the tests surveyed, the specimens (animal models, human surrogates, or animal surrogates) were tested near the exit or outside of the shock tubes.

Experimental investigation into the hydrodynamics of shock wave diffraction from an open-ended shock tube utilize a variety of optical techniques to visualize the flow field. Some optical techniques include particle image velocimetry (Arakeri, Das, Krothapalli, &

Lourenco, 2004), holographic interferometry (Onodera, Jiang, & Takayama, 1998), schlieren imaging (Elder Jr & De Haas, 1952), smoke flow visualization (T Murugan, De, Dora, Das, & Kumar, 2013). These techniques capture the density or instantaneous velocities of the flow fields and are primarily used to understand and characterize the nature of exit jets and vortex rings. Increasingly, these optical techniques are coupled with numerical simulations to better describe the observable flow phenomena, enabling additional quantifiable analysis of the flow field (T Murugan, De, Dora, & Das, 2012). However, despite the wealth of work performed in this field, a majority of the work using shock tubes employed sizes either much smaller (Abe & Takayama, 1990; Arakeri et al., 2004; Koroteeva, Znamenskaya, Glazyrin, & Sysoev, 2016; Mariani & Kontis, 2010) or much larger (Condon, Lottero, & Loucks, 1997) than those conventionally used in biomedical applications, which is the focus of this work. Additionally, much of the work is conducted at Mach numbers (typically hypersonic) which would induce a fatal injury in animal models, precluding their usefulness for the study of mild bTBI (Maeno, Kaneta, Morioka, & Honma, 2005; T Murugan, De, Sreevatsa, & Dutta, 2016; Thangadurai Murugan, Dora, De, & Das, 2018; Zare-Behtash, Kontis, & Gongora-Orozco, 2008).

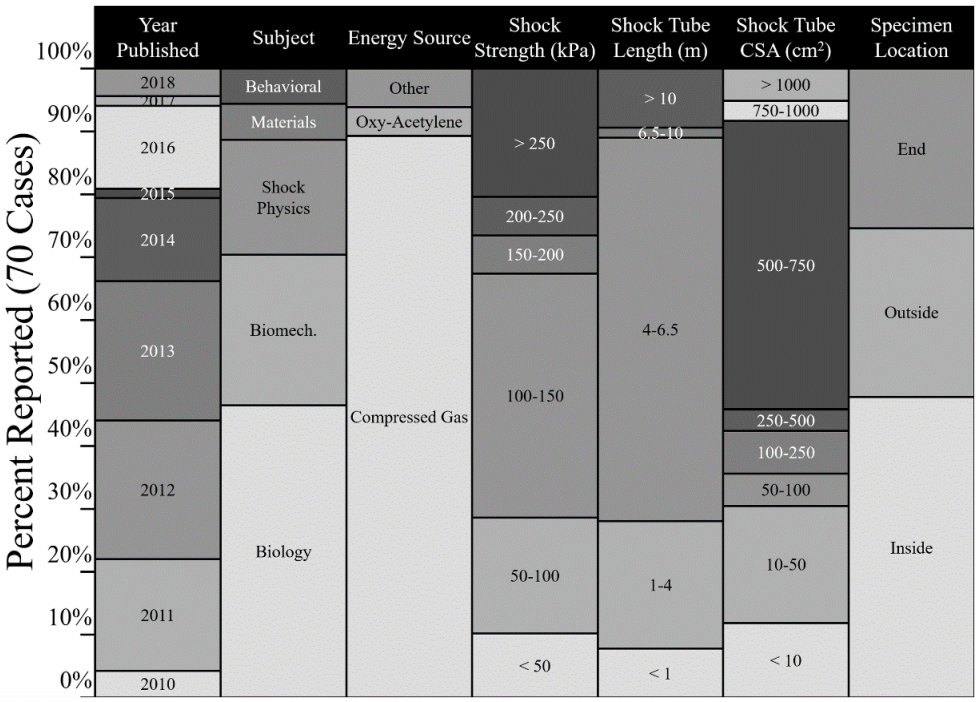

Figure 1.1. Summary of a recent literature survey of experiments using shock tubes. The survey analyzed 71 recent experiments, published between 2010 and 2018, which were conducted using shock tubes. The experimental subject being investigated, the energy source used to generate the shock wave, the shock strength, shock tube length and size, and the location of specimens were identified for each study. Biomech.: Biomechanics; CSA: cross-sectional area.
Note: See Appendix for additional details.

1.2 Motivation for Dissertation Research

As we have seen, blast induced neurotrauma has affected soldiers and innocent civilians exposed to explosive blasts. Such blasts in the recent gulf and Afghanistan wars have caused blast induced traumatic brain injuries (bTBI) to soldiers especially in the form of mild bTBI and has led to many neurocognitive and neuropsychological dysfunctions in the form of PTSD (post-traumatic stress syndrome) years after the conflict. Biomechanical and biochemical mechanisms responsible for the mild bTBI are still largely unknown and has been a major impediment in the development of diagnostic, prognostic, and therapeutic

tools for this serious ailment. Replication of field shock conditions and exposing animal models to the shocks and understanding the loading effects on the animals have been very active areas of research across many academic and federal laboratories. Most of these laboratories use compressed gas-driven shock tubes to simulate the field shock loading conditions as they are simple to construct and have been used since early 19th century for other scientific investigations. This simplicity in construction has led to a range of shock tubes varying in shapes, sizes, lengths, sources of energy, and locations of specimen and all of these geometric and process parameters cause distinctly different shock-loading profiles sometimes quite different from that of the field value they are supposed to replicate. Such variations additionally do not permit lab-to-lab comparisons which are very critical if the data were to be pooled together for scientific advancements. To generate primary field shock waves, the waves need to be planar, free of artifacts from any reflections from the wall structures. Additionally, the specimen size in relation to the shock tube is important to avoid reflections from the shock tube walls and it is imperative that its location be at a position in the shock tube where the ideal field accurate pressure profile is achieved. A wrong profile can cause different loading from that of the field, especially when imposed on an animal model (e.g., rats, mice, and pigs) and cause injuries not relevant to that faced by soldiers. The same applies to the specimen size. To correlate the data from different shock tubes, there is a great need for a numerical model to understand the effect of shock tube configurations, test set-up, specimen size, location, and protocols. The research in the work is motivated by this need. It is an important but challenging task; the uniqueness of the research is in that the numerical model is validated by carefully designed experiments.

1.3 Hypothesis and Specific Aims

Based on the need to characterize the evolution of shock waves in a compressed gas-driven shock tube we hypothesize that, “Shock wave characteristics are governed by energy source, size/shape/length of shock tube, and the location of specimen either inside or outside”. Shock wave characteristics determine the loading on specimens (live or structural) and its relationship to explosive generated field shock waves.

To test this hypothesis, we have identified three different specific aims:

1. Construct and validate a finite element-based shock tube model using experimental data
2. Examine the flow phenomena and their effect at all possible specimen locations to simulate field generate shock wave characteristics, and
3. Investigate the effect of shock artifacts arising from shape and size restrictions of the shock tube and study the effect of specimen geometry occlusions.

In addition to developing the model, the novelty of the work lies in the careful design of experiments that can generate data for comparison with numerical model. Thus, our numerical scheme once validated for a given configuration can then be applied to all other set-ups for comparison purposes. The net outcome will be our ability to pool the data from laboratories and apply the results to actual field shock conditions and subsequent bTBI.

1.4 Organization of Dissertation

In Chapter 1, we outline the general background of explosive blast and bTBI as well as identify the motivation of the work along with hypothesis and specific aims. In Chapter 2, we introduce the theory of explosive shocks and many analytical relationships between the various shock parameters including incident/dynamic/total/reflected pressures,

temperature, and velocities. Here, we introduce in the basic methodology of finite element model that can be used to simulate the complex shock wave characteristics with microsecond rise time and milli second duration with travel lengths in meters. In Chapter 3, we address specific aim 1 to validate the model against well-designed experiments and experimental measurements. Here, we develop two different numerical schemes for correlating with experimental results and identified that one of the methods, the truncated method is more suitable and thus conclude that this method is appropriate to move forward in subsequent aims. In Chapter 4, we address specific aim 2 to examine the flow phenomena on the exit of the shock tube. The method decided upon from Chapter 3 is used here, which consists of using a fully developed shock wave pressure profile from the experiment to generate the shock wave in the shock tube. Within the shock tube, the pressure-time profile remains unchanged and is affected marginally due to friction. However, the profile is affected once the release wave travels back from the open end. The flow phenomena on the outside is very complex and is affected by the magnitude of pressure and orientation of the location from exit. Vortex rings generated at the exit and the magnitude of planarity of the wave also give an idea of the nature of the shock wave at the exit of the shock tube. These results are very useful for investigators who place the specimen outside which is shown to not be ideal for the simulation of bTBI conditions. In the next Chapter 5, we address specific aim 3. The effect of size, shape, thickness, and location within the shock tube is examined and it is seen how these lead to occlusion effects and consequently affect shock wave profile for the specimen. Additionally, the effect of reflection surface is also examined. In the final Chapter 6, we summarize the findings,

outline the scientific contributions, and offer further research ideas emanating from this dissertation research.

CHAPTER 2

THEORY AND LITERATURE REVIEW

2.1 Background

2.1.1 Shock Wave Propagation in Field

In blast TBI research, shock tubes are used to simulate the field condition resulting from an explosion from an explosive. The characteristics of an explosion depends on the chemical content of the charge, extent of the exothermal reaction, energy release rate, the release of gaseous products from the reaction and the rate of propagation of those gaseous products(Baum & Shekhter, 1959). The energy produced due to the exothermal reaction heats the reactive products, leading to rapid expansion which converts the potential energy of the explosive into mechanical work (Baum & Shekhter, 1959; Kinney & Graham, 1985).This propels the components of the explosive spherically in an outward manner, compressing the air around it, leading to the formation of a shock front. A characteristic of the shock front is the rapid rise in air pressure, density, and particle velocity, across an infinitesimally small width. As this shock front (considered ideal and unimpeded) continues to expand, the surface area increases in a nonlinear manner, leading to a rapid reduction of the energy intensity. The shock front, which is compressive in nature, is followed by tensile rarefaction waves propagating in the shock-compressed air. As the shock front propagates through ambient air, it is supersonic with respect to the air in front of the shock and subsonic compared to the air behind it. Thus, the rarefaction waves remain supersonic compared to the compressed air ahead, until the shock wave dies out.

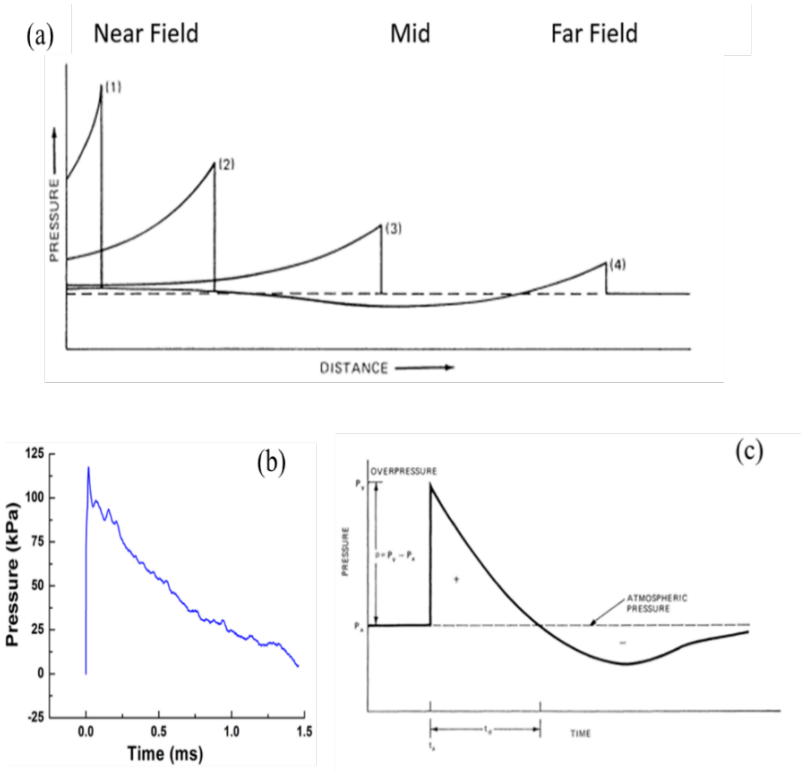

Figure 2.1. (a) Evolution of shock wave as a function of distance where blast overpressure higher than 1000 kPa is near-range, further away are mid- and far- range (b) Profile generated from explosion of 1.814 kg of C4, 2.8m away from explosive center (c) Typical Friedlander waveform at far field.
1a and 1c reprinted from Explosive Shocks in Air, by McKinney and Graham, 1985, retrieved from DOI 10.1007/978-3-642-86682-1; 1b reprinted from Explosive shocks in air, by McKinney and Graham, 1985, https://www.springer.com/us/book/9783642866845

Depending on the distance from the center of the explosion, the blast region can be divided into three regions: near-field, mid-field, and far-field (Figure 2.1 (a) (Ritzel & Matthews, 1997)). Objects in the near-field region are exposed to higher pressures and experience interactions with shrapnel and additional thermal effects. At farther distances from the explosive center, pressure profiles maintain a similar shape, with much lower magnitudes and higher durations. When examining the mechanical environment in the mid- and far-field ranges, effects of temperature and shrapnel can be disregarded. Additionally, in these regions, the shock front has expanded so that it can be considered to be much larger

than that of the human body meaning that the wave front can be approximated as a planar wave (Chandra et al., 2012). Therefore, laboratory settings strive to replicate this planar shock wave, which exhibits lower magnitudes and longer durations, corresponding to those conditions that cause mild TBI.

The unimpeded planar wave front exhibits a characteristic pressure-time profile consisting of a rapid pressure rise, decaying nonlinearly to a period of under pressure (Figure 2.1(c)). It can be mathematically described via the Friedlander equation, given as

$$p(t) = p\left(1 - \frac{t}{t_d}\right) e^{\left(\frac{-t}{\alpha}\right)}. \tag{1.1}$$

where p represents the blast overpressure, t_d represents the positive time duration and α represents the time decay constant (Kinney & Graham, 1985). The blast overpressure is defined as the pressure measured above the initial, atmospheric pressure at a given elevation, ambient temperature, and humidity. The positive phase duration is the amount of time until the pressure profile returns to atmospheric pressure as seen in Figure 2.1 (c). The positive impulse is defined as the area under the pressure-time profile during the positive phase duration. Pressure-time profiles for a C4 explosion, and a typical Friedlander wave can be seen in Figures 2.1 (b) and 2.1 (c), respectively.

It is of interest to consider how this unimpeded shock wave interacts with objects within its environment. When considering only the blast wave impinging on an object, it is customary to define a wave that is devoid of all reflections and other artifacts, wherein a combination of static and dynamic loadings take place. The static component of the wave consists of pure shock information, which is passed between molecules of the medium to the object. The dynamic loading component is the effect of blast winds, or the effect of molecular impact on the object. It imparts drag and lift forces, being mainly responsible

for any displacement of the object. Thus, the object experiences a load which is due to a combination of these effects (Needham, Ritzel, Rule, Wiri, & Young, 2015). The relationship between these components change with respect to the distance from center of the explosion. Close to the center of the explosion, static and dynamic components are approximately the same. As the shock is formed, the dynamic component increases nonlinearly as a function of Mach number of the shock wave velocity. As the shock front decays and the shock wave velocity approaches the acoustic velocity of the medium, the dynamic pressures become negligible. Shock wave loading will also include additional loading artifacts, including reflected pressures resulting from interactions between the shock wave and the ground and/or surrounding objects.

Mathematical relationships exist which describe the nature of the shock front, allowing for numerical approximation of an unimpeded shock front. In the discussion of these relationships, it is convenient to assume the shock front as the point of reference. This would lead to the perception that the unshocked, ambient medium enters the shock plane. Upon passage through this plane, the ambient medium experiences a sudden deceleration, accompanied by an abrupt rise in pressure and temperature. Figure 2.2(a) shows the pressure and temperature before and after shock as P_x, T_x and P_y, T_y respectively. As with any moving stream, three independent relationships are required to establish properties of the stream. In this work, pressure, temperature, and velocity are utilized. For the entering and departing streams across the shock plane, Prandtl's relation states that the product of the stream Mach numbers (M) must equal one (Kinney & Graham, 1985). Thus, one of the streams must be supersonic ($M>1$), while the other must be subsonic ($M<1$). From the

second law of thermodynamics and the tendency toward spontaneous growth of entropy, it is evident that the departing stream is subsonic.

A set of equations referred to as the Rankine-Huguenot conditions can give the relationships between pressure, temperature, and velocity for shocked and unshocked conditions. Air is assumed to behave like an ideal gas and heat capacity is effectively constant with a value of 1.4. Overpressure (p) is the static component of a blast wave, defined as the difference between the unshocked **(**P_x) and shocked (P_y) mediums (Figure 2.2 (b)). P_y also represents the absolute pressure after shock and is called incident pressure. Overpressure can be represented in terms of the Mach number, M_x, as

$$p = P_y - P_x = \frac{7(M_x^2-1)}{6} P_x. \tag{1.2}$$

For an ideal shock, there is no flow of heat to or from the moving stream, making the shock a steady adiabatic flow. The ratio of the shocked and unshocked temperatures (T_y/T_x) can be represented in terms of shock wave velocity as

$$\frac{T_y}{T_x} = \frac{(5+M_x^2)(7M_x^2-1)}{36M_x^2}. \tag{1.3}$$

As previously mentioned, the dynamic pressure component of a blast wave consists of the blast wind. This is due to the movement of particles immediately following the shock. The ratio of particle velocity and acoustic velocity, also known as the Mach number, $M_x = u_p/a_x$, can be represented using shock wave velocity as

$$\frac{u_p}{a_x} = \frac{5(M_x^2-1)}{6M_x}. \tag{1.4}$$

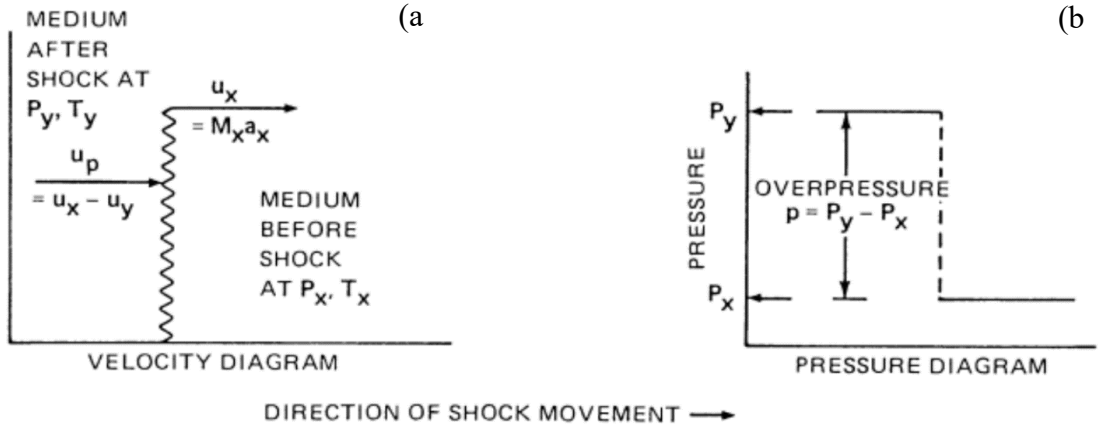

Figure 2.2. Velocity (a) and pressure (b) diagrams depicting an explosive shock moving from left to right with velocity u_x and Mach number M_x: (a) Particle velocity u_p in explosive shock corresponds to a difference in steady-flow velocities, u_x–u_y (b) Overpressure p corresponds to pressure jump, P_y–P_x
Reprinted from Explosive Shocks in Air, by McKinney and Graham, 1985

Dynamic pressure for a stream is a function of its density, ρ and velocity, u_p, and can be calculated as

$$P_{dyn} = \frac{1}{2}\rho {u_p}^2. \tag{1.5}$$

To discuss the measurement of these shock wave parameters in an experimental condition, we can assume that our frame of reference will be the medium, where the shock wave is a moving stream which enters the medium. A fixed instrument is placed in the stream such that it brings the velocity of the medium to zero, converting the kinetic energy to total pressure. This pressure value measured by this instrument represents the effect of gross stream motion, giving the stagnation pressure or total pressure. It is equal to the sum of static and dynamic pressures. Stagnation pressure (P_{stag}) can be calculated from the temperature ratio (T_y/T_x), and the Mach number (u_p/a_x) using equation 1.6.

$$P_{stag} = P_y \left[1 + \frac{(u_p/a_x)^2}{5\left(\frac{T_y}{T_x}\right)}\right]^{3.5}. \tag{1.6}$$

When characterizing the nature of a shock wave, a combination of incident and dynamic pressures is important. The incident pressure represents the shock component, and the dynamic pressure represents the effect of blast winds. Together, they will describe the shock experimental condition.

Theoretical Reflected Overpressure (kPa):

$$P_r = \left(\frac{(4M_x^2-1)(7M_x^2-1)}{3(M_x^2+5)} * 100\right) - P_x. \quad (1.7)$$

Reflected pressure coefficient can be used for easy comparisons between blasts of varying overpressures. It is the ratio of reflected overpressure over incident overpressure. This ratio in our case is dependent on the Mach number of the incident shock. Reflected pressure coefficient can also be calculated from Mach number using Equation 1.7 adapted from (Gilbert Ford Kinney, 1985).

Theoretical reflected pressure coefficient:

$$\frac{P_r}{P_y} = \frac{8M_x^2+4}{M_x^2+5}. \quad (1.8)$$

When a shock wave interacts with a surface it creates a pressure build up on the surface. This creates a relatively flat top region of the reflected pressure profile. The duration of this region is considered the pressure relief start time or dwell time. It is thought that this pressure relief is caused by the arrival of a rarefaction wave from the edges of the plate. This rarefaction wave proves to be difficult to characterize, but its velocity is approximately the same as the speed of sound in the shock medium (Gilbert Ford Kinney, 1985). With this parameter the pressure relief time can be estimated using Equation 1.9, where d is the shortest distance from the point of interest to the edge of the plate. It should

be noted that this is just an estimate and in practice it had been determined to be sufficient for predictions (Gilbert Ford Kinney, 1985).

Pressure relief start time (s)

$$t_r = \frac{d}{u_x}. \tag{1.9}$$

Impulse is the area under the positive phase duration of the pressure profile. It is representative of the energy transmitted by the shock wave.

2.1.2 Shock Wave Propagation in a Shock Tube

Shock tubes are devices build to generate repeatable, and standardized means to create directional blast waves, designed to replicate field blast conditions. The experimental platform has been used in a wide variety of applications, including high speed and temperature aerodynamic research, gas phase combustion, and, more recently, blast wave interaction with biological specimens (Cernak et al., 2011; Nagamatsu, 1958). A shock tube is a simple tube, along which a generated shock wave can propagate. This shock wave can be generated using chemical explosives (Risling et al., 2011) or through a separation of gases with very different pressures (Kuriakose et al., 2016). In the latter method, the conventional methodology uses a diaphragm to divide the tube into two compartments, known as the driver and driven section, enabling a pressure ratio to be formed between them. The pressure differential is created using compressed gas (Kuriakose et al., 2016), or chemical combustion, like a mixture of oxygen and acetylene (Courtney, Andrusiv, & Courtney, 2012). Properly characterized and utilized, there exists a direct correlation between static and dynamic pressure ratios in the shock tube and that observed in free-field explosions (Chandra, Sundaramurthy, & Gupta, 2017).

The focus of this work will be compressed gas-driven shock tubes, which is the predominant method of simulating blast waves in the laboratories. In most cases, the driver section is pressurized, and the driven region is maintained at atmospheric pressure. The driver and driven sections are separated by membranes or a valve. The driver section is filled with gas until the high pressure causes the membranes to burst or the membrane is ruptured via mechanical means. The driver gas, then, rapidly expands into the driven region, which compresses the air in the driven section, leading to the formation of a shock front that travels towards the open end of the tube, termed downstream. Simultaneously, a series of rarefaction waves propagate in the opposite direction, towards the closed end of the shock tube or upstream once the constrained shock waves are allowed free expansion at the exit. Once the membranes rupture, the breech pressure reduces and shock waves travel in either direction, while the flow is along the driven section. Pressure waves also travel upstream towards the closed end and get reflected. A distance-time diagram of shock wave propagation is shown in Figure 2.3(a). The temperature rises during the compression of the driven gas and drops during expansion in the rarefaction wave. This leads to two gaseous bodies which are at same pressure and particle velocity but with different temperature, density and entropy leading to the formation of an interface traveling at the particle velocity. This is called the contact surface and can be seen in Figure 2.3(a). The regions behind the shock and contact surface are both steady, with higher pressures and temperatures (Martin, 1958).

The characteristics of the rarefaction waves are dependent upon the nature of the driver gas and the length of the driver region. For example, helium has a much higher acoustic velocity than air. Therefore, in helium-driven shocks, rarefaction waves will travel

faster than the air shock wave propagating to the end, eventually catching up to the shock wave. The non-sequential arrival of these rarefaction waves leads to the nonlinear decay of the air shock wave resulting in a Friedlander wave (rapid rise time, with nonlinear decay). If the driver gas is changed to nitrogen, which has a similar acoustic velocity to air, the rarefaction waves take longer to catch up to the shock front. This leads to the formation of a flat top wave. The typical profile for nitrogen and helium as driver gases can be seen in Figure 2.3(c) and 2.3(d) respectively.

Figure 2.2(b) and 2.3(c) show that chemical explosions in the field, and compressed gas shock tubes produce pressure profiles that have a sharp rise time followed by a nonlinear decay. After calibration, it is possible to obtain shock tube-generated profiles, that have similar peaks and phase durations. However, it is important to note that the mechanism by which these profiles come about are different. In the formation of the shock front both field and shock tube conditions generate a region of high pressure that can propagate thorough a medium (in this case, air at atmospheric pressure). The reflected shock front from the closed end of the breech generates rarefaction waves as it is propagating through the medium. Since the shock front velocity decreases as it gets farther away from the explosion source, rarefaction waves generated from earlier shock waves catch up to the later, leading to the nonlinear decay. For the shock tube, this decay is due to the catching up of reflected expansion waves from the driver region. Additionally, shock waves dissipate faster in the field than in the shock tube due to the unconstrained movement of the wave.

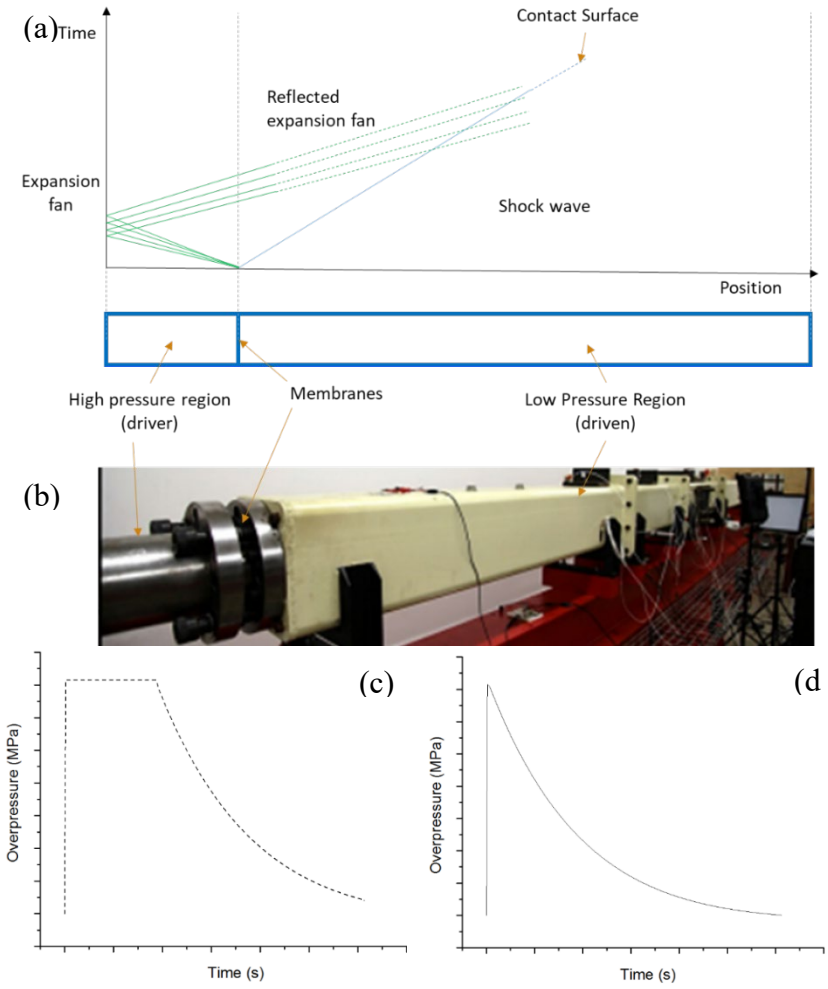

Figure 2.3. (a) Distance-time (x-t) diagram of shock wave in shock tube (b) Picture of shock tube in Center for Injury Biomechanics, Materials and Medicine at the New Jersey Institute of Technology. Pressure-time (p-t) profiles of a (c) nitrogen and (d) helium driver gas.

2.1.3 Finite Element Modelling of Shock Wave

The finite element method (FEM) is used here to model shock wave propagation in a shock tube and shock-structure interaction to replicate the experimental test conditions. FEM allows for the discretization of a boundary value problem spatially and temporally. A domain is spatially discretized into smaller geometrical shapes, called elements, which are connected to each other via nodes.

The governing differential equations are solved for each time step using a weak formulation of the partial differential equations, generated using a weighting function. There are two methods of defining the behavior of a continuum used in this work, Lagrangian and Eulerian methods. In a Lagrangian domain, the material and geometrical numerical mesh are tied together, with the movement of continuum specified as a function of its initial coordinates and time. Thus, nodes of an element follow the distortion of the material. This has limitations for large deformations and/or deformations occurring over very short durations, where the mesh excessively distorts.

In Eulerian domains, movement of a continuum is specified as a function of instantaneous coordinates and time. The Eulerian mesh remains undistorted, while the materials can move freely through the mesh. Thus, not all elements are completely full of material. The Eulerian boundary must be calculated during each time increment and does not correspond with element boundary. It is advantageous for large distortions, or distortions over short periods of time. Thus, a highly dynamic event like a shock is ideal for being modeled in the Eulerian domain. It however has the disadvantage of numerical diffusion in case of two or more materials in the Eulerian domain.

When modeling the interactions between the two domains, as is necessary in this work, the coupled Eulerian-Lagrangian method (CEL) is used. The CEL method attempts to combine the advantages of both Lagrangian and Eulerian methods. The volume of fluid method is used for the Eulerian domain, where the material is tracked as it flows through the mesh by computing Eulerian Volume Fraction (EVF) within each element. The Eulerian elements which are filled with a material are assigned an EVF value of one, while the element containing no material are assigned an EVF value is zero. Since the volume fractions must be calculated for each Eulerian element, the boundaries of each Eulerian material are reconstructed each time increment. The interface reconstruction algorithm approximates the material boundaries within an element as simple planar facets, producing a simple and approximate material surface that can be discontinuous between neighboring elements. Thus, Eulerian domain analyses benefit from higher fidelity meshes (Ahmadzadeh, Saranjam, Hoseini Fard, & Binesh, 2014). For a CEL problem, the governing partial differential equations for conservation of momentum, mass and energy and the equations defining the initial boundary conditions are solved concurrently.

Conservation of mass, momentum and energy are given, respectively, as

$$\rho \frac{\partial v_i}{\partial x_i} + \frac{\partial \rho}{\partial t} + v \cdot \nabla \rho = 0, \tag{2.1}$$

$$\frac{\partial \sigma_{ij}}{\partial x_j} + \rho b_i = \rho a_i, \tag{2.2}$$

$$\rho \frac{\partial e}{\partial t} + v \cdot \nabla e = \sigma_{ij} \frac{\partial v_i}{\partial x_j} - \frac{\partial q_i}{\partial x_i} + \rho q_S. \tag{2.3}$$

In equations 2.1 – 2.3, ρ is density, x, v and a are the respective displacement, velocity and acceleration of a particle, σ is Cauchy stress, b is body force, e is internal

energy per unit mass, q is heat flow per unit area and q_S is rate of heat input per unit mass by external sources.

2.1.4 Objective

There exist inconsistencies in literature regarding the placement and size of subjects in shock tube experiments which seek to recreate a free-field explosive condition. It is hypothesized that there are experimental constraints (i.e. subject location and shock tube occlusion) within the shock tube experimental set up which better simulate a free-field explosion. Identifying the geometric and process parameters using numerical simulations (goal of this research), will result in the right shock wave profile relevant to field conditions. To test this hypothesis, the problem can be approached in three different phases:

1. Construct and validate a finite element-based shock tube model using experimental data,
2. Examine the flow phenomena and their effect at all possible specimen locations to simulate field generate shock wave characteristics, and
3. Investigate the effect of shock artifacts arising from shape and size restrictions of the shock tube and study the effect of specimen geometry occlusions.

Experimental data have been made available by other members of the CIBM3 research group. The author was not directly involved in the experiments but helped to design the experiments, consolidate the data to a format useful for comparison with numerical simulation results. While studies have investigated flow phenomena at the exit and effects of dynamic pressure, the novelty of this work is that it offers the first comprehensive development and investigation of a numerical model of a shock tube fully validated by experimental data. This work will help researchers to effectively use shock tubes to recreate

free-field loading conditions, through a better understanding of the effect that subject placement location and the size of a subject within the shock tube can have on subject loading.

CHAPTER 3

CONSTRUCTION AND VALIDATION OF SHOCK TUBE

The first specific aim of this work is the construction and validation of a finite element model of a shock tube with the purpose of testing the underlying assumptions that the model should be able to replicate the test data and observations. It resulted in the determination of the computational model fidelity that is necessary to best simulate the experimental shock tube setup, building a foundation to answer the questions raised in specific aims 2 and 3. First, a finite element model of a shock tube was created and two methods of shock wave generation were investigated. The experimental setup that was modeled is described in Section 3.1. In each finite element model, experimental pressure-time measurements were compared to the simulated values at different locations along the length of the tube. The most accurate shock wave generation method was selected for subsequent investigation. Additionally, the ideal room size was determined to allow for dissipation of the shock wave from the shock tube exit without any additional artifacts.

3.1 Experimental Setup

The Shock Wave Testing facility at the Center for Injury Biomechanics, Materials and Medicine (CIBM^3) at the New Jersey Institute of Technology houses a shock tube with a 229 mm square cross-section. The shock tube consists of an adjustable-volume driver section called the breech, separated from a 6 m driven section by a 1.5 m transition section. Mylar membranes separate the breech (driver) from the driven region. The transition section allows for a change in the profile of the shock tube from circular (breech section) cross section with a 102 mm diameter to the square (driven region) cross section. Incident

pressure measurements are made using Model 134A24 from PCB Piezotronics sensors that are flush with the walls of the shock tube. Locations of available sensor data is shown in Figure 3.1, highlighted in yellow. The severity or strength of the shock wave is quantified as the blast overpressure at the primary test location, denoted as T4 in Figure 3.1. The overpressure at the test location is changed by adjusting the breech volume and the number of and/or thickness of the Mylar membranes. Additional details of the experimental setup and the effects of various geometric parameters on the pressure-time profiles have been published extensively (Alay, Skotak, Misistia, & Chandra, 2017; Chandra et al., 2017; Kuriakose et al., 2016).

(a)

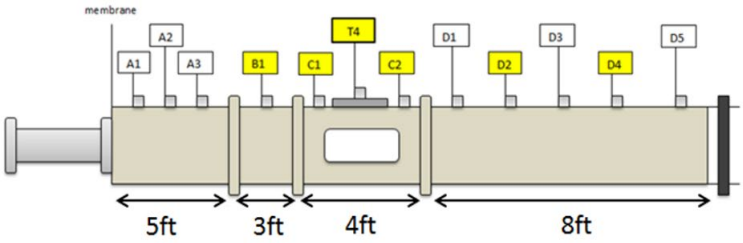

Sensor	Distance from End (inches)
D6	1.5
D4	21.5
D2	65
C2	104.5
T4	119.5
C1	134.5
B1	158.25

(b)

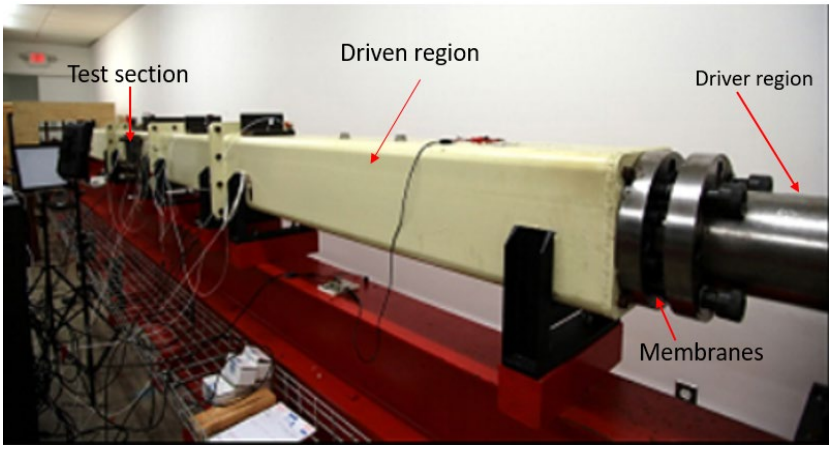

Figure 3.1. (a) Schematic of shock tube with sensor locations and distances; sensor locations marked yellow were used for data procurement (b) Shock tube setup in CIBM^3 facility

3.2 Finite Element Models

To determine the optimal method of shock wave generation, two methods were compared. In the first method, termed the truncated method, the shock tube was simulated downstream from one of the sensors (B1 in Figure 3.1). In this method, a pressure-time sensor reading at the truncation location was input into the numerical scheme as an impulse pressure wave. For this model, the geometry of the shock tube, the ambient temperature and pressure, and a sensor measurement would be necessary to generate the simulation of an experimental blast. This method is described in Section 3.2.1. The other method, termed the pressure release method modeled the entirety of the shock tube and simulated a region of high-pressure gas. This model needed the geometry of the shock tube, the ambient temperature and pressure, and the burst pressure to generate a simulation of an experimental blast. This method is described further in Section 3.2.2. In both cases, shock waves that were designed for a 100 kPa and 250 kPa overpressure at the test location were simulated and compared with experimental results. Comparison locations were selected to be all sensor locations downstream of B1, namely C1, T4, C2, D2, and D4. The simulated pressure-time profile was compared to the experimentally measured pressure-time profile. The experimentally measured and the simulated pressure-time profiles at each location were resampled to the same sampling frequency permitting the calculation of the percent error at each point. The mean percent errors are reported in Section 3.3.

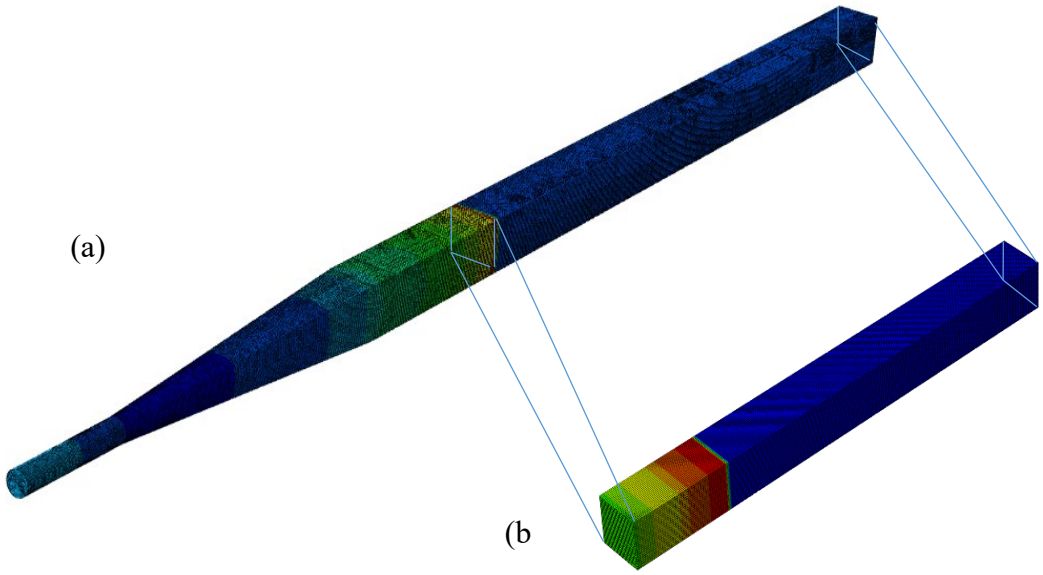

Figure 3.2. (a) The pressure release model with input based on experimental burst pressure measurements and (b) the truncated Model with input based on incident pressure profile at B1 sensor.

3.2.1 Truncated Model

For the truncated model, shock tube was simulated downstream from the B1 sensor to the end of the shock tube, making it a rectangular prism with dimensions of 229 x 229 x 4019.5 mm^3. The geometry was determined by examining different models from simulations of the whole room including the shock tube to the current model (see Figure 3.5). The shock tube was meshed using approximately 400,000 isothermal, reduced integration, linear, hexahedral Eulerian elements with hourglass control. The Eulerian domain was spatially discretized using a biased mesh with a minimum mesh density of 8 mm. This mesh density was identified from the results of a convergence study (Figure 3.4), where it was found that less than a 3% error was introduced into the system. The Eulerian domain was given the material properties of air at standard temperature and pressure conditions. The walls of the shock tube and the shock tube exit had all translational and rotational degrees of freedom

constrained, to prevent leakage. The pressure-time profile obtained from the B1 sensor readings (Figure 3.3) was used as the input. The model is shown in Figure 3.2 b.

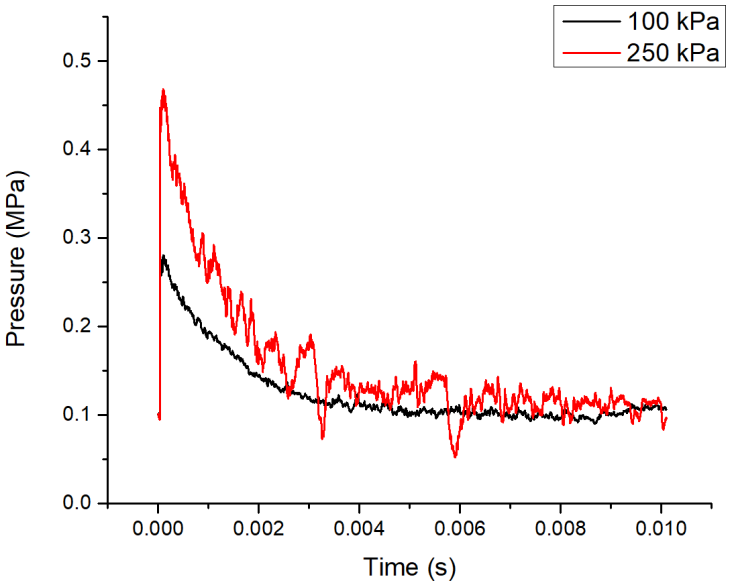

Figure 3.3. Pressure profiles for B1 sensor as input for truncated model

3.2.2 Pressure Release Model

This model was constructed with a closer accuracy to the experimental setup and included the driver region, the breech, and the transition sections (Figure 3.1). A breech length of 260.35 mm was simulated to match the experimental framework. The breech was followed by a 1.5 m long transition region of the driver section, changing from the circular cross section to the square cross section and extending downstream to the shock tube exit. The system was meshed with approximately 200,000 isothermal, reduced integration, linear, hexahedral Eulerian elements with hourglass control. This corresponded with the minimum mesh seed density of 25 mm, identified as the results of a convergence study. Elements inside the breech were defined as compressed gas (e.g. helium), while all other elements

were air. The burst pressures measured within the breech volume for the 100 kPa and 250 kPa shock waves were 742.5 kPa and 4272 kPa, respectively. As in the truncated model, all translational and rotational degrees of freedom at the walls and the shock tube exit were constrained to prevent leakage. Experimental measurements of burst pressure, ambient temperature, the breech volume, and the ideal nature of helium were used to calculate the density of helium at the given burst pressure. The model is depicted in Figure 3.2 (a).

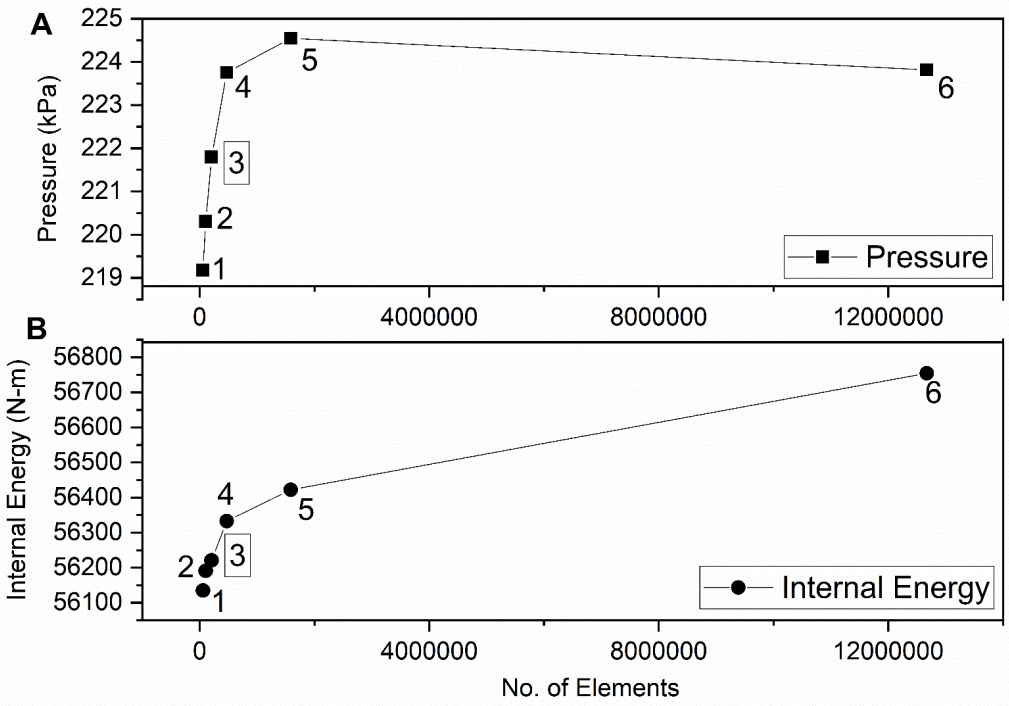

C

	Mesh Size (m)	No of Elements	Pressure (kPa)	Error (%)	Internal Energy (N-m)	Error (%)
1	0.012	58843.0	219.175	1.427	56134.9	1.092
2	0.01	103155.0	220.305	1.079	56190.8	0.993
3	**0.008**	**205204.0**	**221.795**	**0.621**	**56220.9**	**0.940**
4	**0.006**	**469300.0**	**223.755**	**0.018**	**56332.7**	**0.743**
5	0.004	1585512.0	224.545	-0.224	56422.5	0.585
6	0.002	1.3E+07	223.815		56754.4	

Figure 3.4. Convergence studies of the shock tube (A) The pressure in the shock tube was plotted against the corresponding element numbers (B) Internal energy in the shock tube vs corresponding element numbers. (C) Table with mesh sizes, Element numbers, Pressure, and Internal Energy with their errors. While the mesh size of 6 mm showed the best convergence, the 8 mm was determined to be the optimal mesh size due to its closeness in error to the 6mm, while maintaining acceptable run times.

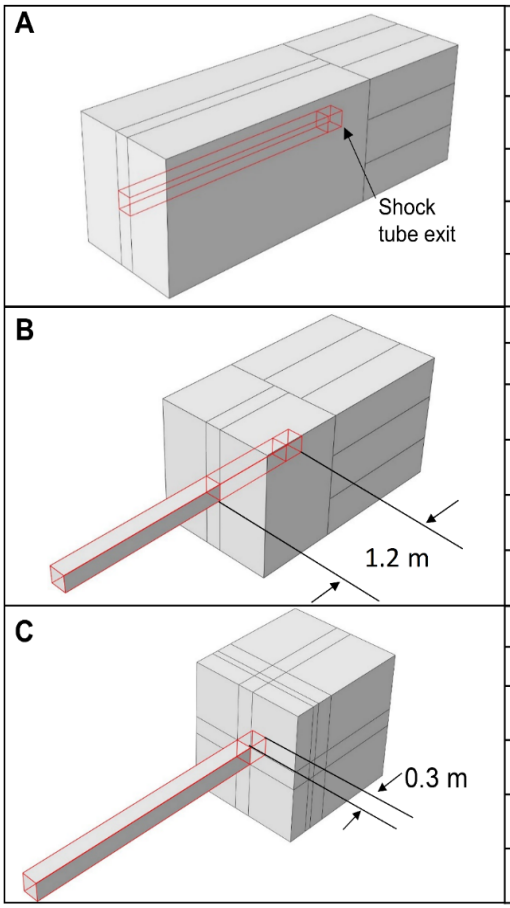

Whole Room	
Position	**Pressure (kPa)**
O1	181.34
O2	139.92
O3	121.76
O4	115.44

Partial Room		
Position	**Pressure (kPa)**	**% Error**
O1	179.67	0.920922
O2	138.5	1.014866
O3	121.63	0.106767
O4	115.18	0.225225

Room region only at the End		
Position	**Pressure (kPa)**	**% Error**
O1	175.53	3.203926
O2	134.35	3.980846
O3	117.48	3.515112
O4	111.04	3.811504

Figure 3.5. Selection of Room region in Simulations. Varying sizes of the room region the shock tube was in, were modelled. Measurements were taken at the four locations outside the shock tube (A) The room region encompasses the entire shock tube, allowing for the most accurate but also the most time consuming simulation (B) Here a partial section of the shock tube near the exit, and region outside the shock tube is modelled, allowing for shorter simulation run times. Here the errors compared to the whole room setup are around 1%. (C) The model consists of the shock tube, and the room region at the exit. It was found to have error of 3-4%. The partial room model was selected for the simulations because of its low errors and run times

3.3 Results

3.3.1 Truncated Model

The incident pressure profiles from exposures of 100 kPa and 250 kPa (Figure 3.6 and 3.7) for the truncated model were compared with experimental values for sensor locations inside the tube. Excellent correlation was seen between simulated and experimental pressure-time profiles in both the peak blast overpressure and the nonlinear decays, with error values of 5.64%±5.83% in the 100 kPa simulation and 6.45%±3.71% in the 250 kPa simulation. Error, in general, was lower for the lower severity test case of 100 kPa. The largest deviations were seen at the location corresponding with the D4 sensor at later time points in the pressure-time profile.

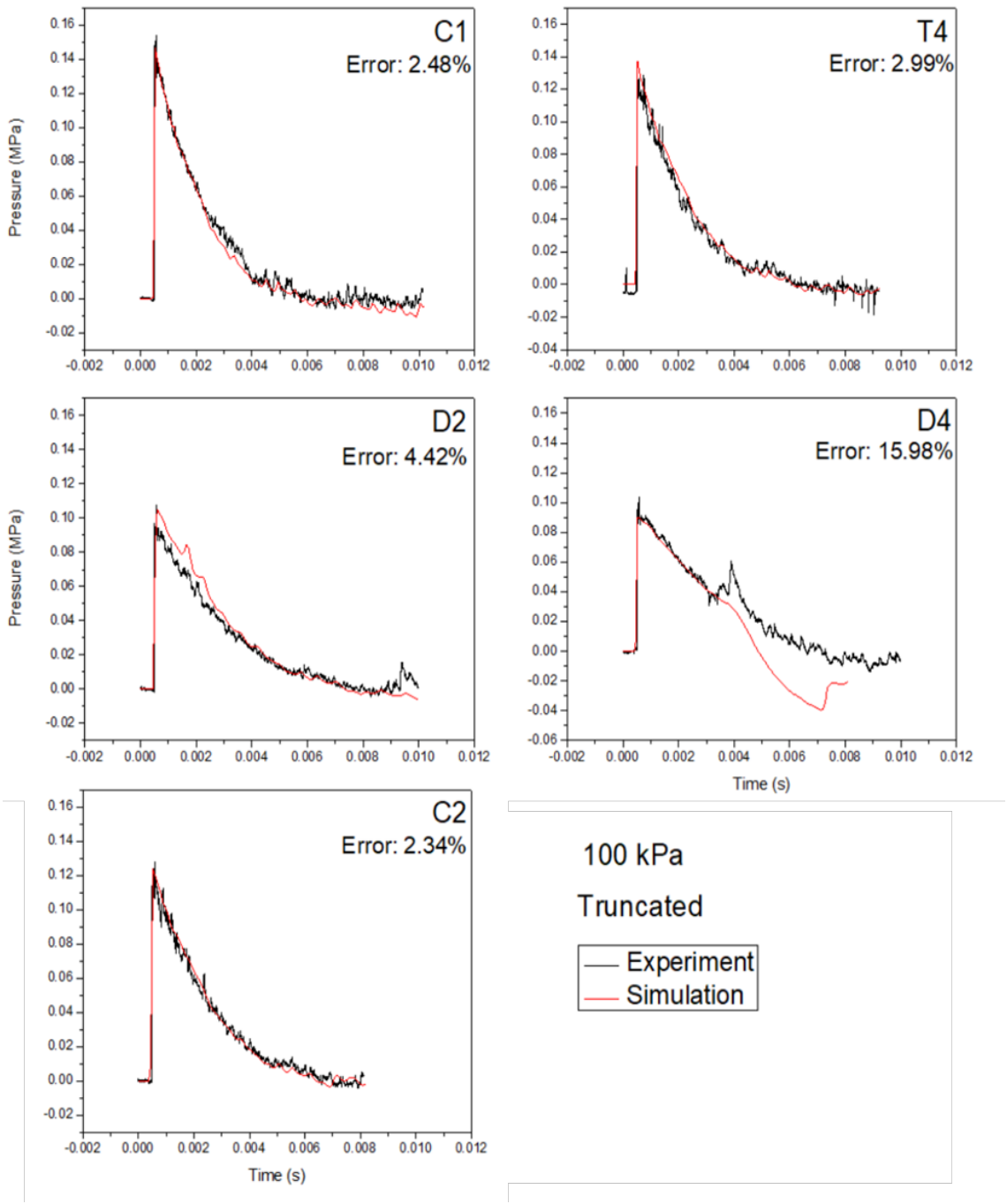

Figure 3.6. 100 kPa pressure inputs for the truncated method

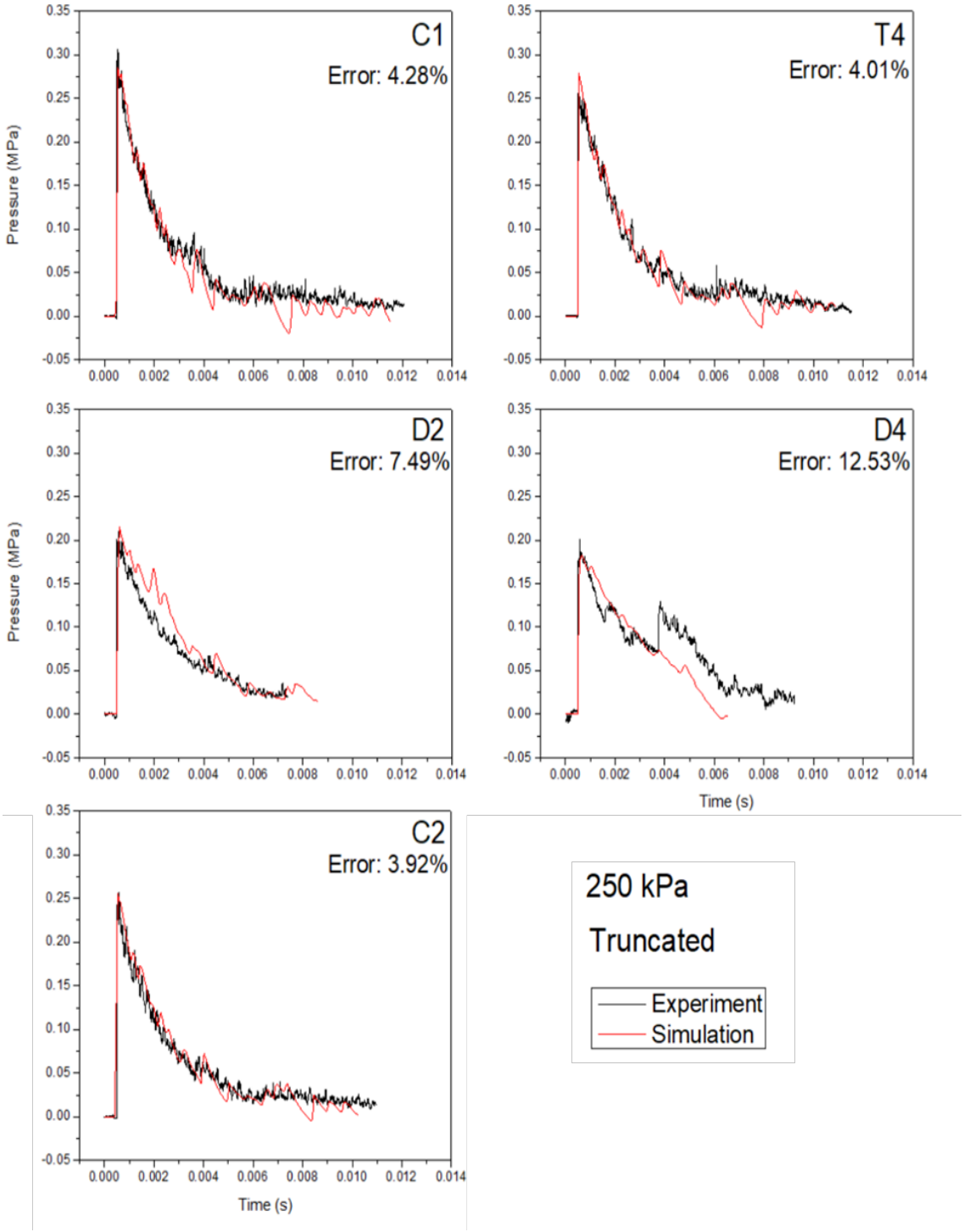

Figure 3.7. 250 kPa pressure inputs for the truncated method

3.3.2 Pressure Release Model

A comparison of simulated and experimental incident pressure-time profiles was conducted for the pressure release model at 100 kPa and 250 kPa (Figure 3.8, 3.9). Simulated pressures were lower in the 100 kPa blast, undershooting the experimental measurements by 13.7%±5.93%. The simulated pressures for the 250 kPa simulation overshot experimental values by 10.1%±3.28%. Additional peaks were observed in the D2 and D4 sensors for the 250 kPa. Simulation time was not long enough to resolve the entire nonlinear decay region of the D2 and D4 sensors in the 100 kPa simulation.

Table 3.1. Error Percentage for Truncated and Pressure Release Methods. SD – Standard Deviation

Sensor Location	**Error, %**			
	Truncated		**Pressure Release**	
	100 kPa	**250 kPa**	**100 kPa**	**250 kPa**
C1	2.48%	4.28%	-8.71%	8.91%
T4	2.99%	4.01%	-8.78%	8.76%
C2	2.34%	3.92%	-10.86%	8.84%
D2	4.42%	7.49%	-20.1%	8.11%
D4	15.98%	12.53%	-20.2%	16.0%
Mean±SD	5.64%±5.83%	6.45%±3.71%	-13.7%±5.93%	10.1%±3.28%

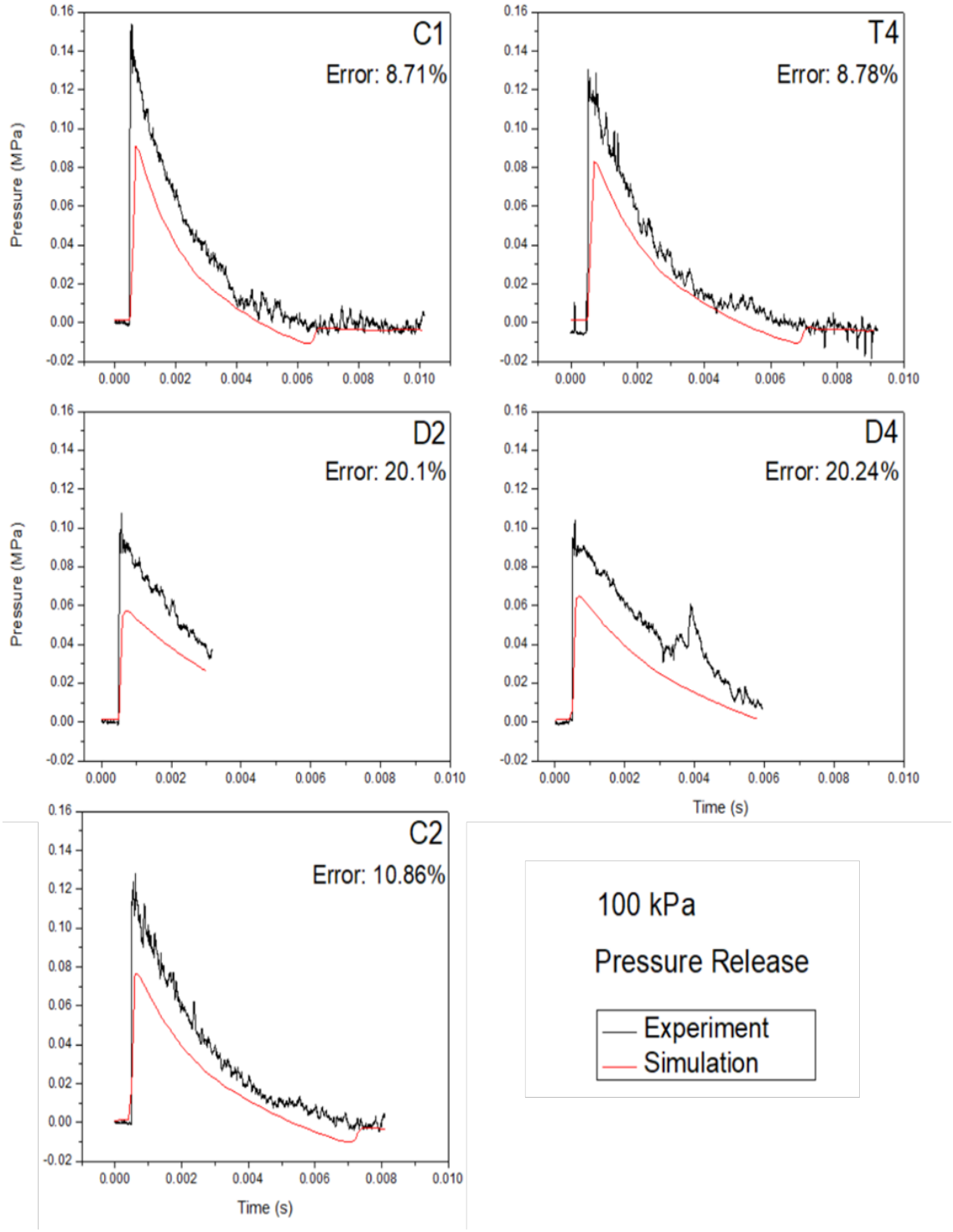

Figure 3.8. 100 kpa Pressure input for the Pressure release model

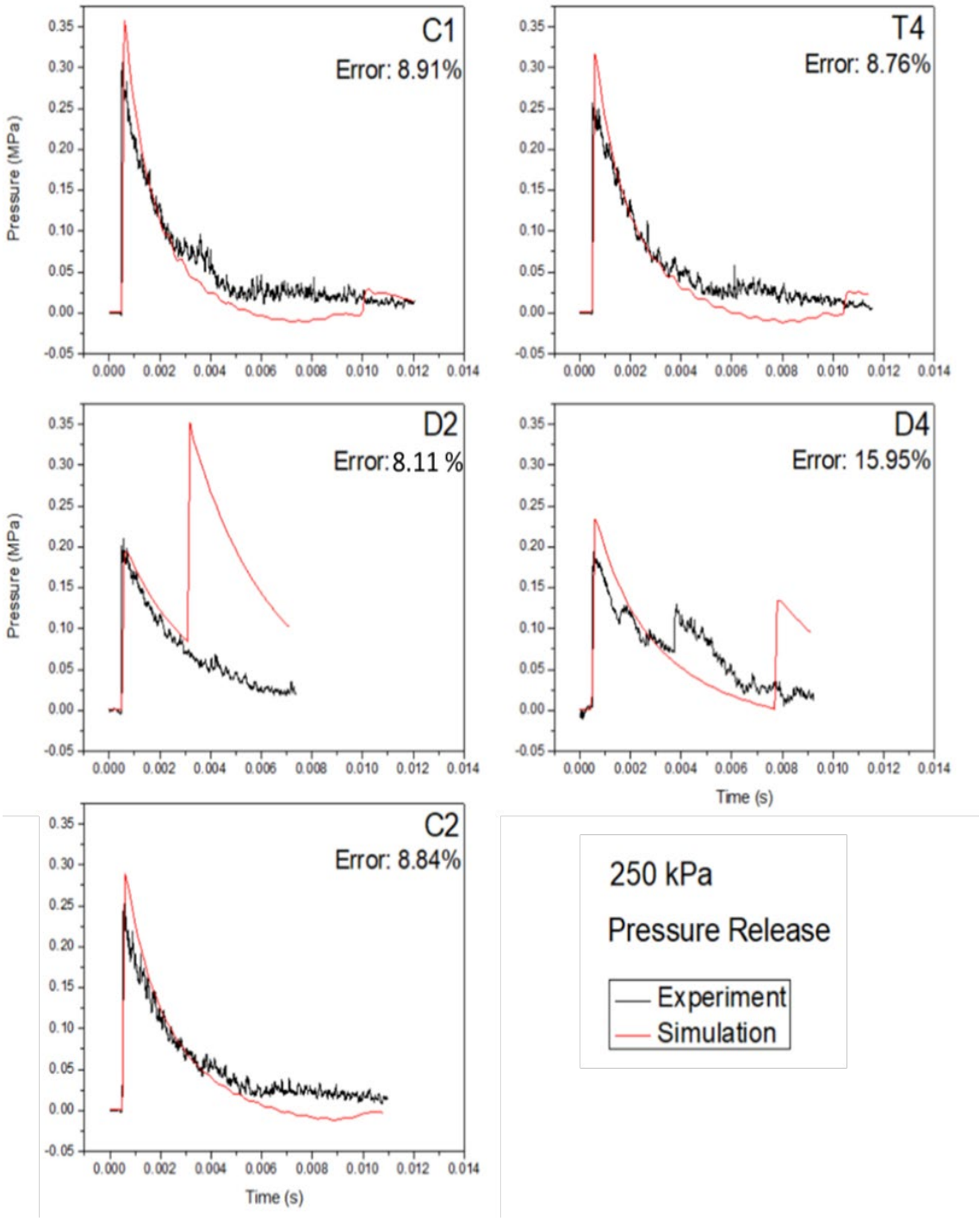

Figure 3.9. 250 kPa pressure input for the Pressure Release model

3.4 Discussion

The truncated and the pressure release model are two methods of shock wave generation. The truncated model uses the direct approach of using the experimental pressure profile data to directly generate the shock wave which propagates along the length of the tube. However, with this input, only experiments in which a sensor measurement is taken upstream can be simulated. The pressure release model aims to create the shock wave from the pressure of the gases, comparable to how the shock wave is generated in the experimental setting. This would eliminate the need for experimental sensor data, but it also has additional potential sources of error.

As the simulation significantly undershot and overshot the experimentally measured data, alterations to the pressure release model were considered. Some hypotheses were examined to see if the fit improves. As the membrane rupture does not completely clear the cross-sectional area, leaving approximately 14% of the cross section occluded, a membrane was simulated. This caused lower pressures, matching the 250 kPa data but severely undershooting the 100 kPa data. A mixture of helium and ambient air that would be consistent with filling the breech with 100% helium from an ambient air condition was tested but did not produce any improvement in the result. Similarly, the temperature change that would occur during breech volume pressurization was simulated, but this also produced no changes. These data are not included for brevity, and since these approaches were not pursued further.

The pressure release simulation was not long enough to capture the full nonlinear decay region of the pressure-time profiles in the D2 and D4 sensors at 100 kPa and

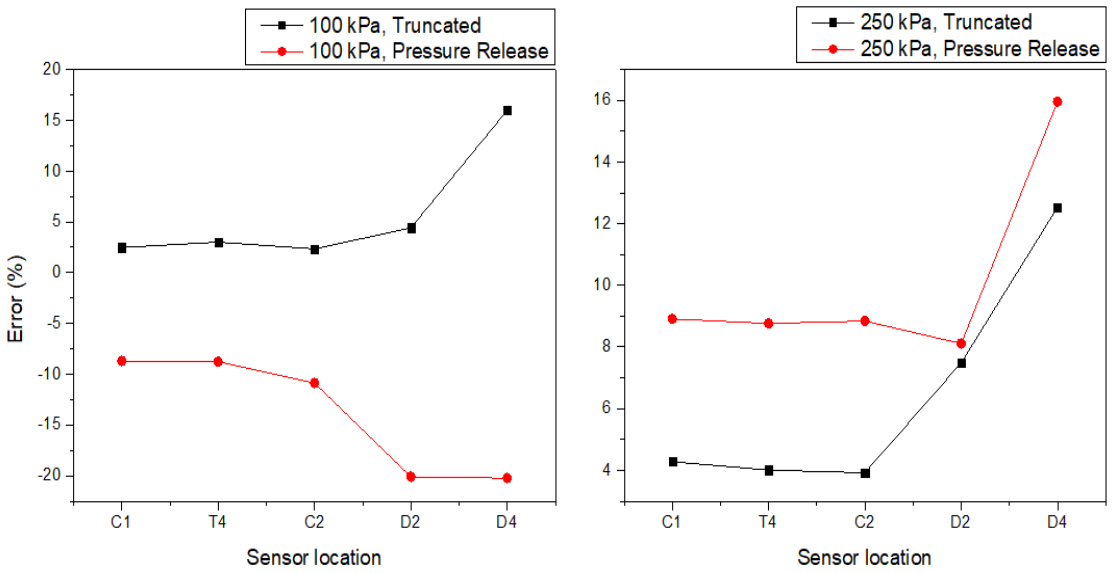

Figure 3.10. Percent error in comparing the incident pressure-time profiles between the truncated and pressure release methods for 100 kPa (left) and 250 kPa (right).

additional peaks were observed in the D2 and D4 sensors at 250 kPa. This is theorized to be due to the wave speed. The additional peaks are reflections that occurred from the hard contact with the end of the shock tube.

The truncated model exhibited a better match with the experimental data, with much lower error values compared to the pressure release model. This is theorized to be due to an increase of control over the system. Another potential explanation for the improved match would be the difference between the element sizes, with a smaller element size allowing for a better reproduction of shock wave propagation. As shock waves experience large variations in pressure over very small periods of time, having smaller element sizes will allow such gradations to be better visible. This hypothesis could be easily tested in the future by remeshing both models with the same element size but was considered beyond the scope of the proposed work, as an excellent match was observed with the current model. There is a deviation for the pressure profile at sensor D4 for the truncated model, which is due to the underpressure wave from the shock wave exiting the

shock tube (Chandra et al., 2012). As the truncated model depends on the experimental pressure profile to generate its shock wave, any errors introduced in the input would carry on to the results from the simulations.

In conclusion, the truncated model better simulates the experimental measurements of incident pressures for an empty shock tube. Therefore, in all subsequent work, the truncated model was used.

CHAPTER 4

CHARACTERIZATION OF SHOCK WAVE PROPAGATION IN SHOCK TUBE

4.1 Introduction

In this work, we have generated shock waves at three shock strengths which have been previously shown to generate mild traumatic brain injuries in animal models (Muneer 2013). For each of those conditions, we have made sixteen measurements of static and dynamic pressures in separate experiments. Additionally, we have developed a computational model to simulate the flow field produced in the shock tube experimental setup and validated the computational model against experimental measurements. Based on additional simulations, we have identified the temporal and spatial evolution of flow phenomena resulting from the free expansion of an unconstrained shock. It confirms the earlier evidence that experiments conducted outside of the shock tube do not ever reproduce the idealized flow field conditions of primary shock waves (Needham et al., 2015; Sundaramurthy et al., 2012).

4.2 Methods

4.2.1 Validation Dataset

The shock tube used in this work has been validated to reproduce free-field explosions within the test section accurately at sensor location I3 in Figure 4.1 (230 x 230 mm^2 square cross-section, 6 m in length) (Holmberg, 2010; Kuriakose et al., 2016). Briefly, compressed helium within a 55 cm length, 10 cm diameter chamber is separated from atmospheric-

pressure air by Mylar membranes. When the pressure differential causes the membranes to burst, a shock wave is formed which travels through a 1.5 m transition region to the driven region. Shock strength is dependent upon the thickness of the Mylar membranes. In this work, three thicknesses, 0.762, 0.457, and 0.152 mm, were used to generate a shock wave with overpressures within the test section of the shock tube of 180, 130, and 70 kPa. As this work seeks to study the evolution of the shock wave as a function of overpressure, the shocks will be referred to as a high, moderate, and low strength shock, respectively.

Incident pressures were measured within the shock tube at six locations (Figure 4.1A and 4.1C) using flush-mounted piezoelectric pressure sensors (Model 134A24, PCB Piezoelectronics). Additional incident pressure measurements and total pressure measurements were taken outside the shock tube, in line with the longitudinal axis of the shock tube as depicted in Figure 4.1A. The PCB 102B06 pressure sensors were mounted in an aluminum cylinder referred to as the sensing apparatus (61 cm length, 51 mm diameter, 6.4 mm wall thickness), rigidly attached to the shock tube support structure. Four pressure sensors were placed on the upper half of the sensing apparatus at four heights (H1-H4), with the H1 sensor aligned with the longitudinal axis of the shock tube and an inter-sensor spacing of 76 mm. The sensing apparatus was positioned at four locations offset from the exit (open end) of the shock tube, at 4, 16, 28, and 40 in (100, 410, 710, and 1020 mm; O1-O4). Total pressures were measured by orienting the pressure sensors so that the longitudinal axis of the pressure sensor was parallel to the longitudinal axis of the shock tube. Incident pressures were measured by rotating the sensing apparatus 90 degrees, such that the sensors were perpendicular to the longitudinal axis of the shock tube. Additional incident pressure measurements were taken within the shock tube at six locations along the

shock tube (I0, I2-I4, I6, and I8). Experiments were repeated four times (n=4) at each measurement location (O1-O4), for each measurement type (incident and total), at the three shock strengths (high, moderate, and low).

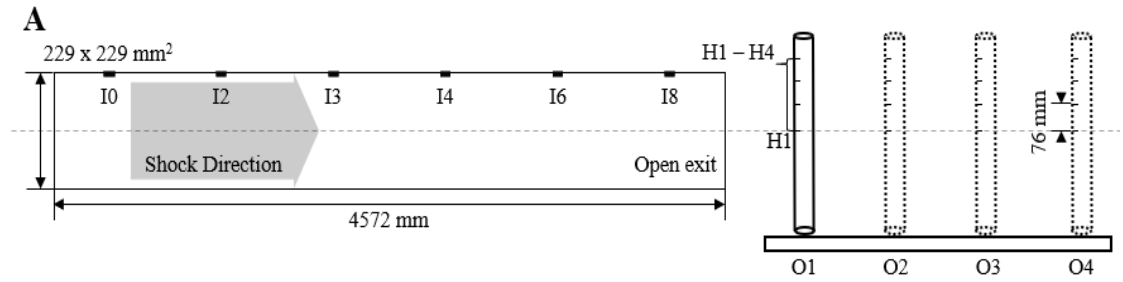

C

	Sensor	Distance from Shock Tube Exit
Inside	I0	-4.01 m
	I2	-3.43 m
	I3	-3.04 m
	I4	-2.65 m
	I6	-1.66 m
	I8	-0.55 m
Outside	O1	+0.10 m
	O2	+0.41 m
	O3	+0.71 m
	O4	+1.02 m

Figure 4.1. Schematic of the experimental setup used to create the validation dataset. (A) A shock tube with a square cross section was used in the development of the experimental dataset. Incident pressures were measured at six locations within the shock tube (I0, I2-I4, I6, and I8). Total and incident pressures were measured at four longitudinal locations outside of the shock tube (O1-O4) at four vertical heights (H1-H4). (B) A schematic representation of the experimental setup for the O1-O4 tests, with the sensing apparatus in the total pressure orientation. (C) The locations of all sensors with respect to the shock tube exit. Negative values denote upstream distances, into the shock tube, and positive values indicate downstream distances.

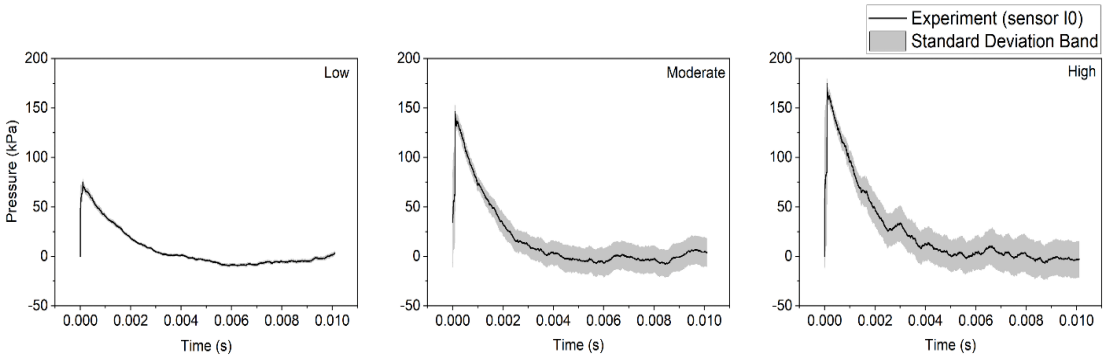

Figure 4.2. The average experimental measurements taken at sensor location I0. Grey bands indicate ± one standard deviation

4.2.2 Finite Element Model

The finite element method was used in this work to simulate the generation and propagation of the shock wave. A three-dimensional Eulerian model of the experimental setup was created and consisted of two continuous domains, a 4 m segment of the shock tube and a room region surrounding the exit of the shock tube (3.2 x 1.75 x 1.75 mm^3). The length of the shock tube was selected to simulate the portion of the shock tube located downstream from the first sensor location (I0). A sensitivity analysis was conducted to identify the dimensions of a room region which optimizes computational time and solution quality, where the shock wave would not be affected by any reflections from the boundary of the room (see Figure 3.5). The Eulerian domain was discretized using a biased mesh with a minimum element edge length of 8 mm at all regions of interest (see Figure 3.4). To validate the simulation, a Lagrangian model of the sensing apparatus was created to match the experimental setup. Figure 16A shows the shock tube, room region, and the sensing apparatus with the testing locations used for model validation. The Lagrangian domain offered a converged solution at an ideal mesh density of 6 mm (see Figure 4.4). This resulted in a system of approximately 3,600,000 Eulerian and 3,500 Lagrangian isothermal,

reduced integration, linear, hexahedral elements with hourglass control. The Eulerian domain was filled with 300 K air at a density of 1.225 kg/m^3. The sensing apparatus was modeled as aluminum, approximated to be linear, elastic, and isotropic with a density, elastic modulus, and Poisson's ratio of 2700 kg/m^3, 70 GPa, and 0.33, respectively.

A typical experimental pressure-time profile collected from the sensor I0 (Figure 4.3B) was used to model the shock wave. Although experiments were shown to be very reliable (see Figure 4.2), the pressure-time pulses of a minimum of four exposures were averaged for each shock severity to minimize the effect of any measurement artifacts. The edges of the room and shock tube were constrained in all translational and rotational degrees of freedom (Figure 4.3A). The open exit of the shock tube was unconstrained, allowing for the unimpeded flow of the shock wave from the shock tube into the room region.

Simulations to derive the incident pressures were conducted without the sensing apparatus model in a purely Eulerian simulation. Total pressure simulations were conducted with the sensing apparatus. In the total pressure simulations, all nodes located at the bottom of the sensing apparatus were constrained in all translational and rotational degrees of freedom. The contact between the Lagrangian and Eulerian domains is based on an enhanced boundary method. Here, the void mesh of the Eulerian domain is occupied by the Lagrangian structure. The general contact algorithm automatically tracks the interface between the domains, compensating for mesh size discrepancies to prevent the entry of Eulerian material through the Lagrangian surface. Contact constraints are enforced through

the penalty method with a finite sliding contact formulation. The total pressure simulations use frictionless tangential sliding with hard contact.

4.2.3 Methodology

Overall, thirty-nine simulations were conducted, three incident pressure simulations, one for each shock strengths (low, moderate, and high), and thirty-six total pressure simulations at three shock strengths for twelve locations. Additional locations were identified to better map the shock tube system, including seven locations inside the shock tube (I1-I8), two locations near the exit of the shock tube (E0 and E1), and four locations outside the shock tube (O1-O4). Exact locations of the additional measurements are included in Figure 4.3C. First, validation was conducted in which the shock wave pressure-time profiles were compared to the experimental measurements. The peak overpressure, impulse, duration, and general form of the total and incident pressure-time profiles were compared to ensure validation of the simulation. Upon validation, the simulation results were analyzed to identify potential flow phenomena.

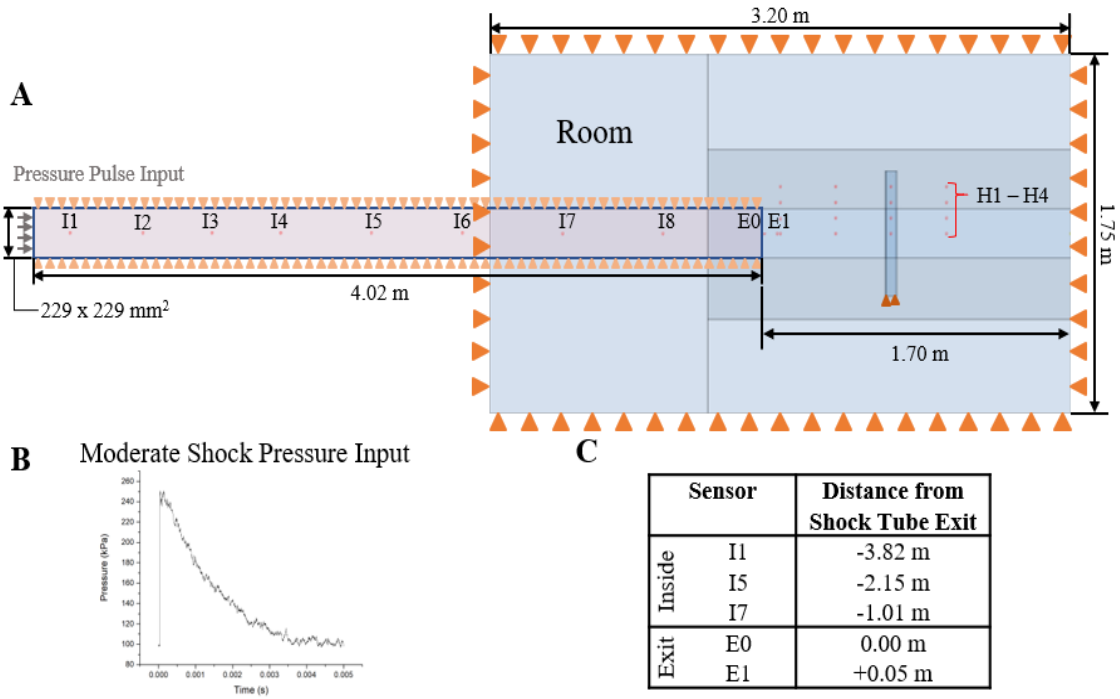

	Sensor	Distance from Shock Tube Exit
Inside	I1	-3.82 m
	I5	-2.15 m
	I7	-1.01 m
Exit	E0	0.00 m
	E1	+0.05 m

Figure 4.3. Schematic of the experimental simulation setup. (A) A depiction of the modeling domain, consisting of the sensing apparatus and the shock tube and room region with boundary conditions. Orange triangles indicate boundaries which are constrained. (B) An example of the pressure-time amplitude used to induce the moderate shock wave, which consists of the average pressure measured at sensor location I0 (n=4). (C) A table of additional sensor locations which were included in the numerical simulations. The sensor locations are reported with respect to the shock tube exit. Negative values denote upstream distances, into the shock tube, and positive values denote downstream distances.

4.3 Results and Discussions

In the discussion below, the evolution of a shock wave at the exit of a shock tube is presented, including the discussion of how the shock wave decays in strength and induces several flow phenomena. First, the observations from the experimental measurements will be presented and the numerical simulations will be validated. Then, the numerical model, supported by experimental measurements when possible, will be used to discuss several metrics used to define the health of the shock wave.

First, the shock is observed to be planar within the shock tube and spherical outside of the shock tube. The shock tube constrains the shock wave, maintaining the planarity of the wave until the shock front experiences rapid expansion into the ambient air within the room. Next, the peak pressure decays as the shock wave propagates, decreasing slowly while inside the shock tube and decreasing rapidly upon exiting the shock tube. Finally, two flow phenomena were generated from the rapid expansion of the shock front at the shock tube exit: a vortex ring and a rarefaction wave. The vortex ring propagates behind the shock wave at a slower velocity that is dependent on the shock strength. The rarefaction wave reflects into the shock tube, decreasing the positive phase duration and the impulse. These metrics of shock health highlight the regions of the shock tube experimental setup which experience an ideal shock wave and those which interact with a vortex ring and a rarefaction wave.

4.3.1 Experimentally Observed Incident and Total Pressures

Experimental measurements of the shock overpressure outside the shock tube exit identified two distinct flow phenomena (Figure 4.4). First, the shock front arrives, characteristically observed as a rapid increase in overpressure and an exponential decay to baseline in which the total pressure is proportionally higher than the incident pressure reading. The difference between shock front arrival time can be used to calculate the shock velocity, which is confirmed to be higher in higher shock intensities and gradually slows as it propagates in the ambient air outside the shock tube. The peak overpressure of the shock front decreases as the distance from the shock tube exit increases. Additionally, the peak overpressure decreases with increased distance from the midline, i.e., normal to the

direction of shock wave propagation. This trend is less pronounced as the distance from the shock tube exit increases.

The second distinct flow phenomenon arrives after the shock front and is characterized by a slow increase in the total pressure and decrease in the incident pressure, resulting in an incident underpressure, or pressure less than atmospheric pressure. At a distance closest to the shock tube exit, O1, the flow artifact occurs shortly after the shock passes. This artifact is observed to travel at a slower velocity than the shock front, moving at a subsonic velocity with a magnitude proportional to the shock severity. This flow phenomenon was observed at sensor locations H1-H3 and the highest sensor measurement location, H4, showed an underpressure in both the total and incident pressures.

A few general trends can be observed in Figure 4.4. by comparing the peak overpressure, positive phase durations, and the impulse at the four vertical locations (H1-H4) at the four longitudinal sensing apparatus measurement locations (O1-O4). Trends are conserved between the three shock strengths examined, differing only in magnitude (Figure 4.5). Peak overpressure, duration, and the magnitude of the impulse increased with shock strength. Over the duration of the pressure signal, under pressures resulted in negative impulse values in all sensor locations in the incident waveform and in the O4 total pressure measurement. The total pressure measurement orientation exhibited higher peak overpressures and impulses in all cases. As longitudinal distance from the shock tube exit increased (O1-O4), peak overpressure and impulse decreased. There exhibited no significant change in incident pressure duration and the total pressure duration decreased with increasing longitudinal distance. As the vertical distance increased from the

longitudinal axis (H1-H4), the peak overpressure decreased, with the magnitude of the reduction decreasing with longitudinal distance. Significance was not observed between the H1 and H2 sensors in the incident pressure measurement at O4. The duration of the total pressure signal increased in the off-axis locations.

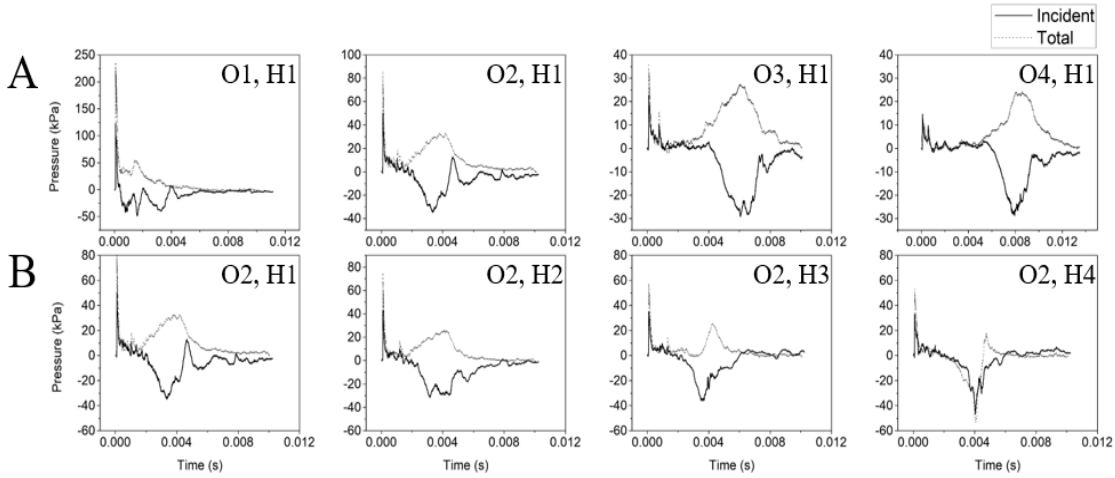

Figure 4.4. Measurement location along the longitudinal axis (O1-O4) and the vertical axis (H1-H4) changes the characteristics of the pressure measurements. (A) The experimentally measured total (grey) and incident (black) pressures at the four measurement locations O1-O4 at sensor location H1 highlight a reduction in the peak overpressure and a delay in the arrival of the secondary flow phenomena as the distance from the shock tube exit increases. (B) Likewise, when comparing the pressure profiles vertically (H1-H4) at a single longitudinal location, O2, shows a change in the nature of the secondary flow phenomena.

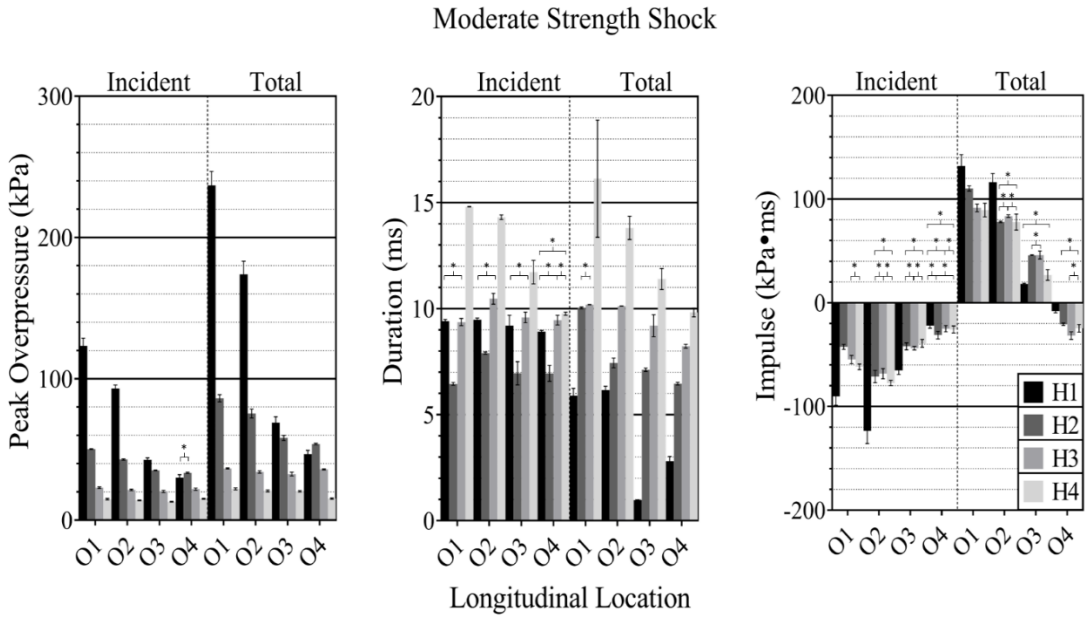

Figure 4.5. Pressure profile characteristics of the incident and total pressures**.** The peak overpressure (left), signal duration (middle), and impulse (right) of the experimentally measured incident, and total pressure pulses for the moderate-intensity shock wave showed several trends.

4.3.2 Validation of Computational Model

The simulations were validated against the experimental datasets through a comparison of the pressure-time waveforms, the peak overpressures, impulses, rise-times, and durations. The simulations, on average, underestimated the peak overpressure and overestimated the rise time, which is attributed to a sampling rate and an element density which were not adequate to resolve the shock front location. The simulations were sampled at a frequency of 26 kHz. Experimentally, sampling frequencies of a similar range have been shown to be sufficient to resolve the peak overpressure and overestimate the rise time of the signal (Skotak, Alay, & Chandra, 2018). However, low sampling frequency coupled with spatial discretization reduces the ability to capture the shock front location. For the shock strengths

simulated, the velocity of the shock front is in the range of 345-518 m/s (low to high strength) which would enable the shock front to traverse an 8 mm element in the range of 15.5-20.4 μs, respectively. To accurately resolve the shock front at that spatial density, a sampling frequency in the range of 98.3-129 kHz would be required and would increase the number of sampled frames by an unrealistic factor of 1.9-2.5. Despite the underprediction of the peak pressure, average point-by-point percent error between the experimental and simulated pressures were under 6% for all incident pressures within the shock tube and under 12.5% for all incident and total pressure measurements taken outside of the shock tube (Figure 4.6). On average, the best match was observed at locations closer to the input location, I0.

Simulation results matched the impulse and duration of the shock front, but incident pressure simulations did not exhibit a negative impulse, as seen in the experimental measurements (Figure 4.5). Several methods of simulating the incident and total pressures were compared, indicating that the decrease in pressure was likely due to the interactions between the secondary flow phenomenon and the cylindrical sensing apparatus (Figure 4.7). In general, a comparison of the pressure-time waveforms revealed an excellent match, meaning that the simulation can be considered validated with conservative blast overpressure estimates.

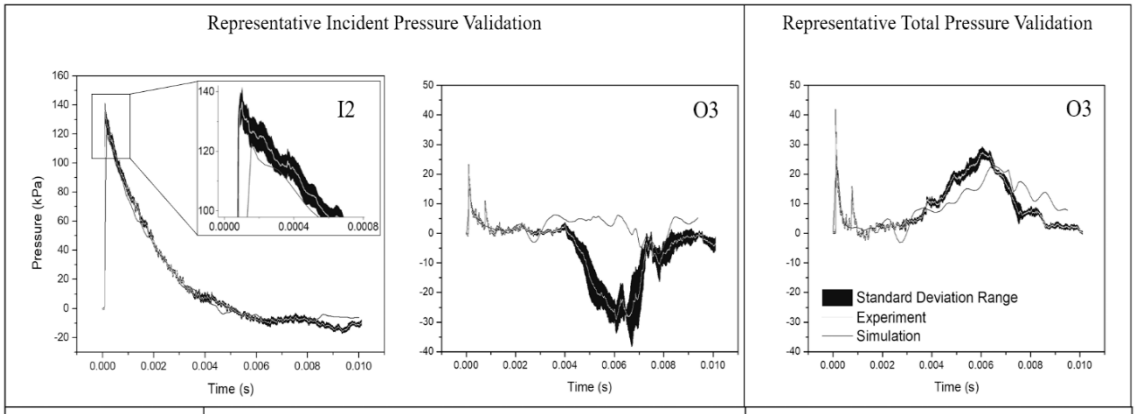

	Incident Pressure Percent Difference		Total Pressure Percent Differences (Outside Only)
	Sensors Inside Shock Tube	Sensors Outside Shock Tube	
Low Strength	5.6 ± 2.6%	10.6 ± 3.2 %	10.7 ± 3.9 %
Moderate Strength	5.2 ± 2.2%	10.7 ± 2.3%	10.4 ± 3.6%
High Strength	6.1 ± 2.4%	12.4 ± 3.1%	12.3 ± 3.6%

Figure 4.61. Simulation predictions compared to experimental results for the high-strength shock. The simulated pressures (grey) showed good validation with the average experimentally measured pressures (black with grey, mean, with standard deviation) for the incident (left and middle) and total (right) pressure measurements for the high strength shock. The point-by-point percent error for the shock front was under 12.5%. Average errors for interior locations (I2-I4, I6, and I8) showed the best validation.

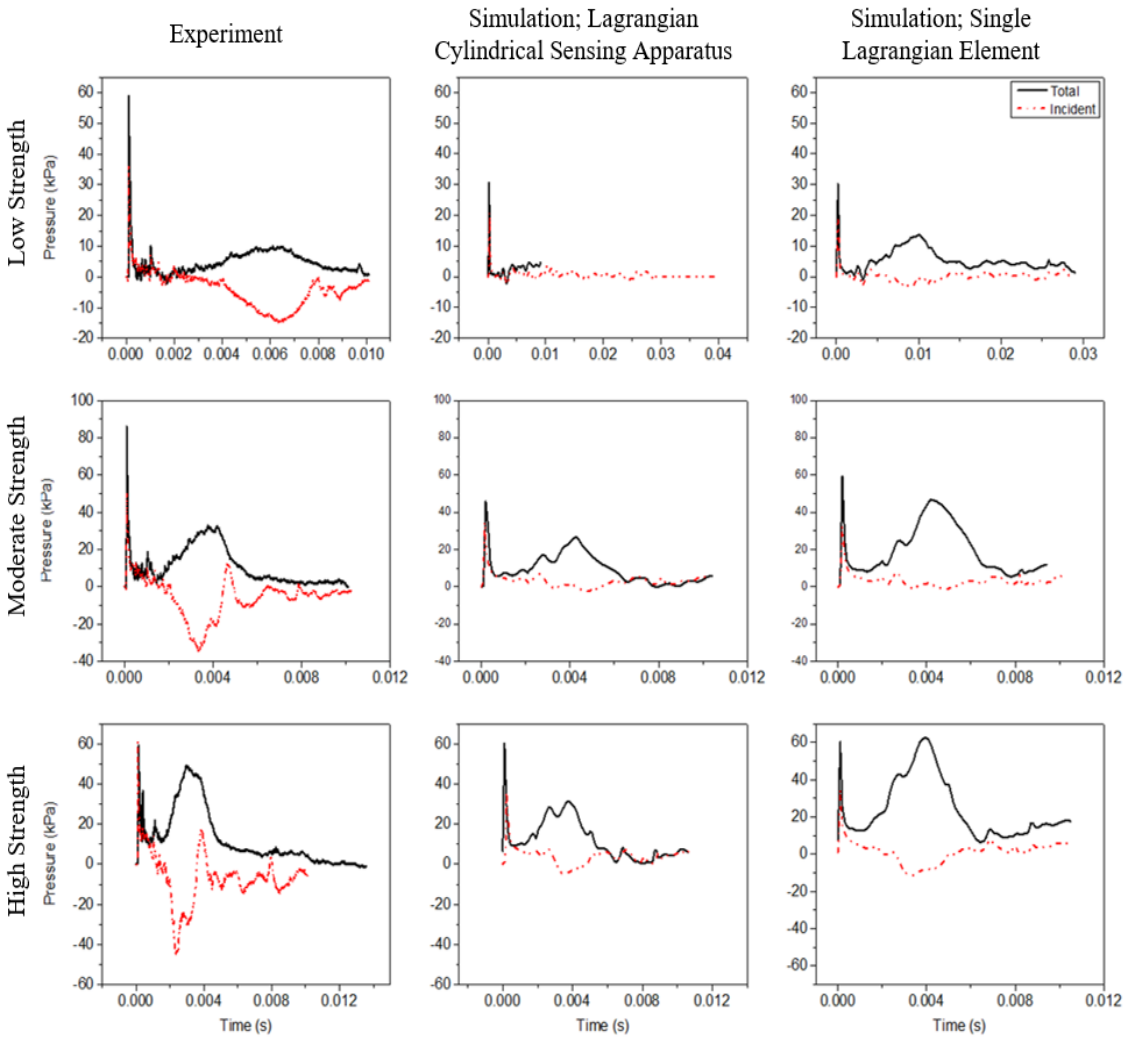

Figure 4.7. A comparison between different methods of simulating the incident pressures. Simulations using the cylindrical sensing apparatus to simulate the incident pressure measurements exhibited a larger underpressure. Experimental data showing difference between the Incident pressures and Total pressures showing the range for dynamic pressures

4.3.3 Peak Overpressure

The shock pressure ratio, defined as the ratio of the pressure within the shock front and the ambient pressure, decreased slowly as it propagated through the shock tube and rapidly upon sudden expansion into the room region (Figure. 4.8). The rate of decay varied with shock intensity, with the high strength shock pressure ratio decaying the most rapidly. The shock pressure ratio decreased within the shock tube at an average rate of 0.09, 0.19, and 0.22 for the low, moderate, and high strength shocks, respectively. The peak pressure at the shock tube exit was 30.99%, 33.33% and 34.15% of the input peak overpressure for the low, moderate, and high strength shock. These results are in line with previous findings from our group, which states that the peak pressure decays as the shock wave propagates down the shock tube (Kuriakose et al., 2016; Skotak et al., 2018). Energy loss in a shock tube has been hypothesized to be due to viscous effects at the shock tube walls, modeled in the numerical simulations by a no-slip boundary condition (Emrich & Curtis, 1953; Slepička, 1966). Additional energy dissipation is also theorized to occur from the expansion of the high-pressure shock front, increasing the shock duration while maintaining a comparable impulse, reducing the energy of the shock front (Kuriakose et al., 2016).

Shock wave expansion at the shock tube exit decreased the shock pressure ratio rapidly, with the average rate of decay increasing to 0.55, 1.00, and 1.19 and an average peak rate of decay of 2.65, 4.96, and 6.03 for the low, moderate, and high strength shocks, respectively. Outside of the shock tube, the pressure decayed rapidly, reducing 92.96%, 94.33%, and 94.51% for the low, moderate, and high strength shocks, respectively. This rapid decay in overpressure is consistent with an increased area of the shock front as the

shock front experiences expansion into the ambient air (Abate & Shyy, 2002). A relationship between the shock strength and the area of the shock front using the function derived by Chisnell (*f(z)*) which, when multiplied by the area of the shock front (*A*), remains constant (Chisnell, 1957). As the area of the shock front increases, the Chisnell function decreases, accordingly, and is given for a shock in diatomic air by (Chisnell, 1957)

$$f(z) = \frac{z^{\frac{5}{7}}(z-1)}{\sqrt{z+\frac{1}{6}}}\left[\frac{1+\left(1+\frac{6}{z}\right)^{-\frac{1}{2}}}{1-\left(1+\frac{6}{z}\right)^{-\frac{1}{2}}}\right]^{\sqrt{7}/2} \times \left[\frac{\left(1+\frac{6}{z}\right)^{-\frac{1}{2}}-7^{-\frac{1}{2}}}{\left(1+\frac{6}{z}\right)^{-\frac{1}{2}}+7^{-\frac{1}{2}}}\right] \times e^{\left(\sqrt{5}\tan^{-1}\left(5\sqrt{\frac{7z}{5(z+6)}}\right)\right)}. \quad (4.1)$$

This function is derived from the Rankine-Hugoniot equations and has been proven to accurately model symmetrical, spherical and cylindrical shocks experiencing rapid, unconfined expansion between two square or circular chambers of similar or very different cross-sectional areas(Chisnell, 1957; Skews, 1967). When used in conjunction with the area of the shock front given for a spherical shock by

$$A = 2\pi X^2. \quad (4.2)$$

where *X* is the longitudinal distance from the exit of the shock tube after which a critical shock is formed. It can be calculated from the shock tube diameter (*d*) and the angle of propagation (α) by

$$X = \frac{d}{2}\cot \propto. \quad (4.3)$$

Using a relationship between the angle of propagation and the Mach number, given by

$$\tan^2 \propto = \frac{(M^2-1)(M^2+5)}{6M^4}. \quad (4.4)$$

a relationship describing the loss in shock pressure ratio due to expansion can be derived. Using this theory for the conditions studied here, the rapid decay of the shock pressure ratio

is explained by the increase in the area of the shock front. As the shock front area increases and continues to expand, the shock pressure ratio exponentially decays.

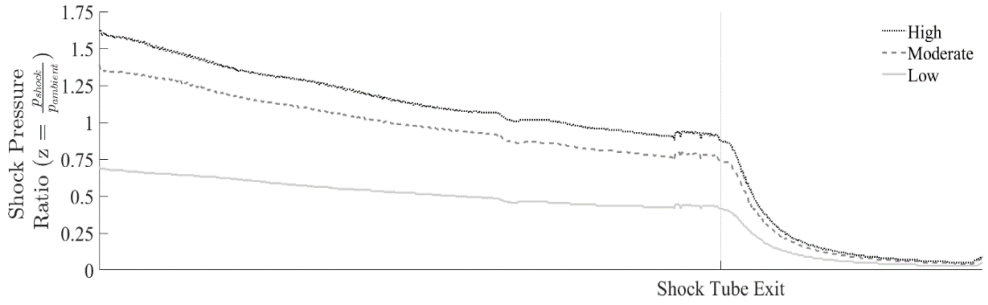

Figure 4.8. The shock pressure ratio along the longitudinal axis. The shock pressure ratio, z, defined as the ratio of the shock front, pshock, to the ambient pressure, pambient, decays gradually along the shock tube and declines rapidly after expansion begins at the shock tube exit. The rate of decay within the shock tube and the following expansion was found to depend on the shock strength.

4.3.4 Shock Planarity

As the simulated shock propagated through the shock tube, it remained planar. At the shock tube exit, the shock front experienced sudden, unconstrained expansion into the still ambient air. At this point, the simulation shows the shock front became less planar, expanding, and becoming more spherical. As the shock front propagated, it eventually regained some planarity (Figure 4.9).

This simulated phenomenon was confirmed experimentally by examining the shock front arrival times at each sensor. At all longitudinal measurement locations (O1-O4), the shock wave arrived at the sensor aligned with the longitudinal axis first (H1). At the measurement location closest to the shock tube exit, the center of the shock front remains mostly planar. When comparing the elapsed time between the shock wave arrival, little difference was observed between the two sensors closest to the longitudinal axis, H1 and

H2. The arrival of the shock front at H2 was delayed an average of 2.75±0.98 μs. The shock wave curvature is apparent in the much higher arrival time delays at the sensors located farther from the midline, with H3 and H4 being delayed by 55.25±1.91 μs and 187.33±2.12 μs, respectively. This demonstrates that the shock wave is only beginning to lose planarity at this location. The curvature of the shock wave is more apparent at the O2-O4 longitudinal measurement locations, where the shock curvature is more even (Figure 4.10). The curvature is highest at O2, then starts decreasing to O4. The shock front arrival time delay was mostly independent of the shock strength. A slight trend was observed where a high-strength shock exhibited a slightly longer delay. This trend was most apparent at the O1 location, and the strength of the trend decreased with the distance from the shock tube exit. The shock front travels at a faster speed in the higher strength shock and, therefore, the shock front will be less planar than a low strength shock, despite there being little to no difference in the shock front arrival time delay.

These observations highlight that the shock front was behaving in line with previous experimental results of sudden shock wave expansion, further validated by the theory. Using the relationship in equation 4.5, the Mach number of the shock wave as it exits the shock tube can be used to predict the angle of propagation of the critical shock, predicting the point at which planarity of the shock front decays. The difference in the experimentally measured arrival times of the shock front between the I8 and O1 and the distance between those measurement locations were used to calculate the shock velocity (v) and the Mach number, using the relationship

$$M = \frac{v}{c}, \tag{4.5}$$

where the speed of sound, c, was assumed to be 343 m/s. At the measurement location O1, the angles of propagation for the shock strengths investigated in this study are 69.5, 62.9, and 61.8 mm for the low, moderate, and high strength shocks, respectively. This indicates that the limits of the planar area fall between the H1 and H2 sensors (76.2 mm) for all three shock strengths at the O1 location, as demonstrated by a lack of curvature seen in Figure 4.10A. The shock front plane in which the shock loses the original planarity, occurs between 222-374 mm for the shock strengths examined in this study. Therefore, by the O2 longitudinal measurement location, the shock front no longer retains any planarity and decays completely, referred to as a "critical shock". As the shock expands into the ambient air, the shock undergoes diffraction and expands freely around the sharp edge of the shock tube exit. This shock front which undergoes diffraction interacts with the planar shock front, causing the planar front to decay into a critical shock. This interaction creates an expansion wave which propagates longitudinally upstream into the shock tube (Abate & Shyy, 2002). The expansion wave, or rarefaction wave, will be described in detail in a later section.

Following the complete decay of the planar shock front into a critical shock, the critical shock front was observed in the simulations to propagate at a much lower strength and, eventually, become more planar in nature. This is theorized to be due to the initial uneven expansion of the wave into a critical shock and due to interactions of the shock front with the boundaries of the room region. As the cross-section of the shock tube investigated here is not of a circular diameter, the planar region will decay in a non-axisymmetric manner. The narrower cross section at the mid-wall of the shock tube will have a smaller planar area than the widest cross-section, at a diagonal cut. The non-

axisymmetric decay will cause the behavior of the critical shock to deviate from the ideal behavior of a spherical shock. Additionally, as the critical shock continues to expand, the increase in the shock area will eventually interact with the boundaries of the domain. At the domain walls, the interaction of the critical shock with the wall creates an oblique reflected shock, which interacts with the critical shock front (Kinney & Graham, 1985). The oblique reflected shock increases the strength of the critical shock, which decreases the apparent curvature of the shock front at the edges of the domain. As the domain of the room region in the computational model was not designed to completely replicate the room in which the experiment was conducted, it is anticipated that the curvature of the shock predicted in the simulation would differ from experimental conditions. However, as the region of interest tested by the sensing apparatus was small in comparison with the room region, it is hypothesized that any differences would only be apparent at the longitudinal measurement locations farthest from the shock tube exit.

Figure 4.9. The planarity of the shock front is largely lost at the shock tube exit. The edge of the shock front at each time step (Δt = 38.5 μs) from t = 0-13.5 ms in the moderate strength shock in a mid-wall (top) and diagonal cut (bottom). As the shock exits the shock tube, denoted by a grey bar, the shock front loses its planar nature and expands, becoming more spherical.

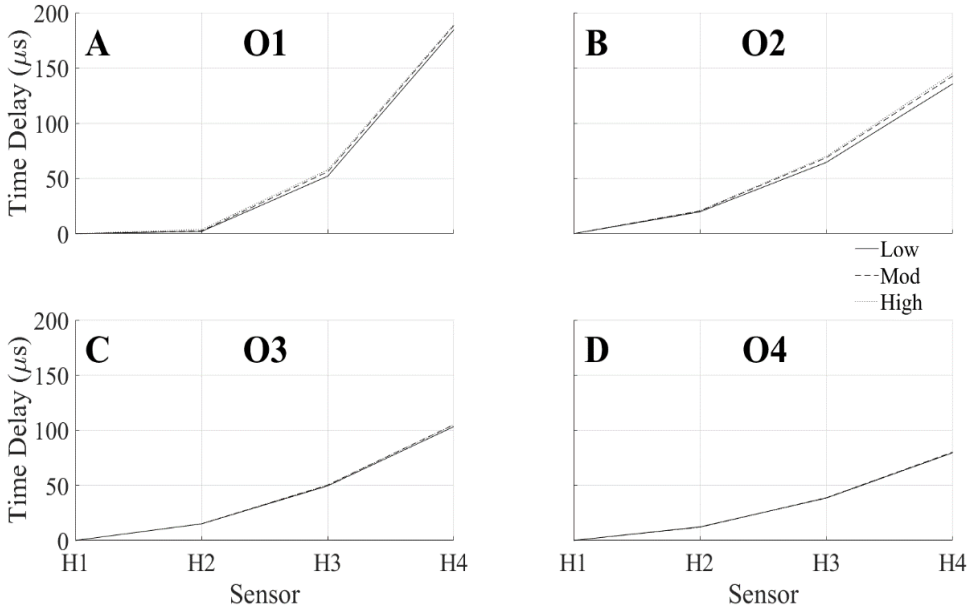

Figure 4.10. Experimentally observed shock curvature. The arrival times of the shock wave normalized with the shock arrival at the H1 sensor showed a curvature of the shock front at the measurement locations (A) O1, (B) O2, (C) O3, and (D) O4.

4.3.5 Vortex Ring

Following the shock front, the secondary flow phenomenon observed in the experimental results was identified as a vortex ring. A vortex ring is formed as the fast-moving volume of compressed air moves into stationary air. Viscous friction slows down the interface between the two media. The slowed air then moves around the mass of compressed air, then rejoins the fast-moving air, forming a toroidal ring. The simulation showed the rotating ring forming at the exit of the shock tube and follows the shock front at a slower velocity. The velocity of the vortex ring was dependent on the shock severity, where the highest strength shock produced a vortex ring which propagates at 90.6 m/s; and with decreasing shock strength, the velocity decreased to 79.8 and 40.3 m/s for the moderate and low strength shocks, respectively. The path of the vortex ring also varied with shock

severity (Figure 4.11). Following the formation of the ring, the vortex ring follows the shock front and the diameter of the vortex ring core at the mid-wall increases to match the diameter of the vortex ring core at the corners. The ring over-expands and comes back to reach a more stable diameter. The diameter of the ring itself increases as it forms and reaches a relatively stable size. The lower severity shock exhibited a reduction in ring size as it propagates, indicating that the ring may have begun to dissipate.

At the time of arrival of the vortex ring, an increase in total pressure was observed experimentally and confirmed in the simulation results. A jet of air behind the shock front exists within the core of the vortex ring. This jet of air arrives with the vortex ring, and the air particles within the jet of air are stopped by an object in the path, resulting in an increase in total pressure. The structure of the vortex ring means that the pressure profile varied for each vertical measurement (Figure 4.12). Along the longitudinal axis, at vertical location H1, the center of the ring accelerated air, which caused the largest total pressure impulse. The impulse decreases with increasing vertical distance, as the sensing location approaches the center of the vortex ring. The vortex ring itself has an underpressure region within the vortex core, where the pressure is falling below atmospheric pressure (Jiang, Onodera, & Takayama, 1999). The H4 sensor location is closest to the vortex core and characteristically drops in pressure as the vortex ring interacts with the testing apparatus.

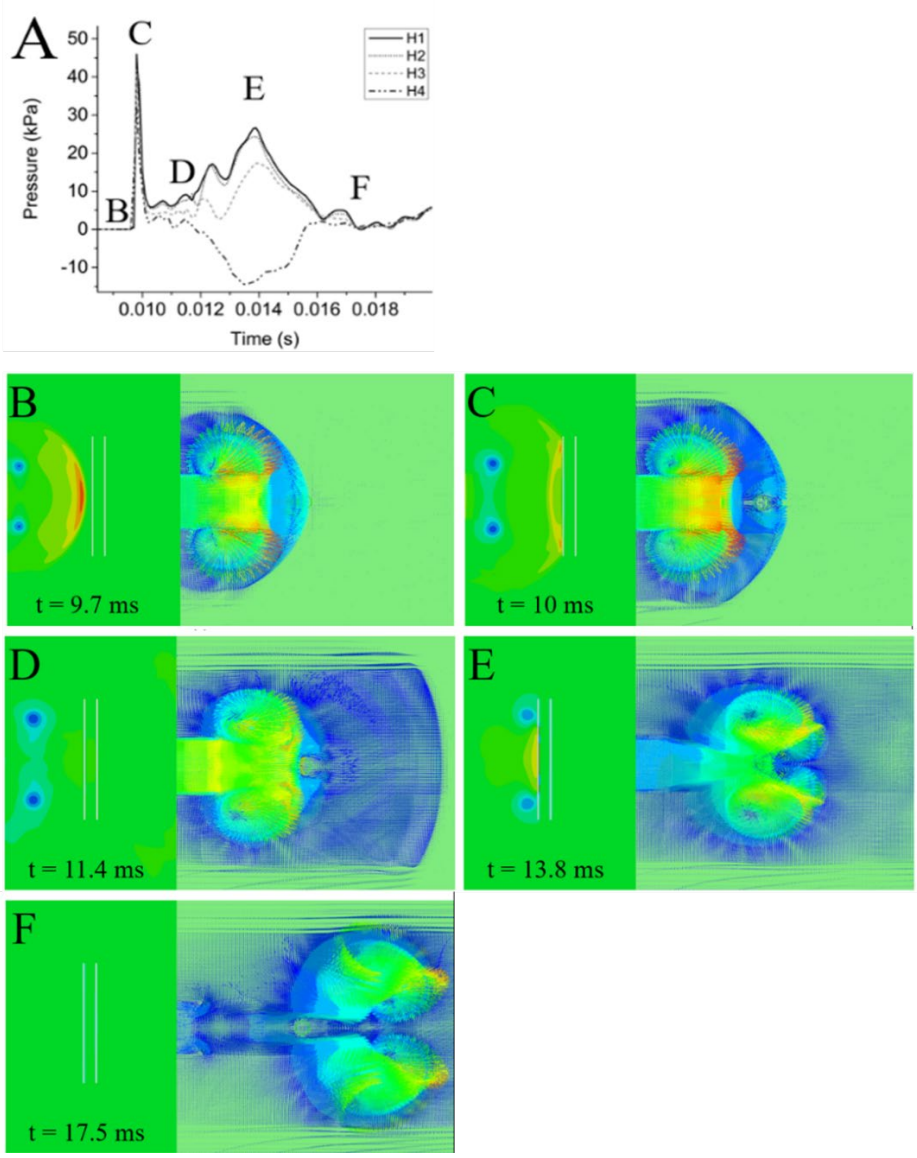

Figure 4.11. Pressure contours and velocity fields depicting how the vortex ring interacts with the cylindrical sensing apparatus. The interaction of the vortex ring at the O3 location under a moderate-intensity shock, visualized in (left) a side view of the pressure field, shown in MPa, and (right) a top-view of the velocity vectors, shown in mm/s for (1) shock front arrival, (2) peak pressure, (3) vortex ring arrival, (4) peak vortex ring interaction, and (5) complete passing of the vortex ring.

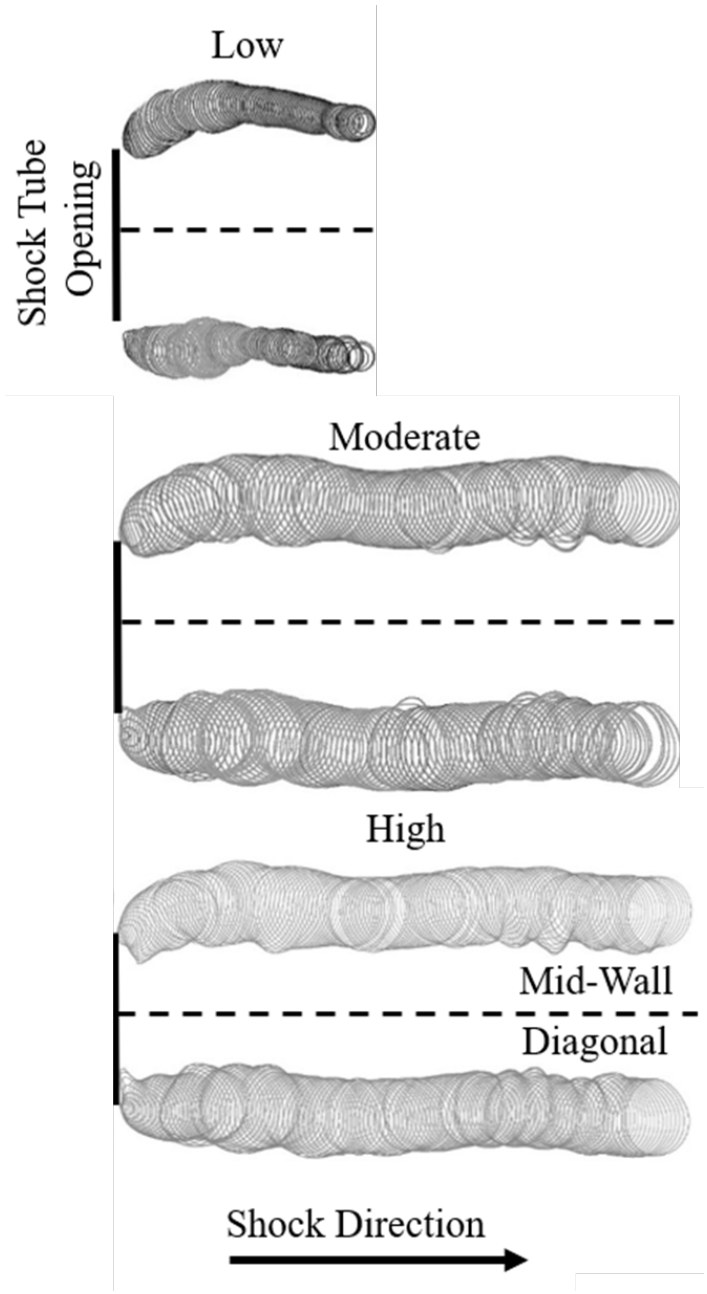

Figure 4.12. The location of the vortex ring with respect to time. Contour plots of the pressure for a cut through the middle of the shock tube wall (upper) and along the diagonal of the square (lower) display the vortex ring location with time following the expansion of the (left) low, (middle) moderate, and (right) high strength shocks.

4.3.6 Rarefaction Wave

Another flow artifact was observed following the exit of the shock wave from the confines of the shock tube. A rarefaction wave radiated upstream back into the shock tube, causing as a decrease in blast overpressure. The pressure along the longitudinal axis of the shock tube was mapped with time to capture the nature of this flow phenomenon (Figure 4.13). After the time point in which the planar shock front exits the shock tube, a fan can be observed which radiates upstream, into the shock tube. The speed of this rarefaction wave and the affected area changes with shock strength, with the rarefaction wave in the low strength shock exhibiting the largest area of influence, with a notable depression observed as deep as sensor I4. The rapid expansion of the shock front at the shock tube exit causes a density gradient to form, which initiates the rarefaction wave. Previously, we have shown that a reflection generated from a reflector plate at an appropriate offset can largely nullify the impact of the rarefaction wave on the incident waveform within the shock tube (Kuriakose et al., 2016). A normal reflection of the shock on a perpendicular endplate causes a reflected compressive wave that greatly reduces the effect of the tensile rarefaction wave. However, without an endplate, the tensile wave travels unimpeded and can affect the nature of the pressure waveform.

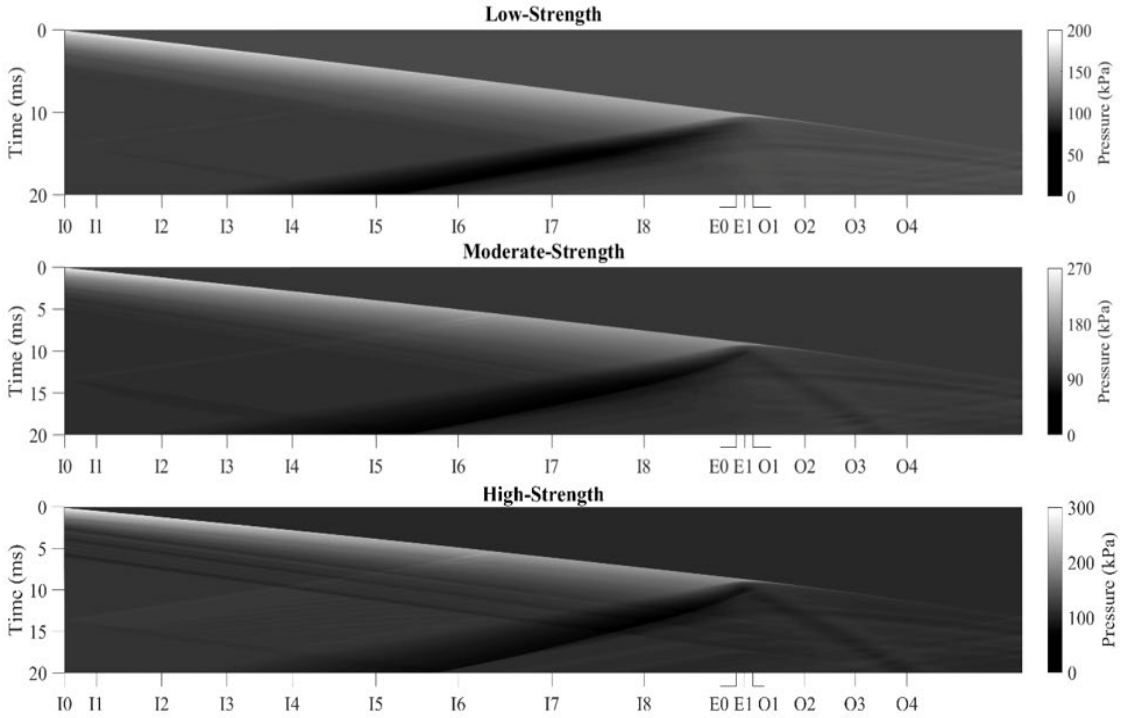

Figure 4.13. Pressure-time contour plots along the longitudinal axis. A surface map of the pressure for each node along the longitudinal axis plotted as longitudinal location vs. time, shows a rarefaction wave for the (top) low strength, (middle) moderate-strength, and (bottom) high-strength shock. The posteriorly traveling dark fan shows the region of low pressure, which is characteristic of the rarefaction wave.

4.4 Conclusions

The presented work highlights the spatial and temporal evolution of flow phenomena in the shock tube experimental setup relevant to the field of blast-induced traumatic brain injury. corroborated with pressure measurements and numerical simulations. The nature of these flow phenomena is confirmed and discussed in the range of shock strengths and shock tube dimensions commonly used to generate field-relevant shock exposures to study traumatic brain injury in animal models. In summary, while the shock front is constrained within the shock tube, the shock further exhibits strong similarities to a primary blast in the free field. The sudden expansion of the shock front into the free ambient air induces two

flow phenomena which initiate changes to the flow system. The sudden expansion causes a vortex ring formation, which develops and moves sub-sonically along the longitudinal axis, following the shock front. The vortex ring and high dynamic pressures are observed as the vorticity forms around the accelerated air within its core. Additionally, a rarefaction wave develops which propagates upstream into the shock tube, which decreases the overpressure, reducing the impulse and duration of the waveform. The shock front expands non-uniformly into the ambient air. This expanded critical shock continues to dissipate energy through expansion and experiences a reduction in peak overpressure and duration. These observations were simulated using a numerical model, validated extensively against experimental pressure measurements. This work strives to better inform the biomedical field of study by identifying the nature and extent of these flow phenomena in the common testing regime.

The limitations of this work are primarily associated with the fidelity of the numerical modeling domain. The room region outside of the shock tube exit was unobstructed by any other objects. This created an idealized flow field which does not reflect realistic experimental conditions, which would introduce reflections which cause the experiment to deviate from numerical predictions. Additionally, only a limited room domain was considered. This was shown to have a potential influence on the evolution of the critical shock, altering how planar the shock front would appear. This simplification enabled for more efficient simulations, but potentially reduced the simulation fidelity of later time points. And finally, the influence of shock tube size and cross-sectional shape were only postulated in this work. This assumption is supported by the findings of other researchers

but is not confirmed through a parametric study. Despite these limitations, we are confident in the reported trends.

These observed phenomena are essential to consider in the planning of biomedical shock tube experiments. If the experimental goal is to capture a primary shock waveform, it is recommended that the experimentalist test in locations which are not affected by the passing of the vortex ring or which experience the expansion rarefaction wave. Failure to do so would result in an alteration of the ideal primary shock characteristics. Similarly, if the goal of the experiment is to examine the interaction of an object with a vortex ring, the experimentalist is encouraged to examine the production and evolution of the vortex ring at the shock strengths investigated. The propagation speed of the vortex ring is dependent on the shock strength, and the size of the vortex ring will be dependent on the size and shape of the shock tube. Within the vortex ring, an area with pseudo-blast winds is observed, but the diameter of the vortex ring, if formed, should be compared to the experimental area to ensure that the specimen is not inadvertently experiencing pressure reductions from the vortex ring. Within the shock tube, close to the shock tube opening, regions of decreased incident pressure impulses and durations can be isolated by targeting the area of influence of the rarefaction wave. Therefore, it is recommended that experimentalists gather incident and total pressures at the experimental testing location to capture the nature of the desired flow field.

CHAPTER 5

CHARACTERIZATION OF SHOCK STRUCTURE INTERACTION BASED ON SIZE AND SHAPE OF SPECIMEN

5.1 Background

A large motivator for experimental methodologies in which the subject is placed outside of the shock tube, is that the subject is too big for the tube and is theorized to cause major deviations from field conditions due to occlusion of the shock tube (Shridharani et al., 2012). As seen in Figure 5.1, any confinement will distort the flow pattern of a steady flow, leading to changes in measured forces of lift and drag, natural boundary layer, turbulence and vortex phenomena on the object (Needham et al., 2015). This phenomenon is anticipated to be exacerbated in the shock environment and possibly in the shock tube test conditions

An empirical relationship between the dynamic pressures due to blockage, Q_b, and the dynamic pressure with no blockage, Q_o and the blockage ratio, R was derived as equations 5.1 and 5.2 (Ethridge, Lottero, Wortman, & Bertrand, 1984),

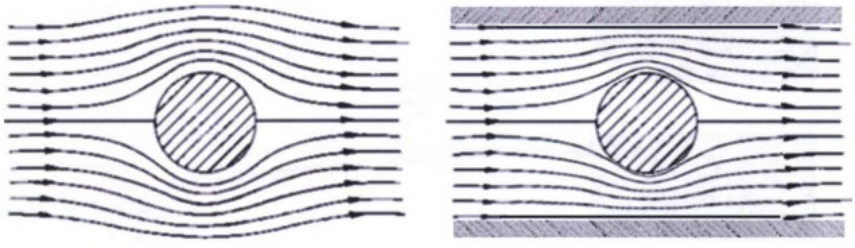

Figure 5.1. Adapted from Needham et. al. 2015; Shown in a quasi-steady flow, blockage here, should not exceed 5%, otherwise distortion is seen
Source: Ethridge, Lottero, Wortman, & Bertrand, 1984

$$R = \frac{A_{sub}}{A_{st}}. \tag{5.1}$$

$$Q_b = Q_o e^{2.64R^{1.038}}, \tag{5.2}$$

where A_{sub} and A_{st} are the cross-sectional areas of the subject and the shock tube, respectively. This relationship indicates the importance of the subject size in experimental design. As injuries will accumulate from reflections from the shock tube walls, it is hypothesized that it is especially important to minimize blockage when working with live subjects. When subjects are exposed to shock waves in the field, flow occurs in a semi-infinite medium and there is no additional flow field arising from the walls of the shock tube. As can be expected the larger the shock tube as compared to the size of the subject this reflection effect will be lesser. Additionally, as a majority of flow distortion induces high dynamic pressures, there is a potential that head accelerations from interactions with the air particles in the blast wind will cause additional brain injuries, which may not have occurred in a pure shock environment encountered in the live explosion conditions (Needham et al., 2015).

To ensure the proper loading that simulates primary blast injury, the use of simple geometry surrogates is a common practice. Simple geometries allow for a greater understanding of shock-structure interactions by eliminating many of the complexities that arise from biological structures that are typically complex in shape. In this chapter we use simple geometries, to elucidate how various parameters (specimen size and shape) affect the loading of a specimen. By examining the characteristics of reflected shock waves (peak overpressure, duration, impulse), the changes in specimen loading are examined. The computational methods are first validated using results from experimental results obtained using some simple geometries. Once validated, the computational methods are then used

to study the effects of different geometric, material and testing variables commonly encountered in tests to examine if and how they produce artifacts in the loading profiles.

5.2 Methods

5.2.1 Experimental Setup

The data generated by the experimental setup was used for the validation of the finite element model of a subject placed inside the shock tube. This experimental work was carried out by Jose Rodriquez and is presented here solely for the comparison of the experiment with the numerical simulations carried out by the author. The author does not place any claim on the experimental work per se. Once validated with the provided experimental data, the computational model has the distinct advantage of being able to be used for many other configurations commonly encountered in test paradigms used in many different laboratories.

Present experiments were conducted with the 9 x 9 inch (228.6 x 228.6 mm), 20-foot-long square cross-section shock tube (same shock tube described in Chapter 4). Tests were performed at three discrete shock wave intensities: 70, 130, and 180 kPa (10.1, 18.8, and 26.1 psi) measured at the test section of the shock tube covering a typical range in military bTBI studies. Incident pressure profiles were measured using PCB Piezotronics (Depew, NY) Model 134A24 distributed along the length of the tube. Pressure data was recorded at 1.0 MHz sampling frequency with a total acquisition time of 50 milliseconds. The pressure data signal was run through a signal conditioner prior to the DAQ, no filtering or other post processing was done to the data after data was initially collected. Variation in cross-section area, duration and specimen location was done to investigate the effects of shock loading due to the different parameters.

To investigate the effects of specimen size on shock loading, three square aluminum plates or 3D printed PLA plates with increasing cross-sectional area (H x W): 1 x 1 (1 in^2, Figure 5.2A), 2 x 2 (4 in^2, Figure 5.2B), and 3 x3 (9 in^2, Figure 5.2C) were used as test subjects. The two different materials test the effect of material properties while the three sizes study the effect of blockage in the shock tube cross-sections. Additionally, 3 x3 (9 in^2) plates with curved edges were machined to examine shock wave flow at the corner and at the walls of the shock tube. This test examined the effect of specimen location within the cross-section. The design of the plate holder was optimized to eliminate the vibration and other motion artifacts from the signal. The center of the plates was aligned with the center axis of symmetry of the shock tube to ensure flow field uniformity (except the last test). The front surface of the plate was normal to the propagation of the incident shock wave. Each plate was instrumented with pressure sensors model 102B06 (PCB Piezotronics, Depew, NY), with the sensing element placed flush with the front face placed diagonally every .85 inches (21.59 mm) as size permitted. The experimental setup is shown in figure 5.2.

5.2.2 Computational Model

A finite element model of the experimental setup with the shock tube and plate was created using coupled Eulerian-Lagrangian modeling technique, described earlier. This modeling technique has been shown to effectively simulate shock wave propagation within the shock tube and has the ability to accurately replicate the shock-structure interactions. Two modeling domains were simulated, an air-filled Eulerian domain and the other a Lagrangian domain of the solid plates. The Eulerian shock tube model simulated a 3.8 m long Eulerian domain. This domain was filled with air at atmospheric pressure and

temperature, modeled as an ideal gas with a specific heat ratio of 1.4. The length of the shock tube model was selected to simulate the section downstream from the first sensor closest to the breach, sensor A1 in Figure 5.3. The incident pressure signal from this sensor location was used as the input waveform for the simulations. The shock wave was modeled as a pressure-time waveform applied at the A1 location and was constrained at the shock tube walls and exit, where all translational degrees of freedom were constrained. The model was represented by a biased mesh, with a converged minimum element edge length of 4 mm at the region of interest, resulting in a system of over 857,000 linear hexahedral Eulerian elements.

The Lagrangian domain consisted of models of plates based on the experimental specifications. The plates were modeled with a converged element edge length of 2 mm, with the 1 in^2, 4 in^2, and 9 in^2 plates having approximately 800, 2700, and 5750 linear hexahedral Lagrangian elements, respectively. Two additional models were created to simulate the rounded edge variations of the 9 in by 2 in plates used in the corner and side shock tube locations. The plate was modeled as aluminum approximated to be linear, elastic, and isotropic with a density, elastic modulus, and Poisson's ratio of 2700 kg/m^3, 70 GPa, and 0.33 respectively. When PLA was modeled different parameters were used. Additionally, for cases examining the thickness of the plate, the material PLA (density = 1240 kg/m^3, elastic modulus = 35 GPa, and Poisson's ratio = 0.33) was also used for comparison with the Aluminum plates. The plate locations were as specified in the experimental setup for validation of the experiment and all translational and rotational degrees of freedom were constrained for a section on the posterior face of the plates, to mirror the experimental configurations.

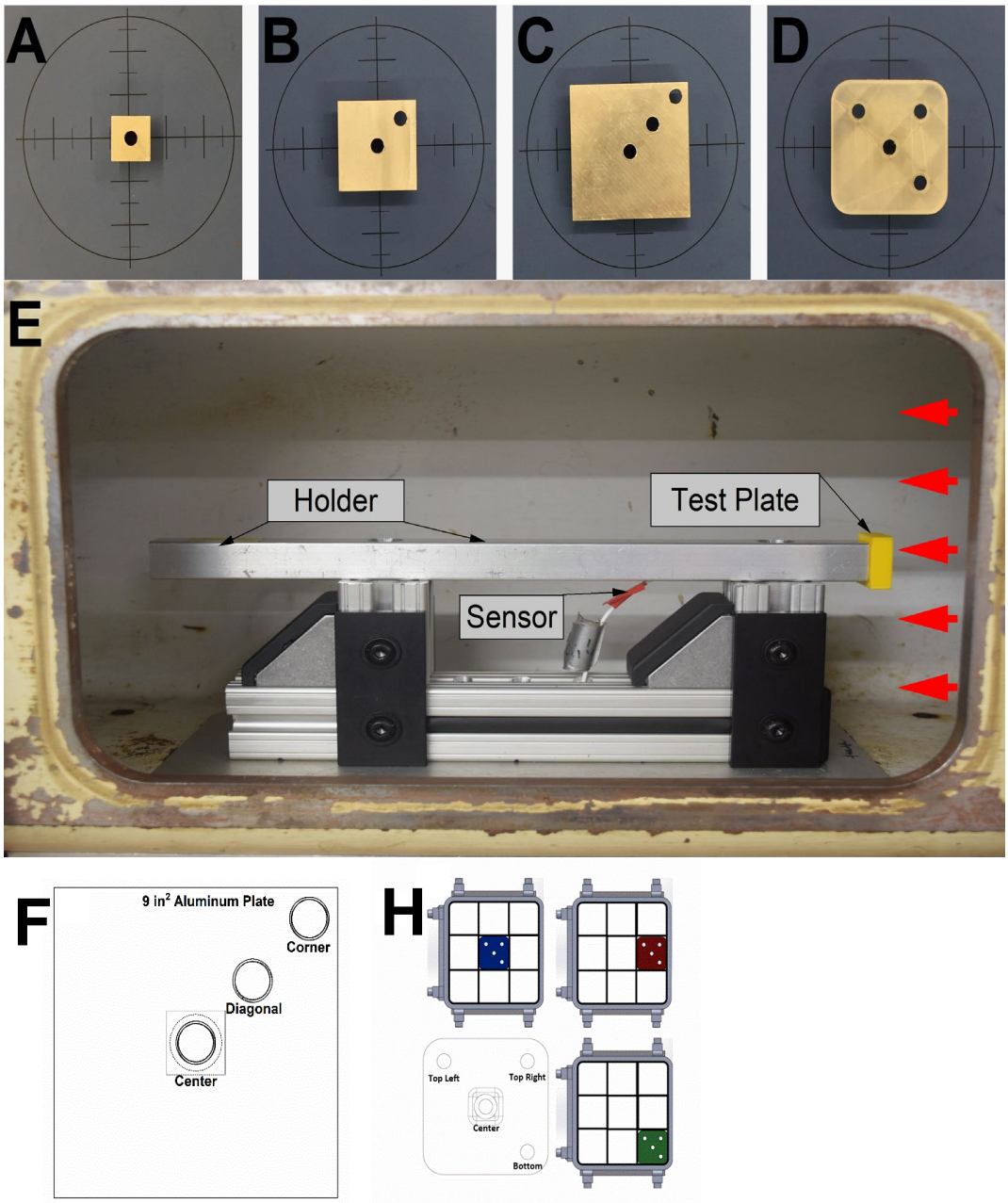

Figure 5.2. The test setup for the evaluation of the effect of the cross-sectional area on the reflected pressure. The aluminum plates with cross-sectional areas of: A) 1 in^2, B) 4 in^2, and C) 9 in^2 were mounted in the center location D) The 9 in^2 PLA plate was used in specimen location experiments E) Test fixture at the test section of the shock tube holding an instrumented 1 in^2 PLA plate (yellow). The direction of the propagation of the incoming shock wave is indicated with red arrows. F) Diagram of 9 in^2 plate showing naming conventions for each sensor location G) Diagram of the plate positioning used for evaluation of the effect of specimen location within the cross-sectional area in the test section of the shock tube.

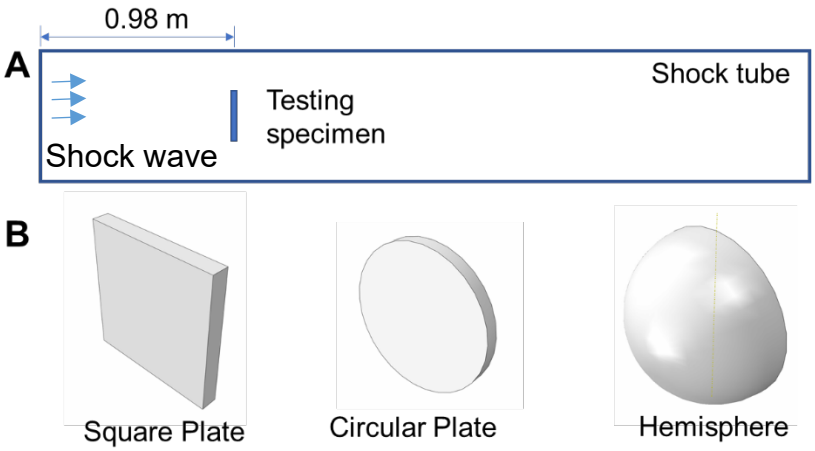

Figure 5.3. The finite element method setup showing the (A) Shock tube with the testing specimen position and (B) different testing specimens

5.3 Results and Discussion

5.3.1 Validation

Observations from the experiments were validated with the pressure-time data using a finite element model of the shock tube and the specimen. Figures 5.4-5.12 show comparison between the experiment and computational model for 1 in^2, 4 in^2, and 9 in^2 plates at the center, side, and corner locations in the shock tube. The non-linear decay and time duration for the experimental and simulated pressure profiles show excellent match, and the trends in reflected overpressure waveform evolution between different sensor locations are captured with high fidelity.

There is some discrepancy observed at the peaks. This deviation is possibly due to limitations in the experimental and computational setups. Since the shock waves consist of extremely high-pressure gradient over very small-time increments, the sensors used for data capture may have errors introduced for higher shock pressures. In the computational model, to increase the quality of the simulation, the mesh was refined, and the number of time increments was increased around the peak region. There were improvements in the fidelity around the peak region indicating that further reducing the mesh size as well as increasing the time increments would improve the result. However, the task was not undertaken due to limits in computational resources and time available for simulations. Since the peak occurs for an extremely short duration, the effect may not be significant.

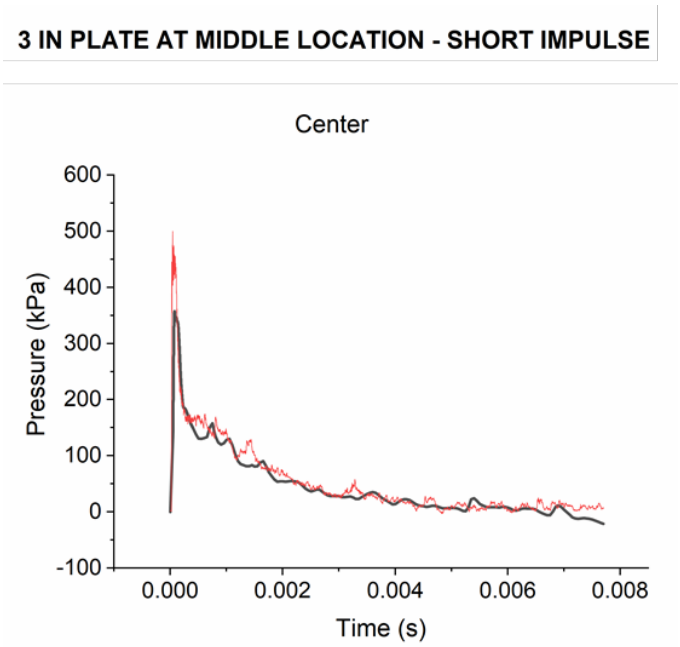

Figure 5.4. Pressure profile at the center sensor for all figures inside the diagram

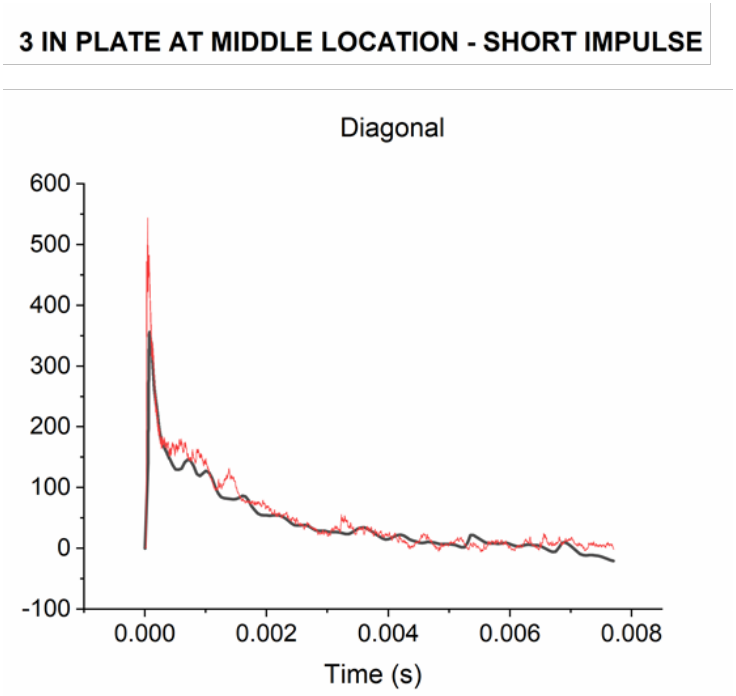

Figure 5.5. Pressure profile at the diagonal sensor

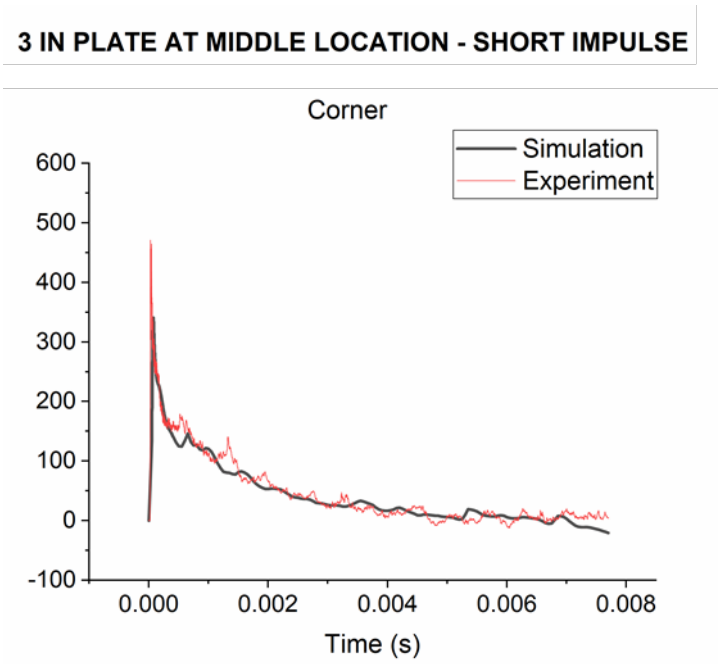

Figure 5.6. Pressure profile at the corner sensor

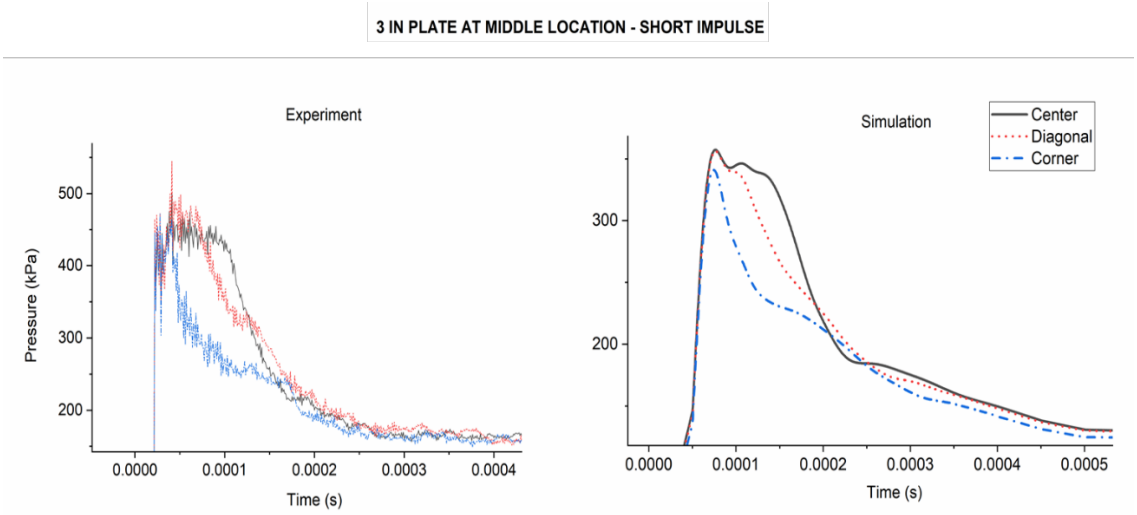

Figure 5.7. Pressure profile comparison at the peak region between Experiment and Simulation (Note the similar trends despite the difference in peak pressure)

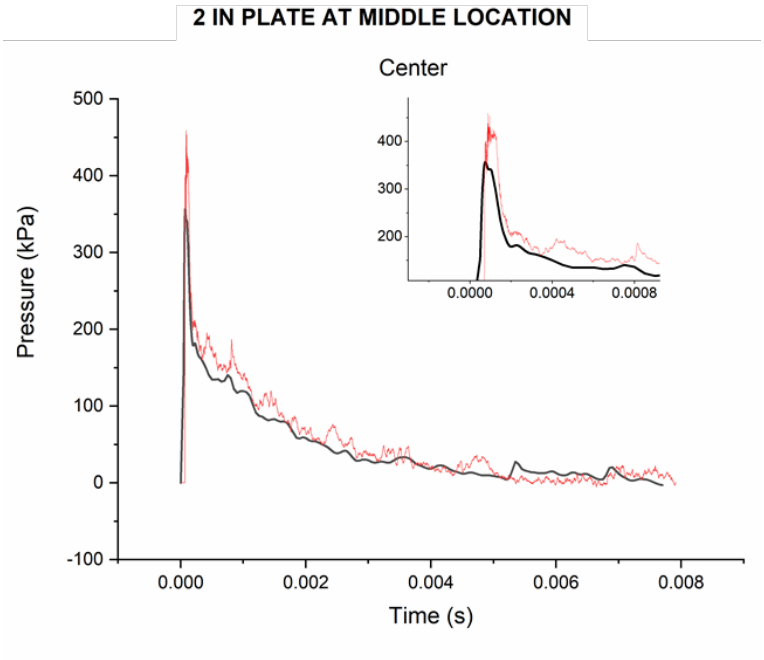

Figure 5.8. Pressure profile at center sensor for 2 in plate

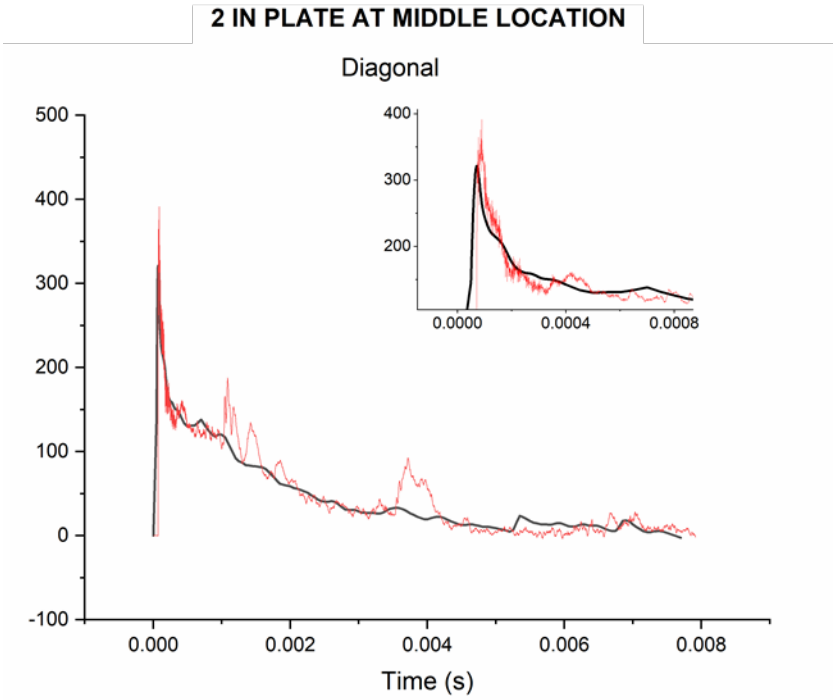

Figure 5.9. Pressure profile at diagonal sensor for 2 in plate

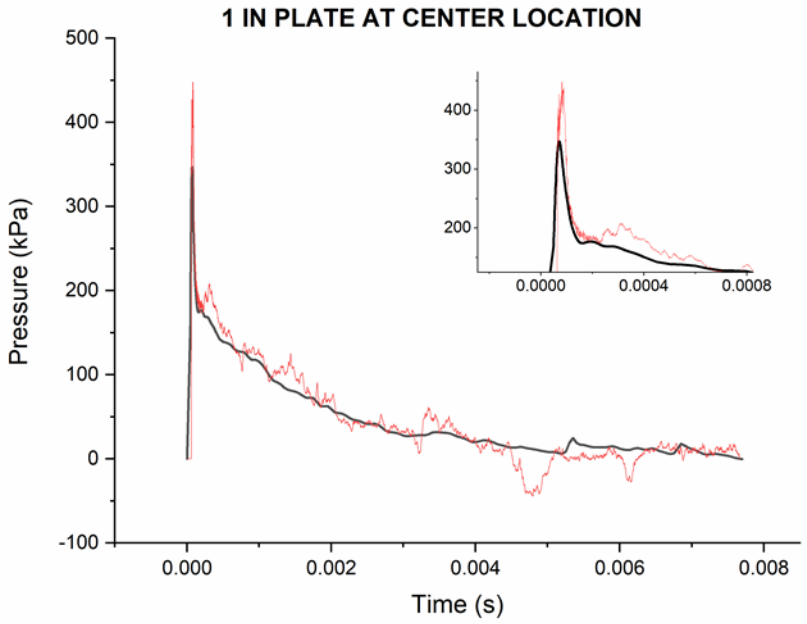

Figure 5.10. Pressure profile at center sensor for 1 in plate

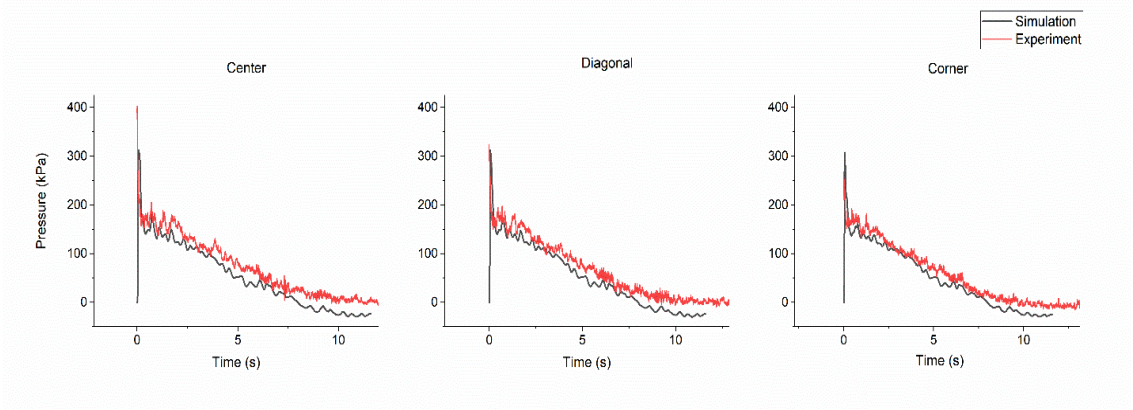

Figure 5.11. The validation of a numerical model for 3 x 3 in (9 in2) plate located at the middle

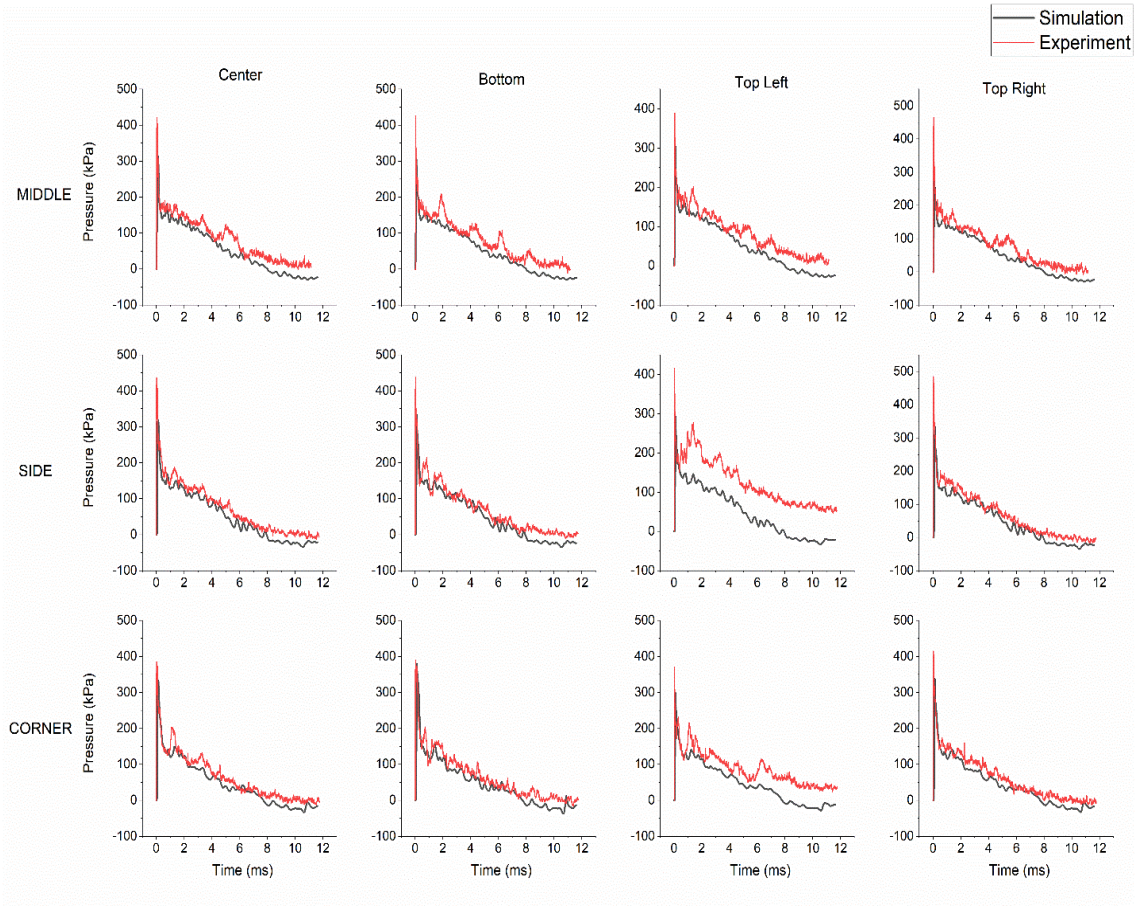

Figure 5.12. Plate validation at locations middle, side and corner locations. Since the shock tube is rounded at the corners, round plates were used for validation at various locations

5.3.2 Shock Wave – Specimen Interaction

Once the validation process was completed, variations in the shape and size of specimens were studied to examine their effect on the interactions with a shock wave inside the shock tube using the finite element model. The shock wave intensity used was 130 kPa.

It is important to understand the effects of shock tube occlusion since a majority of TBI research relies on specimen placement in shock tubes. The size of the specimen with respect to the shock tube must be well understood to avoid artifacts from occlusion. Two configurations were considered. In the first configuration, the shape of the plate was changed while maintaining the occlusion percentage. Here, circular and square plates were considered with the same cross-sectional area. For the second configuration, the surface shape was changed while keeping the same cross-sectional area and results from their impact was examined. Here, a flat circular plate was compared to a hemispherical object, with the curved edge facing the shock wave remaining the same. For both the configurations, cross-sectional areas of 11%, 25%, 40% and 75% of the total area of the shock tube were considered.

Additionally, the change in size of the specimen was examined. The size of the object was altered by changing the cross-sectional area and the thickness of the object. The cross-sectional area of a square plate was changed to occlude the shock tube by 11%, 25%, 40% and 75%.

5.3.2.1 Change in Edge Shape with Same Cross Section Area. This section examines effect due to change shape of the square plate while maintaining the occlusion percentage. Square and circular shaped plates with the same cross-sectional area were compared (Figure 5.13). The pressure profile was examined at the center of the plates.

For the same cross-sectional areas, the pressure profiles for the square and circular plates have very little difference. There was a change in the secondary peak for plates at 75% cross-sectional area, with the peak for the square plate appearing sooner than the circular plate due to the square edge being closer to the shock tube wall.

The similar shock wave interaction with the different plates can be explained by their similarities in reflection surface. Since the shock wave is perpendicular to the plate, the interaction can be considered a normal reflection. When the shock wave comes into contact with the plate, effects of the interaction at the edges can be observed at the center based on the distance from the edge and the area the shock wave needs to travel until it reaches the center. Considering that the square and circular plates of equal cross-section area for the same shock wave will have identical travel times from the edge to the center, the pressures at the centers would also be the same.

Based on the comparison between the impulse values (Figure 5.14) for the square and circular plates at different occlusion percentages, there was an average difference of 0.89% between the plates. This shows that the energy of the shock wave also remained largely the same for the different shapes.

Thus, edge shape was found to have no real effect on loading of the specimen, for the same cross section areas. After determination that there is no difference in pressure and

impulse for the circular and square plate of the same area, the circular plate was considered validated and was used for further simulations.

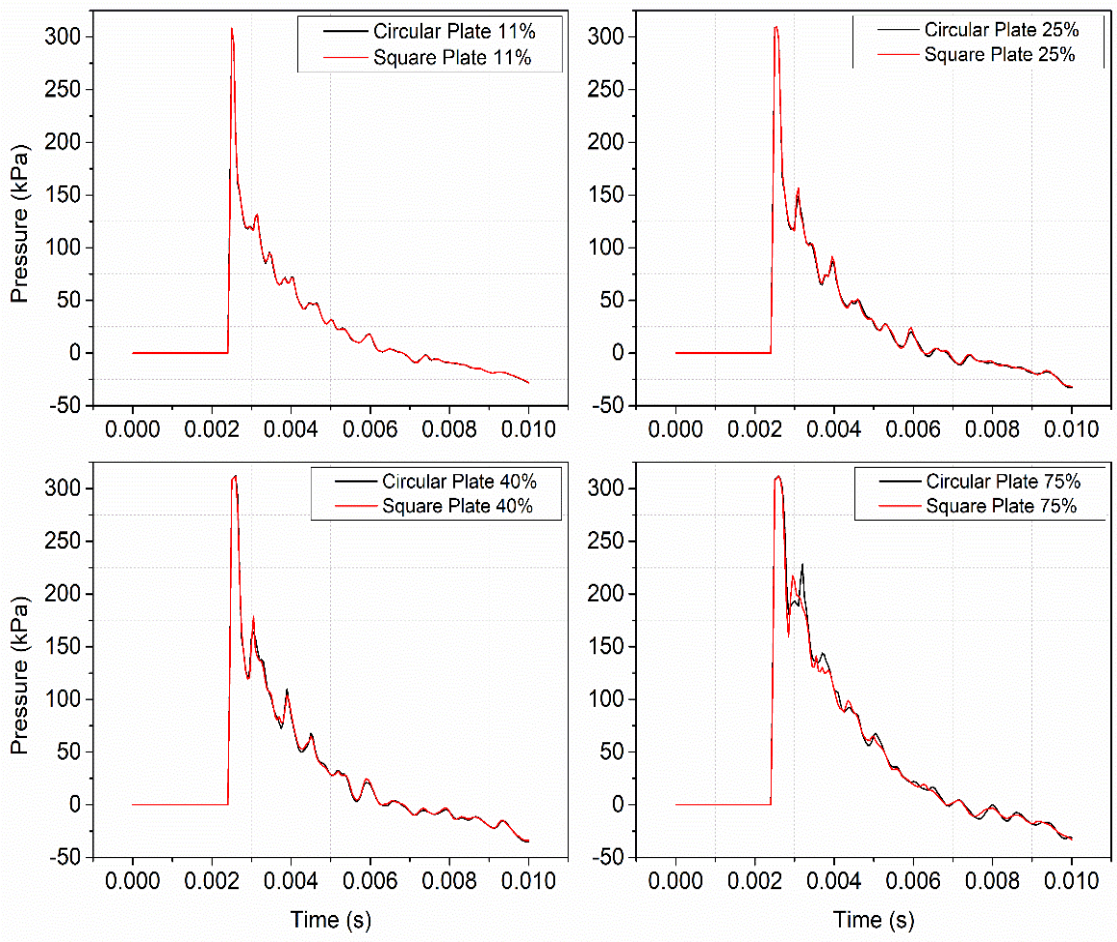

Figure 5.13. The observed effect of changing cross-sectional specimen shape with constant cross-sectional area.

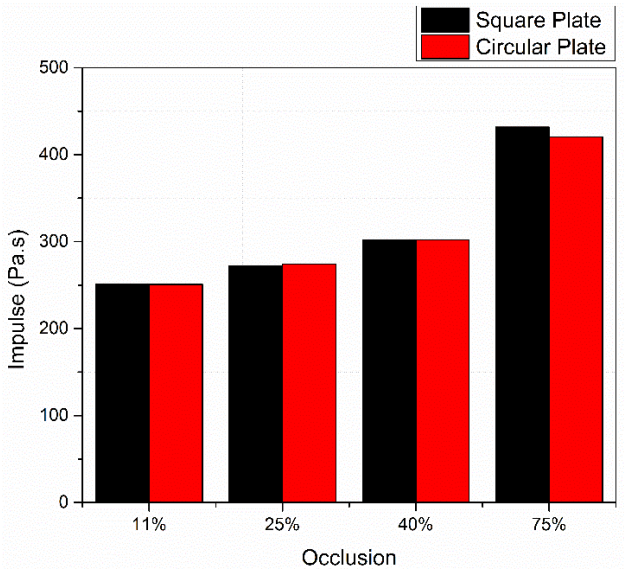

Figure 5.14. Impulse comparisons for Square and Circular Plate

5.3.2.2 Change in Thickness of Plate. The circular plate with the original thickness of 8.636 mm (0.34 in) was multiplied and effects of thicker specimen with the same cross-sectional areas was examined (Figure 5.15). Since the material used was aluminum (being incompressible), the profiles were nearly indistinguishable, having nearly identical peaks with slight changes in non-linear decay region. Similar results were obtained when the material was changed to PLA (Figure 5.16). Comparison of the pressure profiles and impulse values (Figure 5.17) between the material properties showed higher deformability for the thinnest plate. However, with increasing thickness, the difference between the plates of different materials minimized.

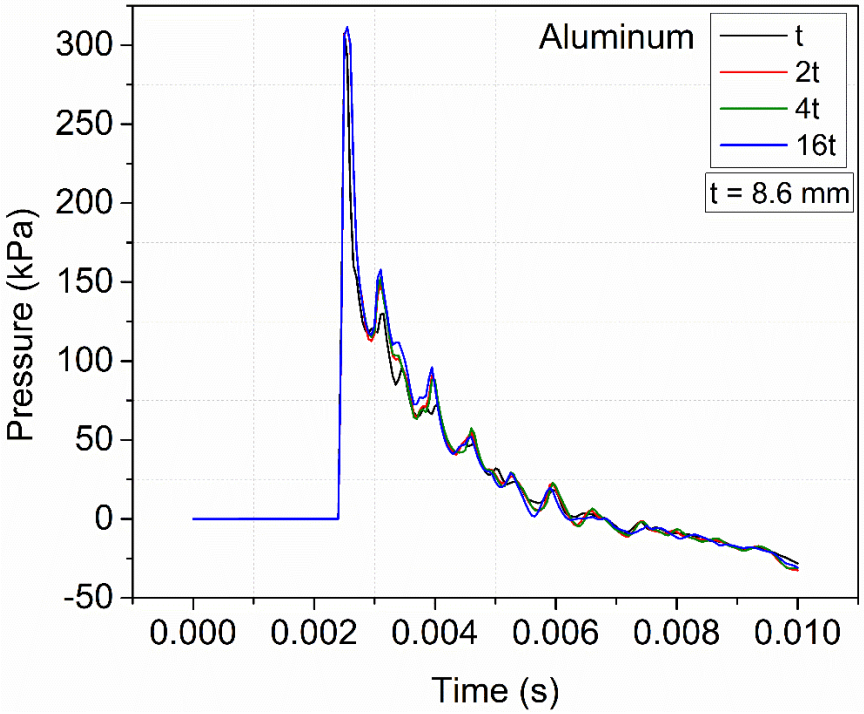

Figure 5.15. Increase in cross sectional area for the specimen, with shape remaining the same

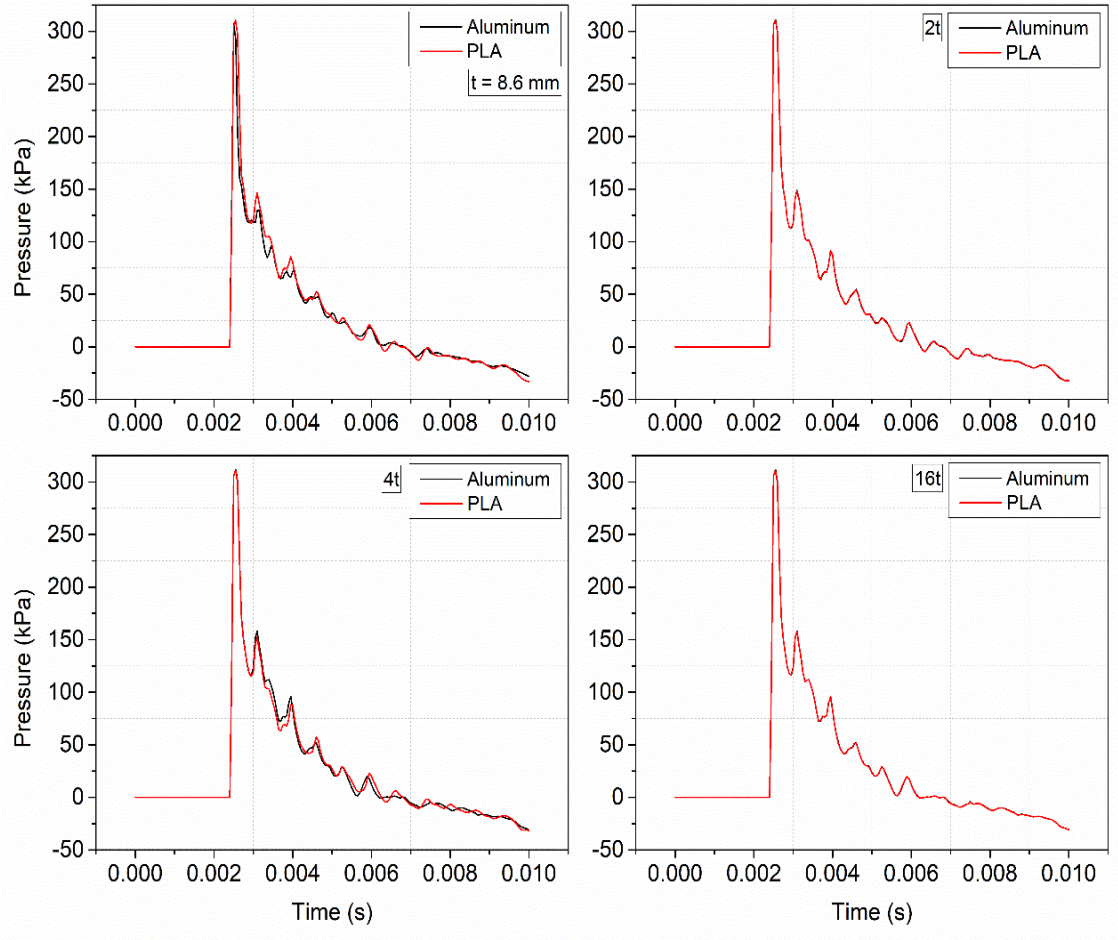

Figure 5.16. Pressure profile comparison between Aluminum and PLA plates of increasing thickness

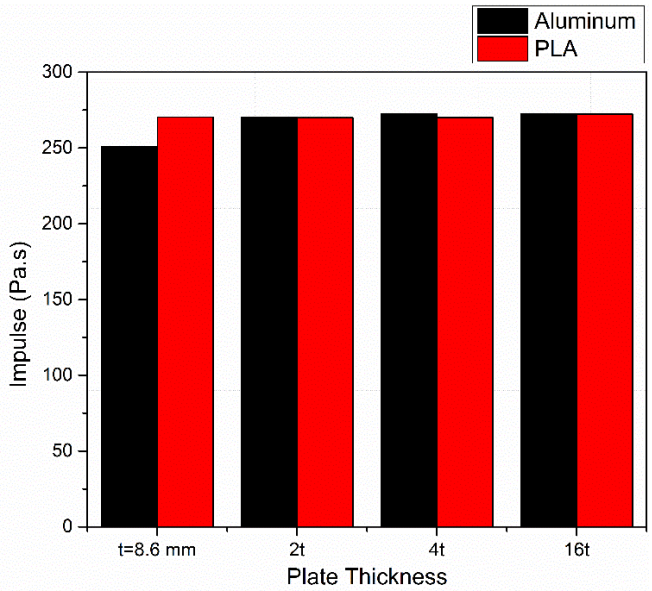

Figure 5.17. Impulse comparison between Aluminum and PLA plates of increasing thickness

Thus, the simulation did not show any difference between Aluminum and PLA. However, this result cannot be to all materials like very soft foams.

5.3.2.3 Change in Cross-Sectional Area (Circular Plate). For the circular plate, the cross-sectional area was varied to examine the effect of increasing occlusion of the shock tube (Figure 5.18). This increase in occlusion is observed to lead to an increase in impulse (Figure 5.18) and duration of the flat top region at the peak of the pressure-time profiles for the circular plates. Larger cross-sections can block more of the shock wave, resulting in an increase in dwell time (t_r) for the larger plates explaining their higher impulse values. Additionally, the increased surface area leads to higher travel times for the shock wave on the plate, from the edges to the center, leading to an increasingly larger flat top at the peak for increasing cross-section areas.

This result can also be extrapolated to assume increased loading on larger specimens inside the shock tube due to the increased occlusion.

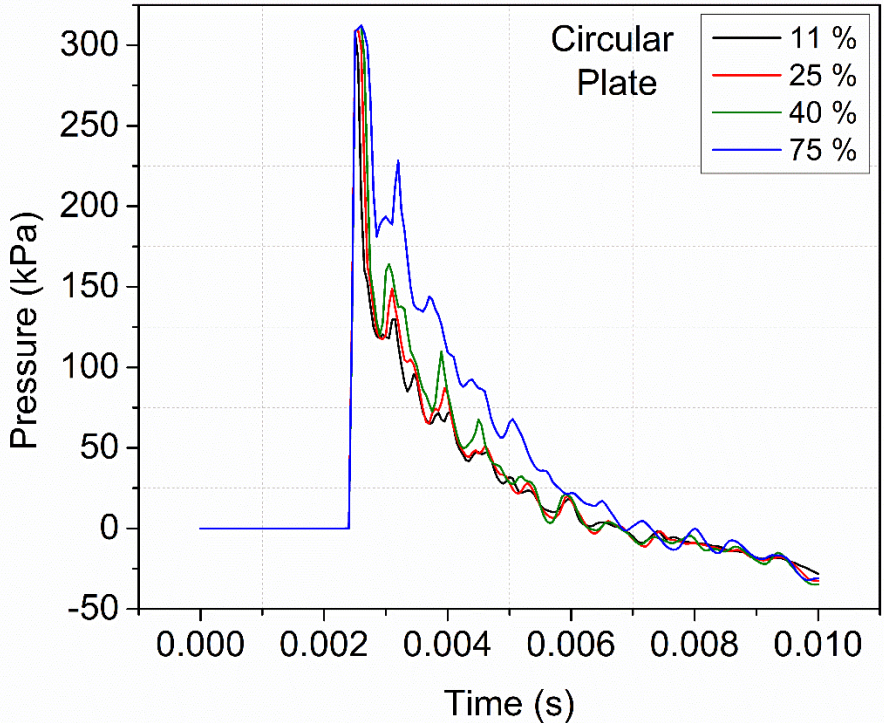

Figure 5.182. Increase in cross sectional area for the specimen, with shape remaining the same

5.3.2.4 Change in Surface Shape with Same Cross-Section Area. The circular plate was compared with a hemisphere of the same cross-section area to compare shock-structure interactions for different reflected surfaces (Figure 5.19). The curved reflected surface of the hemisphere is used to extrapolate a live specimen interaction. The main difference for the hemisphere was a reduced and sharper peak, while both subjects had similar non-linear decay regions in the pressure-time profiles. While the interaction with the circular plate can be considered a normal reflection, this is not the case for the hemisphere. The center region of the shock-hemisphere interaction can be considered

approximately normal, while the curved regions of the hemisphere would more closely resemble an oblique reflection. Additionally, the curvature of the hemisphere would affect the dwell time of the shock wave, considerable reducing it adding to the sharpness of the peak.

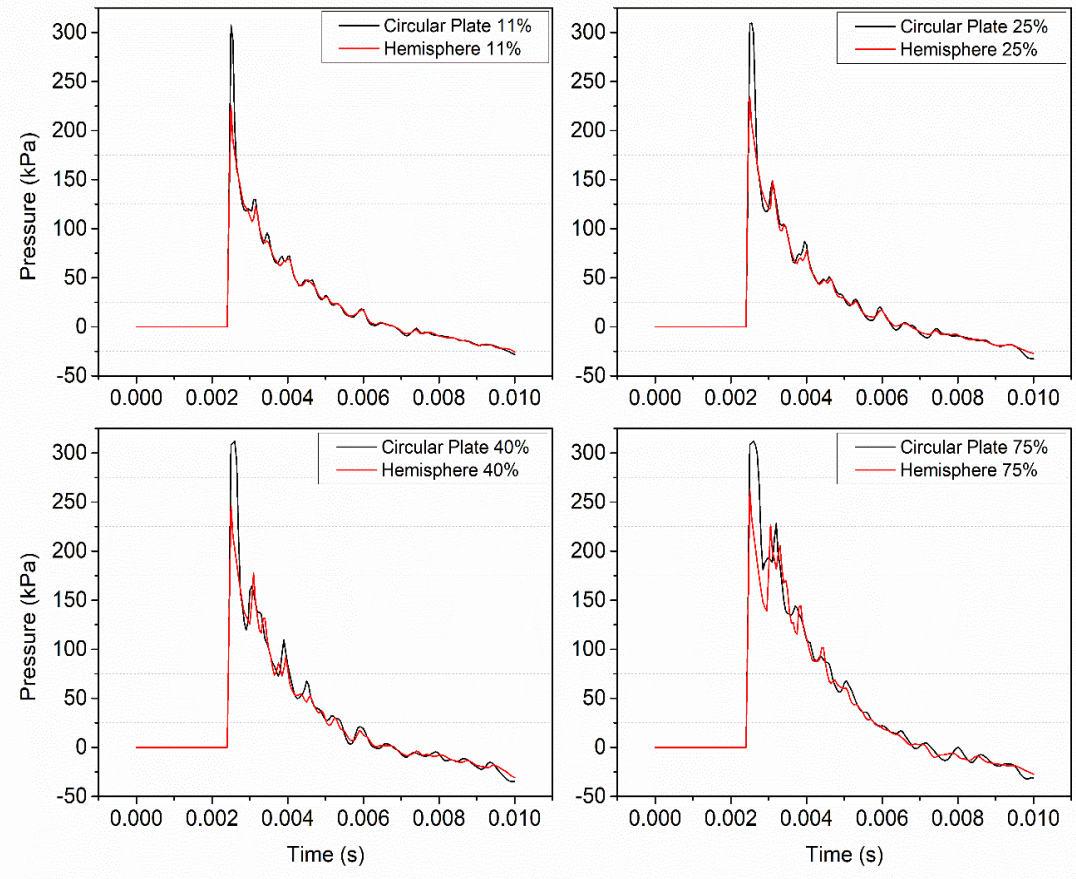

Figure 5.19. Circular plate compared with hemisphere

5.3.2.5 Change in Cross-Sectional Area (Hemisphere). The reflected pressure profiles for different hemispherical sizes were then examined. The curved reflection surface of the hemisphere leads to a sharper peak for all occlusion percentages. Additionally, the increased impulse (Figure 5.20) due to the secondary reflection is more pronounced compared to the circular plate results. This can be extrapolated to live specimen behavior, which would experience higher loading at larger occlusion percentages.

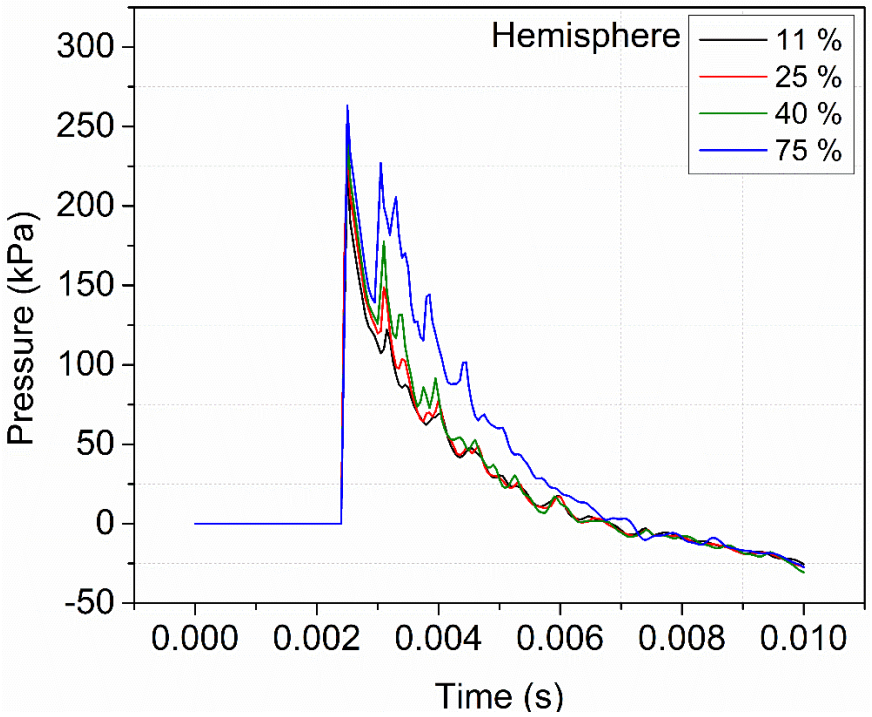

Figure 5.20. Reflected pressure profiles for different hemisphere sizes are compared.

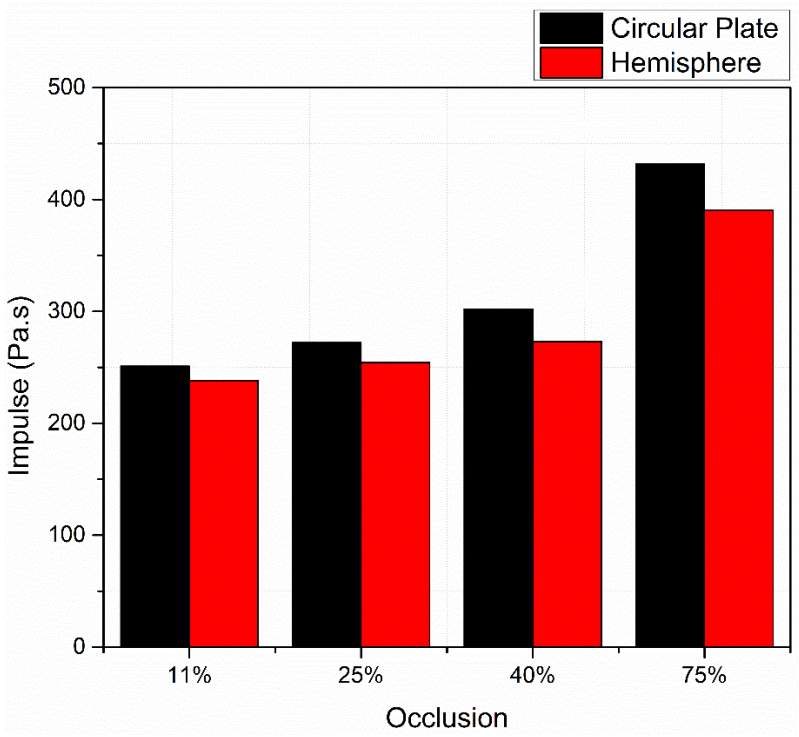

Figure 5.21. Impulse comparison for Circular plate and Hemisphere

5.3.2.6 Summary of Results. In this final chapter, we examined the effect of various specimen geometry, location within the shock tube on the fidelity of the pressure-time, impulse profile imposed on the specimen. In the last chapter, we already established to replicate faithfully the field conditions for mild bTBI, it is important not to place the specimen (especially live) near the exit or outside. In this chapter, we further analyzed even if the specimen is placed inside, what specimen and test parameters can influence the results. For this purpose, we first validated our computational simulations with experimental data (done by others) with respect to pressure-time and impulse for square plates with three different sizes. Except for the spike in the peak, the simulation matched very well with the experimental results and we concluded that the simulation is thus validated.

Once validated, we conducted additional numerical simulations to study the effect of two different shapes (square vs. circular), 2D vs 3D (circular vs. hemispherical) and different placements in the same plane from axis to corner. We can summarize the results as follows:

The study of two different shapes (square vs. circular) showed no significant changes

- When the plate thickness was varied, there was no effect on either the pressure-time or impulse
- Then we examined the effect of 2D vs 3D; For the same cross-sectional area, circular plate showed higher peak pressure as well as impulse compared to hemisphere. This can be understood from the fact that any non-normal surface allows for diffraction and thus not build the reflected pressure.
- Final study (cases 4 and 5) involved the effect of increased cross-sections. Clearly the larger sections showed increased peak pressure and impulse.

The results are summarized in the table below:

Table 5.1. Summary of Results of Chapter 5

No	Shape	Cross-section Area	Result
1	Square vs Circular Plate	No change	No change in pressure and time duration
2	Plate thickness	No change	No change in pressure and time duration
3	Circular Plate vs Hemisphere	No change	Changes observed with higher impulse at the peak region, while non-linear decay region remained similar
4	No change (circular plate)	11%, 25%, 40%, 75% of shock tube cross-section area	Impulse was higher for higher specimen cross-section areas
5	No change (hemisphere)	11%, 25%, 40%, 75% of shock tube cross-section area	Impulse was higher for higher specimen cross-section areas

CHAPTER 6

SUMMARY AND FUTURE WORK

6.1 Conclusions

Blast-induced traumatic brain injuries (bTBI) have afflicted many soldiers, veterans, law enforcement personnel and recently some civilians. To understand the effect of shock strength on the biological consequences, compressed gas driven shock tubes are extensively used in many research and federal laboratories. However, as outlined in Figure 1.1, they use different energy sources, shapes, sizes, lengths, and test subjected in a variety of locations and as each test configuration produces different wave profiles, results from different laboratories can be synergized. A validated numerical model that can predict the effect of these geometric and test variables on the quality of the wave profile can be used to compare the results as well as optimize a given set up to match the field profile. This thesis is developed to address this need.

In Chapter 3, we examined two different numerical FE models, namely pressure release and truncated models. By comparing the results with carefully designed experiments, we concluded that the truncated model shows better fidelity with the results. Though this model requires the need of a good pressure-time profile at one location, the other model suffers from the need for many other measurements including burst pressure, membrane rupture configurations and breech geometry. We concluded that the truncated model is the right approach for further studies. In Chapter 4, we demonstrated that the shock wave planarity is maintained within the shock tube length and away from exit. Though the incident peak pressure decreased, measurement of a profile close to specimen

obviates this deficiency. At or near the exit, the shock flow field becomes very complex affected by the generation of vortex rings and the production of release wave which travel both upstream and downstream. Thus, if the goal is to simulate mild bTBI, near or away from exit may not be the right location. However, other tests for shock-structure interaction can be conducted there with careful simulations. In Chapter 5, we examined the effect of material, size, shape and placement of the specimen vis-à-vis shock tube cross-section. While material and thickness have no effect, the size and location profoundly affect static and dynamic pressures and total impulse.

6.2 Contributions of This Dissertation

Blast-induced mild TBI has been called as a silent epidemic among active soldiers and veterans, and the mechanisms responsible for the injury have not been identified. Shock tube experimentation is playing a key role, but progress is impeded due to incorrect use of the equipment and experimental protocols. Inter-laboratory test data comparison is hindered by a lack of standardization procedure. This dissertation developed a numerical model, robustly validated with experimental data. Upon successful model generation, the numerical model can be used to determine the ideal test protocols for a variety of shock tubes, enabling a comparison of results generated from different shock tube experimental setups. It is hoped that the inter-laboratory comparison will propel more unified data and, hence, facilitate in the identification of injury mechanisms and offer better preventive, diagnostic and therapeutic methods.

6.3 Future Work

Since the FEM developed in this work has been validated against specially designed experiments, it is presumed that the truncated Eulerian-Lagrangian model is capable of simulating shock wave generation. Thus, any other geometry can be simulated for the purpose of identifying the evolution of the profile as well as identifying any sweet spot for testing. Though, many possible future directions exist, we outline three additional approaches:

1. Study the effect of shape of shock tube: How does circular cross-section affect the flow field compared to that of square?

2. Study the effect of specimen material: How does a very soft material like foam or skin differ from that of hard material like aluminum or bone?

3. Identify the optimal test location: Given a geometry of shock tube, which is the ideal test location to generate a given wave profile? How does the strength of the shock affect this location?

APPENDIX

APPENDIX A: Case studies in shock tube testing

Case No.	Year	Author	Study	Type	Model/Device used-BOP Intensity	BOP	Animal location /Measurement Location	Tube Length and cross section	Position	Diaphragm	Profile	Testing Location	Institution
1	2018	Alay, E	Dynamic loads on human and animal surrogates at different test locations in compressed-gas-driven shock tubes	Biomechanics	Compressed gas Shock tube	130 kPa	Inside the Shock Tube	229 mm square cross section; 711.2 mm square cross section	Headform facing the blast	Mylar	Friedlander	CIBM3, NJIT	CIBM3, NJIT
2	2018	Medhi, Biswajit	Time-resolved quantitative visualization of complex flow field emanating from an open-ended shock tube by using wavefront measuring camera	Shock wave behavior (shock tube)	Compressed gas Shock tube (piston in driver region to increase pressure)	Mach Number = 1.33	End of shock tube	Driver: 400 mm, Driven: 600 mm Inner Diameter: 31 mm	NA	Not reported	Flat top wave (using diaphragm)	Computational Mechanics Lab, Department of Civil Engineering, Indian Institute of Science, Bangalore, India	Computational Mechanics Lab, Department of Civil Engineering, Indian Institute of Science, Bangalore, India

3	2017	Sundararaj, A	Effect of blast pressure on discrete models using a shock tube	Shock wave behavior (shock tube)	Various Shapes/ Compressed gas shock tube	661-6195 kPa	End of shock tube	Driver: 2000mm, Driven: 500 mm. Radius: 40 mm	NA	Mylar	Friedlander	Karunya University	Karunya University
4	2017	Marty, A	Experimental and numerical investigations of shock wave propagation through a bifurcation	Shock wave behavior (shock tube)	Compressed gas Shock tube	Mach Number = 1.12, 1.36, 1.69	End of Shock tube (Y Bifurcation duct)	Driver: 750 mm, Driven: 299 mm, Rectangular cross section: 80 x 80 mm2	NA	Not reported	Not Reported	Aix Marseille Univ, CNRS, IUSTI, Marseille, France	Aix Marseille Univ, CNRS, IUSTI, Marseille, France
5	2016	Chan, Joel	Interactions of shock tube exhaust flows with laminar and turbulent flames	Shock wave behavior (shock tube)	Explosives Shock tube	275, 414, 517 kPa	End of shock tube	Driver: 1800 mm long, 70 mm diameter; Driven: 2200 mm long, rectangular cross section - 57 x 44 mm2	NA	Not reported	Friedlander	UNSW Australia	UNSW Australia

6	2016	Aune Vegard	A shock tube facility to generate blast loading on structures	Shock wave behavior (shock tube)	Compressed gas (air) shock tube	Various Pressure values	End of shock tube	Driver: 770 mm, Driven - 1612 mm	NA	Not reported	Flat top wave	Structural Impact Laboratory (SIMLab)	Norwegian University of Science and Technology (NTNU)
7	2016	Huber, Meabon	Validating that blast exposer causes macrophage responce	Biochemistry	Mice/Shock Tube	105.5 kPa	Inside the Shock Tube	520 mm	the animals' ventral body surface was oriented perpendicular with respect to the oncoming blast wave	Not reported	Friedlander	Boston University School of medicine	Boston University School of medicine
8	2016	Stolz, A	Analysis of the Resistance of Structural Components to Explosive Loading by Shock-Tube Tests and SDOF Models	Shock wave behavior (shock tube)	Compressed Gas shock tube	Variable pressures	Outside the Shock Tube	Variable	NA	Not reported	Not Reported	Fraunhofer Institute for High-Speed Dynamics, Eckerstraße, Germany	Fraunhofer Institute for High-Speed Dynamics, Eckerstraße, Germany

9	2016	Stemper, Shah	Looking at differences in behavior between rotaional and blast mechanisms causing mild TBI	Behavioral	Rats/ Custom Shock tube	450 kPa	Outside the Shock Tube	3000 mm driven section and 300 mm driver section	Moreover, the head was constrained laterally and inferiorly to prevent head rotational acceleration-induced injury (15), and all shock wave exposures were conducted with the sagittal plane of the rat head perpendicular to the radial axis from the Shock Tube opening.	Not reported	adjucted the angle relative to end of blast tube	Medical College of Wisconsin	Medical College of Wisconsin
10	2016	DeMar, Sharrow	Effects of Blasts on Retina and optic tract	Biochemistry	Rats/Shock Tube	137.9 kPa	Inside the Shock Tube	Shock tube length - 5334 mm	Prone transverse postion	Not reported	Friedlander	Walter Reed	Walter Reed

11	2016	Mishra, V	Primary blast causes mild, moderate, severe and lethal TBI with increasing blast overpressures: Experimental rat injury model	Biochemistry	Rats/Shock Tube	60-420 kPa	Inside the Shock Tube	229 mm inch rectangular cross section; 6000 mm driven	Prone	Not reported	Friedlander	CIBM3	NJIT
12	2015	Ostoich, C	Shock Tube Design for High Fidelity Blast Wave Simulation	Shock wave behavior (shock tube)	sphere/Shock tube	Variable pressures	Inside the Shock Tube	Driven: 152 mm; Driver: 1524 mm	NA	Not reported	Friedlander		
13	2015	Kabu, Jaffer	Examining Valscuklar Leakeage and Elavted ROS Levels due to TBI	Biochemistry	Rats/ Oxy-acetylene Shock Tube/ Table Top	137.8-896.3 kPa	Outside the Shock Tube (3cm, midline)	Variable	Prone head towards Shock Tube	Not reported	generated by different driver section configurations. For example changing the length: 18 inch driver =3.8 ms of BOP	Lerner Research Institute	Lerner Research Institute

14	2014	Courtney, E	Shock tube design for high intensity blast waves for laboratory testing of armor and combat materiel	Shock wave behavior (shock tube)	Oxygen-acetylene Shock tube (2 designs)	92,98 kPa	Outside the Shock Tube	Variable	NA	Not reported	Friedlander	BTG Research	BTG Research
15	2014	Sundaramurthy, A	A parametric approach to shape field-relevant blast wave profiles in compressed-gas-driven shock tube	Shock wave behavior (shock tube)	Compressed gas shock tube	70-350 kPa	Inside the Shock Tube	Driver: 1219 mm; Transition: 1829 mm; Driven: 6832 mm	NA	Mylar	Friedlander	University of Nebraska	University of Nebraska
16	2014	Effgen	Isolated Primary Blast Alters Neuronal Function with Minimal Cell Death in Organotypic Hippocampal Slice Cultures	Biochemistry	Cell culture wells, Helium, Nitrogen /Compressed gas shock tube	92.7-534 kPa	End of the shock tube	76 mm diameter, Variable driver length (max - 190 mm), driven section - 1240 mm	NA	Not reported	NA	Department of Biomedical Engineering, Columbia University, New York, New York	Department of Biomedical Engineering, Columbia University, New York, New York
17	2014	Gullotti, Beamer	Studying the effects of head accelerations due to blasts	Biomechanics	Rats/ Custom Shock tube/He gas driver	120-500 kPa	Outside the Shock Tube	1310 mm	Prone/ adjustable angle platform	Mylar	Not Reported	University of Pennsylvania	University of Pennsylvania

18	2014	Kamnaksh, Budde	To validate the use of DTI (Diffusion Tensor Imaging) as a way of better understaning mild TBI pathology	Biochemistry	Rats/ Shock Tube/ compressed air-driven/	~137 kPa	Not Reported	Shock tube length - 5334 mm	transverse prone position with the right side facing the direction of the membrane and the incidence of the blast waves.	Mylar	Not Reported	Walter Reed	The Uniformed Services University
19	2014	Goel, M	Interaction of a Shock Wave with a Closed Cell Aluminum Metal Foam	Shock wave behavior (shock tube)	Aluminum Foam/ Compressed gas air-driven	350 kPa	End of the shock tube	Driver: 1503 mm; Driven: 833 mm	NA	diaphragm was provided by an industrial duty air compressor	Not Reported	CSIR - Advanced Materials and Processes Research Institute (AMPRI), Council of Scientific and Industrial Research (CSIR)	CSIR - Advanced Materials and Processes Research Institute (AMPRI), Council of Scientific and Industrial Research (CSIR)

20	2014	Hua, Yi	Experimental and Numerical Investigation of the Mechanism of Blast Wave Transmission Through a Surrogate Head	Biomechanics	Surrogate Head/ Shock Tube	130 kPa	Inside the shock tube	711 mm diameter, 12319 mm length	Facing the blast	Not reported	Friedlander	University of Nebraska-Lincoln, Lincoln	University of Nebraska-Lincoln, Lincoln
21	2014	Yazici	Experimental and numerical study of foam filled corrugated core steel sandwich structures subjected to blast loading	Shock wave behavior (shock tube)	Corrugated steel structure /Compressed gas shock tube	1100 kPa	End of shock tube	Innter diameter - 38 mm	NA	Not reported	Friedlander	aUludag University, Engineering Faculty, Automotive Engineering Department, TR16059 Bursa, Turkey	aUludag University, Engineering Faculty, Automotive Engineering Department, TR16059 Bursa, Turkey

22	2014	Nguyen	Controlling blast wave generation in a shock tube for biological applications	Shock wave behavior (shock tube)	Cellular suspensions/Compressed gas shock tube	200 kPa	Inside the shock tube and End	Diameter - 59mm, 3800 mm long	NA	Mylar	Not Reported	The Royal British Legion Centre for Blast Injury Studies, Institute of Shock Physics, Imperial College London, UK	The Royal British Legion Centre for Blast Injury Studies, Institute of Shock Physics, Imperial College London, UK
23	2014	Simard	Exposure of the Thorax to a Sublethal Blast Wave Causes a Hydrodynamic Pulse That Leads to Perivenular Inflammation in the Brain	Biochemistry	Rat/Unloaded Gun/Direct Throrax Transimission	451 ± 11 kPa	Outside the Shock Tube	Various lengths	Prone	Not reported	Adjusting length of barrel	University of Maryland School of Medicine	University of Maryland School of Medicine

24	2013	Prima, Serebruany	Impact of Moderate Blast Exposures on Thrombin Biomarkers Assessed by Calibrated Automated Thrombography in Rats	Biochemistry	Rat/ Composite blast with head acceleration & Primary blast with no acceleration	230-280 kPa	Outside the Shock Tube	Ratio between driver and driven section - 1:15	Prone	Not reported	Friedlander	The Royal British Legion Centre for Blast Injury Studies, Institute of Shock Physics, Imperial College London, UK	The Royal British Legion Centre for Blast Injury Studies, Institute of Shock Physics, Imperial College London, UK
25	2013	Tümer, Svetlov	Showing the blast tbi elevate oxidative stress in the hypothalmus	Biochemistry	Rat/ Compressed air-driven Shock Tube ~2 m distance /	358 kPa	Outside the Shock Tube	Not Reported	Not Reported	0.05 mm thick stainless steel diaphrags	Not Reported	University of Florida	University of Florida

26	2013	Abdulmuneer	the hypothesis that oxidative damage of the cerebral vascular barrier interface (the blood–brain barrier, BBB) causes the development of mild traumatic brain injury (TBI) during a primary blast-wave spectrum.	Biochemistry	Rat / Primary blast/ Shock Tube/	123 kPa	Inside the Shock Tube	6096 mm	Prone	Mylar	Friedlander	University of Nebraska	University of Nebraska
27	2013	Skotak, Wan	Physiological responce to various BOP	Biomechanics	Rat/Helium driven Shock Tube	130, 190, 230, 250, 290 kPa	Inside the Shock Tube	6096 mm	Prone	Mylar	Friedlander	University of Nebraska	University of Nebraska

28	2013	Yeoh, Bell	To investigate cerebro vascular injury in Rats exposed to low-impulse pure primary blast	Biochemistry	Male Rats/ Rifle primer driven Shock Tube (Blasting Cap from .308 round was used to create blast)	145, 232, 323 kPa	Outside the Shock Tube	5580 mm	see figure 2	Adjusted by changing subjects distance and angle from the muzzle of the rifle. 1.5 cm 60 degrees for 323 kPa, 2.5 cm and 60 degrees for 232 kPa, and 5.5 cm and 30 degrees for 145 kPa	Not Reported	University of Utah	University of Utah
29	2013	Cho, Sajja	Blast effects TBI on short term memory	Biochemistry	Rat/Blast chamber (Compression wave attached to a PVC tube)/	129.23 kPa	Inside the Shock Tube	3048 mm	rostral cephalic orientation toward the shock wave	acetate sheets	Friedlander	Virginia Polytechnic Institute and State University	Virginia Polytechnic Institute and State University

30	2013	Ahmed, Kamnaksh	Indentifying Long term consequences of multiple blasts	Biochemistry	Rat / Compressed air-driven Shock Tube /	138 kPA	Outside the Shock Tube	Shock tube length - 5334 mm	transverse prone position	Not reported	Not Reported	Walter Reed	Uniformed Services University
31	2013	Arun, Abu-Taleb	Identifying the roleof compromised cell membrane integrity in TBI after blast esposure	Biochemistry	Mouse/Acompressed air-driven Shock Tube /	21 psi	Outside the Shock Tube	Shock tube length - 5334 mm	Prone	Mylar	Not Reported	Walter Reed	Walter Reed
32	2013	Valiyavettil, Alamneh	Modulation of cholinergic pathways and inflammatory mediators in blast-induced traumatic brain injury	Biochemistry	Mouse/ blast overpressure/	20.6 psi	Outside the Shock Tube	Shock tube length - 5334 mm	Prone	Mylar	Not Reported	Walter Reed	Walter Reed

33	2013	Turner, Naser	Modeling clinically relevant blast parameters based on scaling principles produces functional & histological deficits in rats	Biomechanics	Rats/Tabletop Shock Tube/	31, 50, 72, 90 psi	Outside the Shock Tube	170.2 mm diameter	Prone with right side facing blast	clear polyester membranes (Rid out Plastics Co.) of varying thickness (0.003″–0.010″) to achieve a range of peak over pressure exposures.	Not Reported	West Virginia School of Medicine	West Virginia School of Medicine
34	2013	Selvan	Blast Wave Loading Pathways in Heterogeneous Materiai Systems- Experimentai and Numericai Approaches	Biomechanics	Cylinder / Surrogate Head/Shock Tube/	150 kPa	Inside the Shock Tube	Shock tube length - 12192 mm	Not Applicable	Mylar	Not Reported	University of Nebraska	University of Nebraska

35	2013	Tumer, N	Overpressure blast-wave induced brain injury elevates oxidative stress in the hypothalamus and catecholamine biosynthesis in the rat adrenal medulla	Biochemistry	Compressed Air driven Shock tube	358 kPa	Outside the Shock Tube (2m from exit)	Ratio between driver and driven section - 1:15	Facing the blast	stainless steel diaphragm	Not Reported	Department of Veterans Affairs Medical Center, Gainesville, FL	Department of Veterans Affairs Medical Center, Gainesville, FL
36	2013	Genovese, RF	Effects of mild TBI from repeated blast overpressure on the expression and extinction of conditioned fear in rats	Biochemistry	Compressed Air driven Shock tube	74.5 kPa	Inside the Shock Tube	304.8 mm diameter, 5334 mm long (762 mm driver, 4572 mm driven)	Facing the blast	Mylar	Not Reported	Center for Military Psychiatry and Neurosciences, Walter Reed Army Institute of Research, Silver Spring, MD, USA	Center for Military Psychiatry and Neurosciences, Walter Reed Army Institute of Research, Silver Spring, MD, USA
37	2013	Harington, B	The study of a human head simulant's dynamic response to a blast wave	Biomechanics	Explosive Shock tube	Various Pressure values	Outside the Shock Tube	563 mm Diameter; 500 mm long driven; 4000 mm long driver	Facing the blast	Not reported	NA	Impact and Armour Group, Centre for Defence Engineering	Cranfield University

38	2012	Shridharani, Wood	Determining the dynamic repsonce of the brain at varios BOP	Biomechanics	Pigs/Compressed-gas Shock Tube/variable	107-740 kPa	Outside the Shock Tube	Not Reported	Prone	Varied Diaphram thickness and driver length	Not Reported	Duke University	Duke University
39	2012	Sundaramurthy, Alai	Blast-Induced Biomechanical Loading of the Rat: An Experimental and Anatomically Accurate Computational Blast Injury Model	Biomechanics	Rat/compressed gas Shock tube/	100, 150, 200, 225 kPa	Inside the Shock Tube	Shock tube length - 6096 mm	Prone	Not reported	Not Reported	University of Nebraska	University of Nebraska
40	2012	Ahlers, Vasserman-Stoke	investigating affects of acute repeated exposure on TBI	Biochemistry	Rat/Pneumatically driven Shock Tube	36.6, 74.5, 116.7 kPA	Inside the Shock Tube	Shock tube length - 5334 mm	Prone/ facing or side ways	Adjusting number of Mylar sheets	Not Reported	Walter Reed	Naval Medical Research Center
41	2012	Balakathiresan, Bhomia	Micro RNA Let-7i Is a Promising Serum Biomarker for Blast-Induced Traumatic Brain Injury	Biochemistry	Rat/ Air-driven Shock Tube	120 kPa	Outside the Shock Tube	Shock tube length - 5334 mm	right side ipsilateral to the direction of the BOP	Mylar	Mylar Membranes	Walter Reed	Uniformed Services University

42	2012	Kovesdi, Kamnaksh	Testing how well acute minocycline treats mild TBI	Biochemistry	Rat/ Shock tube/	20.6 psi	Inside the Shock Tube	Shock tube length - 5334 mm	Transverse prone position		Not reported	Walter Reed	Uniformed Services University
43	2012	Elder, Dorr	Blast Exposure Induces Post-Traumatic Stress Disorder-Related Traits in a Rat Model of Mild Traumatic Brain Injury	Biochemistry	Rat/Air blast Shock Tube	74.5 kPa	Outside the Shock Tube	Shock tube length - 5334 mm	head facing the blast exposure without any body shielding,	Mylar	Not Reported	Walter Reed	Department of Veterans Affairs Medical Center,
44	2012	Houas	The effects that changes in the diaphragm aperture have on the resulting shock tube flow	Shock wave behavior (shock tube)	Compressed gas Shock tube	Mach number - 1.06 to 1.25	NA	Driver: 750 mm, Driven: 299 mm, Rectangular cross section: 80 x 80 mm2	NA	Aluminum	Not Reported	Aix Marseille Univ, CNRS, IUSTI, Marseille, France	Aix Marseille Univ, CNRS, IUSTI, Marseille, France

45	2012	Dalle Lucca, Chavko	Blast-induced moderate neurotrauma (BINT) elicits early complement activation and tumor necrosis factor alpha (TNFα) release in a rat brain	Biochemistry	Rat/ Compressed air-driven Shock Tube ~2 m distance /	120 kPa	Not Reported	Shock tube length - 5334 mm	resulting in a full body exposure to the blast wave	Mylar	Not Reported	Walter Reed	US Army Institute of Surgical Research
46	2012	Bir, VandeVord	Effects of variable blast pressures on blood flow and oxygen saturation in rat brain as evidenced using MRI	Biochemistry	Rat/Gas-driven Shock Tube	90, 103, 117, 159, 193 kPa	Inside the Shock Tube	Shock tube length - 6096 mm	Prone	Mylar	Not Reported	Wayne State University	Wayne State University

47	2012	Zhu, Skelton	Biochanical reponse due to blast loading	Biomechanics	Pigs/ ORA Inc. Shock tube/detonation of explosive chrage	100-250 kPa	Inside the Shock Tube	2070 mm, 2438.4 mm heavy walled driver chanber, 3048 mm expansion section, 1524 mm test section.	Perpendicular to the long axis of the tube	Not reported	Not Reported	Wayne State University	Wayne State University
48	2012	Goeller, Wardlaw	Investigation of Cavitation as a Possible Damage Mechanism in Blast-Induced Traumatic Brain Injury	Biomechanics	Head Surrogate/ Shock tube/	69-170 kPa	Outside the Shock Tube	2336.8 mm	Not Applicable	Not reported	Not Reported	Advanced Technology and Research Corporation	Advanced Technology and Research Corporation
49	2012	Courtney, Lubov	Oxy-acetylene driven laboratory scale shock tubes for studying blast wave effects	Biomechanics	Various Materials/Oxygen acetylene based shock tube	204 - 1187 kPa	End of the shock tube	Driven section : 60 diameters	NA	Latex balloons	Friedlanderesque	R & D, Force Protection Industries, Inc	R & D, Force Protection Industries, Inc

50	2012	Chandra, Namas	Evolution of blast wave profiles in simulated air blasts: experiment and computational modeling	Shock wave behavior (shock tube)	Compressed gas shock tube	150-250 kPa	Inside the shock tube	229 mm square cross section, 6225 mm length	NA	Friedlander	Friedlander	University of Nebraska	University of Nebraska
51	2012	Ganpule	Mechanics of blast loading on the head models in the study of traumatic brain injury using experimental and computational approaches	Biomechanics	Surrogate Head/ Shock Tube	100 kPa	Inside the Shock Tube	Shock tube length - 12192 mm	Not Applicable	Mylar	Friedlander	University of Nebraska	University of Nebraska
52	2011	Rafaels, Cameron	Survival Risk Assessment for Primary Blast Exposures to the Head	Biomechanics	White Rabbits/ 8 in Diameter Shock tube	168.5 kPa-1086 kpa	Outside the Shock Tube	1206 mm	Not Reported	Mylar	Friedlander	Duke Univeristy	University of Virginia
53	2011	Reneer, Hisel	A Multi-Mode Shock Tube for Investigation of Blast-Induced Traumatic Brain Injury	Biomechanics	compressed air/helium driven tube mode, or oxyhydrogen – RDX explosives mode	100, 150, 200 kPa	Inside the Shock Tube	Shock tube length - 6553.2 mm	laterally with the left side facing the blast	Not reported	Friedlander	Univeristy of Kentucky	Univeristy of Kentucky

54	2011	Zuckerman, Amitai	Controlled Low-Pressure Blast-Wave Exposure Causes Distinct Behavioral and Morphological Responses Modelling Mild Traumatic Brain Injury, Post-Traumatic Stress Disorder, and Comorbid Mild Traumatic Brain Injury –Post-Traumatic Stress Disorder	Biomechanics/Behavioral	Exploding wire technique	100-350 kPa	265 mm from exploding wire	NA	Prone	NA	NA	Ben-Gurion University of the Negev	Ben-Gurion University of the Negev
55	2011	Arun, Spadaro	Studies on blast traumatic brain injury using in-vitro model with shock tube	Biochemistry	Compressed air-driven Shock Tube / Cell Cultures	94.3, 124.3, 145 kPa	Inside the Shock Tube	Shock tube length - 5334 mm	N/A	Mylar	Mylar Membranes	Walter Reed	Walter Reed

56	2011	Cernak, Merkle	we describe the pathophysiological consequences of graded blast injuries and BINT generated by a newly developed, highly controlled, and reproducible model using a modular, multi-chamber shock tube capable of tailoring pressure wave signatures and reproducing complex shock wave signatures seen in theater.	Biochemistry	Mouse/Helium modular, multi-chamber Shock Tube/mild	183, 213, 295 kPa	Inside the Shock Tube	Shock tube length - 5882.64 mm	Prone or Supine	various combinations of Kapton and polyethylene sheets.	Not Reported	Johns Hopkins	Johns Hopkins

57	2011	Koliatsos, Cernak	A Mouse Model of Blast Injury to Brain: Initial Pathological, Neuropathological, and Behavioral Characterization	Biochemistry/Behavioral	Mouse/ Helium multi chamber Shock Tube	25-45, 26.5 psi	Inside the Shock Tube	Shock tube length - 5882.64 mm	frontally or dorsally positioned against the open end of the shock tube, that is, toward the shock front.	various combinations of Kapton and polyethylene sheets.	Not Reported	Johns Hopkins	Johns Hopkins
58	2011	Risling, Plantman	Mechanisms of blast induced brain injuries, experimental studies in rats	Biochemistry	Rat/blast tube with pressure wave/	130, 260 kPa	Inside the Shock Tube	1500 mm	Prone/Side exporsure	Not reported	Not Reported	Karolinska Institutet	Karolinska Institutet
59	2011	Garman, Jenkins	Blast Exposure in Rats with Body Shielding Is Characterized Primarily by Diffuse Axonal Injury	Biochemistry	Rat/Helium-driven Shock Tube/	241.3 kPa	Inside the Shock Tube	Shock tube length - 6400.8 mm	Not Reported	Mylar	Not Reported	University of Pittsburgh School of Medicine	University of Pittsburgh School of Medicine

60	2011	Gyorgy, Ling	Time-Dependent Changes in Serum Biomarker Levels after Blast Traumatic Brain Injury	Biochemistry	Pig/ compression-driven Shock Tube	(165–255 kPa, average 194.4 kPa; N = 9) or moderate (275–358 kPa, average 321.3 kPa; N = 16)	Not Reported	Not Reported	Not Reported	Not	Not Reported	Walter Reed	Uniformed Servises University
61	2011	Larcher, M	Experimental and numerical investigations of laminated glass subjected to blast loading	Shock wave behavior (shock tube)	Laminated glass/ Shock tube	Variable pressures	Not Reported	Not Reported	Not Reported	Not	Not Reported	University of the Armed Forces Munich	University of the Armed Forces Munich
62	2011	Ganpule, S	Role of helmet in the mechanics of shock wave propagation under blast loading conditions	Biomechanics	Head Surrogate/ Shock tube	200 kPa	Inside the Shock Tube	Driver: 1530 mm; Driven: 833 mm	Facing the blast	Friedlander	Friedlander	University of Nebraska	University of Nebraska

63	2011	Vandevord	Mild Neurotrauma Indicates a Range-Specific Pressure Response to Low Level Shock Wave Exposure	Biomechanics, behavioral	Rat/Helium driven Shock Tube	0, 97, 117 and 153 kPa	Inside the Shock Tube (44 in from exit)	Diameter - 304.8 mm, Driver - 762 mm, Driven - 6146.8 mm	Facing the blast	Mylar	Friedlander	Wayne State University	Wayne State University
64	2011	Kuehn	Rodent Model of Direct Cranial Blast Injury	Biochemistry	Rat/Unloaded Gun/Direct Head transmission	250-1000 kPA	Outside the Shock Tube	Various lengths	Prone	Adjusting	Not Reported	University of Maryland School of Medicine	Walter Reed
65	2010	Leonardi	Intracranial Pressure Increases during Exposure to a Shock Wave	Biomechanics	Rat/Helium driven Shock Tube	70 kPa	Inside the Shock Tube (44 in from exit)	Diameter - 304.8 mm, Driver - 762 mm, Driven - 6146.8 mm		Not Reported	Not Reported		
66	2010	Svetlov	Morphologic and biochemical characterization of brain injury in a model of controlled blast overpressure exposure	Biochemistry	Rat explosed to 358 kPa for 10 sec	358 kPa	Inside the shock tube	Ratio between driver and driven section - 1:15	Prone	Mylar	Friedlander	Florida Institute of Technology and Banyan Biomarkers, Inc.	Florida Institute of Technology

67	2010	Chavko, Watanabe	Relationship between orientation to a blast and pressure wave propagation inside the rat brain	Biomechanics	Rat/ Air-driven Shock Tube/	36 kPa	Inside the Shock Tube	Not Reported	(1) frontal, a head-on orientation with the head facing blast; (2) side-on orientation, with the right side exposed to blast; and (3) in a backward position to blast with the head facing away from blast	Not reported	Not Reported	Naval Medical Research Center,	Naval Medical Research Center,
68	2010	Cernak, Merkle	The pathobiology of blast injuries and blast-induced neurotrauma as identified using a new experimental model of injury in mice	Biochemistry	Multi chamber shock tube (helium)	183, 213, 295 kPa	Inside the Shock Tube (Near end)	Driver - 940 mm, Driven - 4950 mm, Diameter - 146 mm	Supine vs Prone	Friedlander	Friedlander	Johns Hopkins University Applied Physics Laboratory	Johns Hopkins University Applied Physics Laboratory

69	2010	Readnower, Chavko	Increase in blood–brain barrier permeability, oxidative stress, and activated microglia in a rat model of blast-induced traumatic brain injury†	Biochemistry	Rat/Air-driven Shock Tube	120 kPa	Outside the Shock Tube	Shock tube length - 5334 mm	right side ipsilateral to the direction of the BOP.	Not	Not Reported	Univeristy of Kentucky	Univeristy of Kentucky
70	2009	Saljo, Bolouri	Intracranial pressure (ICP). Cognitive functions (Morris water maze).	Behavioral	Rat/ Shock tube	10, 30, 60 kPa	Inside the Shock Tube	Shock tube length: 3100 mm	Prone facing the blast	Cell aphane membrane	Cellaphane membrane	University of Göteborg	University of Göteborg
71	2008	Saijo	Neuropathology and pressure in the pig brain resulting from low-impulse noise exposure	Biomechanics	Rat/Air-driven Shock Tube	8.7 kPa	Outside the shock tube	200 mm diameter, 1600 mm driver, 1500 mm driven	Various positions	Not reported	Not reported	University of Göteborg	University of Göteborg
72	2009	Long, Bentley	Blast Overpressure in Rats: Recreating a Battlefield Injury in the Laboratory	Biomechanics	Rat/compression-driven Shock Tube/	126, 147, kPa	Outside the Shock Tube	Shock tube length - 5334 mm	Prone transverse position	Mylar	Friedlander	Walter Reed	Walter Reed

73	2009	Alley, Schimizze	Experimental modeling of explosive blast-related traumatic brain injuries	Biomechanics	Explosives Shock tube	82-455 kPa	Outside the Shock Tube	Variable lengths	NA	NA	Not reported	Purdue University	Purdue University
74	2009	Bauman	An Introductory Characterization of a Combat-Casualty-Care Relevant Swine Model of Closed Head Injury Resulting from Exposure to Explosive Blast	Biomechanics	Swine/ Shock Tube	234.4 kPa	Inside the Shock Tube	Shock tube length: 21336 mm	Prone	Not reported	Not reported	Walter Reed	Walter Reed
75	2001	Cernak, Wang	To determine the memory deficit due to damage in hippocampus. Nitric Oxide Production, Electron microscopy study	Biochemistry	Rat/large-scale BT-I Shock Tube/ Small scale BT-111 Shock tube	338.9 ± 9.1 kPa 440 kPa	Not Reported	Not Reported	Not Reported	Not reported	Not Reported	Johns Hopkins	Johns Hopkins

REFERENCES

Abate, G., & Shyy, W. (2002). Dynamic structure of confined shocks undergoing sudden expansion. *Progress in Aerospace Sciences, 38*, 23-42. doi:https://doi.org/10.1016/S0376-0421(01)00016-1

Abe, A., & Takayama, K. (1990). Numerical simulation and density measurement of a shock wave discharged from the open end of a shock tube. *JSME international journal. Ser. 2, Fluids engineering, heat transfer, power, combustion, thermophysical properties, 33*(2), 216-223.

Ahmadzadeh, M., Saranjam, B., Hoseini Fard, A., & Binesh, A. R. (2014). Numerical simulation of sphere water entry problem using Eulerian–Lagrangian method. *Applied Mathematical Modelling, 38*(5-6), 1673-1684. doi:10.1016/j.apm.2013.09.005

Alay, E., Skotak, M., Misistia, A., & Chandra, N. (2017). Dynamic loads on human and animal surrogates at different test locations in compressed-gas-driven shock tubes. *Shock Waves, 28*(1), 51-62. doi:10.1007/s00193-017-0762-4

Arakeri, J., Das, D., Krothapalli, A., & Lourenco, L. (2004). Vortex ring formation at the open end of a shock tube: A particle image velocimetry study. *Physics of Fluids, 16*(4), 1008-1019.

Bass, C. R., Panzer, M. B., Rafaels, K. A., Wood, G., Shridharani, J., & Capehart, B. (2012). Brain injuries from blast. *Ann Biomed Eng, 40*(1), 185-202. doi:10.1007/s10439-011-0424-0

Baum, S., & Shekhter, B. I. (1959). Physics of an Explosion. 954.

Cernak, I., Merkle, A. C., Koliatsos, V. E., Bilik, J. M., Luong, Q. T., Mahota, T. M., Ahmed, F. A. (2011). The pathobiology of blast injuries and blast-induced neurotrauma as identified using a new experimental model of injury in mice. *Neurobiol Dis, 41*(2), 538-551. doi:10.1016/j.nbd.2010.10.025

Chandra, N., Ganpule, S., Kleinschmit, N. N., Feng, R., Holmberg, A. D., Sundaramurthy, A., Alai, A. (2012). Evolution of blast wave profiles in simulated air blasts: experiment and computational modeling. *Shock Waves, 22*(5), 403-415. doi:10.1007/s00193-012-0399-2

Chandra, N., Sundaramurthy, A., & Gupta, R. K. (2017). Validation of Laboratory Animal and Surrogate Human Models in Primary Blast Injury Studies. *Mil Med, 182*(S1), 105-113. doi:10.7205/MILMED-D-16-00144

Chisnell, R. F. (1957). The motion of a shock wave in a channel, with applications to cylindrical and spherical shock waves. *Journal of Fluid Mechanics, 2*(3), 286-298. doi:10.1017/S0022112057000130

Clemedson, C., & Criborn, C. (1955). A detonation chamber for physiological blast research. *The Journal of aviation medicine, 26*(5), 373.

Condon, J. A., Lottero, R. E., & Loucks, R. B. (1997). *Construction and Testing of the ARL 1.68-m Diameter Shock Tube Exit Jet Spreader for Non-Ideal Blast Simulation*. Retrieved from

Courtney, A. C., Andrusiv, L. P., & Courtney, M. W. (2012). Oxy-acetylene driven laboratory scale shock tubes for studying blast wave effects. *Rev Sci Instrum, 83*(4), 045111. doi:10.1063/1.3702803

Courtney, A. C., & Courtney, M. W. (2009). A thoracic mechanism of mild traumatic brain injury due to blast pressure waves. *Med Hypotheses, 72*(1), 76-83. doi:10.1016/j.mehy.2008.08.015

Defense and Veterans Brain Injury Center, DoD Numbers for Traumatic Brain Injury. (2013).

Elder Jr, F., & De Haas, N. (1952). Experimental study of the formation of a vortex ring at the open end of a cylindrical shock tube. *Journal of Applied Physics, 23*(10), 1065-1069.

Emrich, R., & Curtis, C. (1953). Attenuation in the shock tube. *Journal of Applied Physics, 24*(3), 360-363.

Ethridge, N., Lottero, Wortman, & Bertrand. (1984). Computational and Experimental Studies of Blockage Effects in a Blast Simulator.

Fievisohn, E., Bailey, Z., Guettler, A., & VandeVord, P. (2018). Primary Blast Brain Injury Mechanisms: Current Knowledge, Limitations, and Future Directions. *J Biomech Eng, 140*(2). doi:10.1115/1.4038710

Frohn, A., & De Boer, P. (1969). Measurement of ionization relaxation times in shock tubes. *The Physics of Fluids, 12*(5), I-54-I-57.

Gilbert Ford Kinney, K. J. G. (1985). *Explosive Shocks in Air* (Second ed.). Heildelberg New York: Springer Science, Business Media.

Griffith, W. (1952). Shock-tube studies of transonic flow over wedge profiles. *Journal of the Aeronautical Sciences, 19*(4), 249-257.

Henshall, B. D., & Aeronautical Research, C. (1957). *On some aspects of the use of shock tubes in aerodynamic research*. London: H.M. Stationery Off.

Hertzberg, A. (1951). A shock tube method of generating hypersonic flows. *Journal of the Aeronautical Sciences, 18*(12), 803-804.

Hoge, C. W., McGurk, D., Thomas, J. L., Cox, A. L., Engel, C. C., & Castro, C. A. (2008). Mild Traumatic Brain Injury in U.S. Soldiers Returning from Iraq. *The New England Journal of*

Medicine, 358(5), 453–463. doi:https://doi.org/10.1056/NEJMoa1414264

Holmberg, A. (2010). *Development and Characterization of Shock Tubes for Laboratory Scale Blast Wave Simulation.* (Masters of Science), University of Nebraska, Lincoln,

Jiang, Z., Onodera, O., & Takayama, K. (1999). Evolution of shock waves and the primary vortex loop discharged from a square cross-sectional tube. *Shock Waves, 9*(1), 1-10. doi:10.1007/s001930050133

Jones, E., Fear, N. T., & Wessely, S. (2007). Shell shock and mild traumatic brain injury: a historical review. *Am J Psychiatry, 164*(11), 1641-1645. doi:10.1176/appi.ajp.2007.07071180

Kinney, G. F., & Graham, K. J. (1985). *Explosive Shocks in Air* (2nd ed.): Springer Science.

Koroteeva, E. Y., Znamenskaya, I., Glazyrin, F., & Sysoev, N. (2016). Numerical and experimental study of shock waves emanating from an open-ended rectangular tube. *Shock Waves, 26*(3), 269-277.

Kuriakose, M., Skotak, M., Misistia, A., Kahali, S., Sundaramurthy, A., & Chandra, N. (2016). Tailoring the Blast Exposure Conditions in the Shock Tube for Generating Pure, Primary Shock Waves: The End Plate Facilitates Elimination of Secondary

Loading of the Specimen. *PLoS One, 11*(9), e0161597. doi:10.1371/journal.pone.0161597

Maeno, K., Kaneta, T., Morioka, T., & Honma, H. (2005). Pseudo-schlieren CT measurement of three-dimensional flow phenomena on shock waves and vortices discharged from open ends. *Shock Waves, 14*(4), 239-249.

Mariani, R., & Kontis, K. (2010). Experimental studies on coaxial vortex loops. *Physics of Fluids, 22*(12), 126102.

Martin, W. (1958). A Review of Shock Tubes and Shock Tunnels. *Aerodynamics*, 1-73.

Masel, B. E., Bell, R. S., Brossart, S., Grill, R. J., Hayes, R. L., Levin, H. S., DeWitt, D. S. (2012). Galveston Brain Injury Conference 2010: clinical and experimental aspects of blast injury. *Journal of neurotrauma, 29*(12), 2143-2171.

Moore, D. F., Jerusalem, A., Nyein, M., Noels, L., Jaffee, M. S., & Radovitzky, R. A. (2009). Computational biology - modeling of primary blast effects on the central nervous system. *Neuroimage, 47 Suppl 2*, T10-20. doi:10.1016/j.neuroimage.2009.02.019

Moss, W. C., King, M. J., & Blackman, E. G. (2009). Skull flexure from blast waves: a mechanism for brain injury with implications for helmet design. *Phys Rev Lett, 103*(10), 108702. doi:10.1103/PhysRevLett.103.108702

Murugan, T., De, S., Dora, C., & Das, D. (2012). Numerical simulation and PIV study of compressible vortex ring evolution. *Shock Waves, 22*(1), 69-83.

Murugan, T., De, S., Dora, C., Das, D., & Kumar, P. P. (2013). A study of the counter rotating vortex rings interacting with the primary vortex ring in shock tube generated flows. *Fluid Dynamics Research, 45*(2), 025506.

Murugan, T., De, S., Sreevatsa, A., & Dutta, S. (2016). Numerical simulation of a compressible vortex–wall interaction. *Shock Waves, 26*(3), 311-326.

Murugan, T., Dora, C. L., De, S., & Das, D. (2018). A comparative three-dimensional study of impulsive flow emanating from a shock tube for shock Mach number 1.6. *Journal of Visualization, 21*(6), 921-934.

Nagamatsu, H. T. (1958). Shock tube technology and design.

Needham, C. E., Ritzel, D., Rule, G. T., Wiri, S., & Young, L. (2015). Blast Testing Issues and TBI: Experimental Models That Lead to Wrong Conclusions. *Front Neurol, 6*, 72. doi:10.3389/fneur.2015.00072

Onodera, O., Jiang, Z., & Takayama, K. (1998). Holographic Interferometric Observation of Shock Waves Discharged from an Open-Eng of a Square Cross-Sectional Shock Tube. *JSME International Journal Series B Fluids and Thermal Engineering, 41*(2), 408-415.

Risling, M., Plantman, S., Angeria, M., Rostami, E., Bellander, B. M., Kirkegaard, M., .Davidsson, J. (2011). Mechanisms of blast induced brain injuries, experimental studies in rats. *Neuroimage, 54 Suppl 1*, S89-97. doi:10.1016/j.neuroimage.2010.05.031

Ruff, R. L. (2008). Headaches among Operation Iraqi Freedom/Operation Enduring Freedom veterans with mild traumatic brain injury associated with exposures to explosions. *The Journal of Rehabilitation Research and Development, 45*(7), 941-952. doi:10.1682/jrrd.2008.02.0028

Skews, B. W. (1967). The perturbed region behind a diffracting shock wave. *Journal of Fluid Mechanics, 29*(4), 705-719.

Skotak, M., Alay, E., & Chandra, N. (2018). On the accurate determination of shock wave time-pressure profile in the experimental models of blast induced neurotrauma. *Frontiers in Neurology, 9*, 52.

Slepička, F. (1966). Attenuation in shock tubes. *Physics of Fluids, 9*(9), 1865-1866.

Southard, E. E. (1919). *Shell-shock and other neuropsychiatric problems*: WM Leonard.

Stuhmiller, J. H. (2008). *Blast Injury: Translating Research Into Operational Medicine*: United States Dept. of Defense.

Sundaramurthy, A., Alai, A., Ganpule, S., Holmberg, A., Plougonven, E., & Chandra, N. (2012). Blast-induced biomechanical loading of the rat: an experimental and anatomically accurate computational blast injury model. *J Neurotrauma, 29*(13), 2352-2364. doi:10.1089/neu.2012.2413

Tanielian, T. L. (2008). Invisible Wounds of War Psychological and Cognitive Injuries, Their Consequences, and Services to Assist Recovery. 499.

Tsaousides, T., & Gordon, W. A. (2009). Cognitive rehabilitation following traumatic brain injury: assessment to treatment. *Mt Sinai J Med, 76*(2), 173-181. doi:10.1002/msj.20099

Zare-Behtash, H., Kontis, K., & Gongora-Orozco, N. (2008). Experimental investigations of compressible vortex loops. *Physics of Fluids, 20*(12), 126105.